NASA CONTRACTOR REPORT

NASA CR-

NASA CR-2881

F-8C ADAPTIVE FLIGHT CONTROL EXTENSIONS

Gunter Stein and Gary L. Hartmann

Prepared by
HONEYWELL, INC.
Minneapolis, Minn. 55413
for Langley Research Center

NATIONAL AERONAUTICS AND SPACE ADMINISTRATION • WASHINGTON, D. C. • SEPTEMBER 1977

1. Report No.	2. Government Accession No.	3. Recipient's Catalog No.
NASA CR-2881		

4. Title and Subtitle	5. Report Date
F-8C ADAPTIVE FLIGHT CONTROL EXTENSIONS	September 1977
	6. Performing Organization Code

7. Author(s)	8. Performing Organization Report No.
Gunter Stein and Gary L. Hartmann	76SRC16
	10. Work Unit No.

9. Performing Organization Name and Address	11. Contract or Grant No.
Honeywell, Inc., Systems and Research Center 2600 Ridgway Parkway, N. E. Minneapolis, Minnesota 55413	NAS 1-13383
	13. Type of Report and Period Covered
12. Sponsoring Agency Name and Address	Final Report
National Aeronautics and Space Administration Hampton, Virginia 23665	14. Sponsoring Agency Code

15. Supplementary Notes

Langley technical monitors: Jarrell R. Elliott and Joseph Gera

Extension of Final Report under Contract NAS1-13383.

16. Abstract

A previous study of three digital adaptive concepts for the F-8C selected an explicit Maximum Likelihood Estimation (MLE) design as the most promising. This study investigated three areas for improving the baseline design. The first area involved improving the pitch axis estimation accuracy by incorporating attitude data, estimating gust intensity for setting filter gains and improving parameter tracking during changing flight conditions. The second area involved the design of a lateral identifier to improve true air speed and angle-of-attack estimates during lateral maneuvers. The third area examined the relationships in the MLE design and exploited them to detect failures in the input sensors.

Design details and simulation performance are presented for each of the three areas investigated.

17. Key Words (Suggested by Author(s))	18. Distribution Statement
Flight Control Adaptive Identification Digital F-8C Maximum Likelihood Estimation	Unclassified - unlimited Subject Category 08

19. Security Classif. (of this report)	20. Security Classif. (of this page)	21. No. of Pages	22. Price*
Unclassified	Unclassified	141	$6.00

* For sale by the National Technical Information Service, Springfield, Virginia 22161

CONTENTS

ILLUSTRATIONS

TABLES

F-8C ADAPTIVE FLIGHT CONTROL EXTENSIONS

Gunter Stein and Gary L. Hartmann
Honeywell, Inc., Minneapolis, MN

SECTION 1
PROGRAM OVERVIEW

NASA is conducting a research program in digital fly-by-wire technology using a modified F-8C aircraft. To support these efforts, Honeywell initiated a design program in 1974 to provide digital adaptive control laws suitable for flight test. As part of the ground rules, measurements were restricted to rate gyros, accelerometers and servo position. Adjustment of the control laws is based on this information. Aircraft like the F-8, whose performance requirements can be satisfied with air-data-scheduled control laws, benefit most by eliminating air data gain scheduling. This will be particularly valuable for future aircraft requiring flight-critical gain adjustment. The control laws were constrained to be compatible with the existing airframe without structural modification. Hence, they use only existing elevator, rudder, and ailerons as control effectors, each powered by existing actuators.

The design program recommended an adaptive concept which combines gain-scheduled control laws with explicit maximum likelihood identification to provide the scheduling variables. This approach was selected from a comparison of three candidate concepts:

- Implicit gain adjustment based on self-excited limit cycles
- Gain adjustment based on explicit identification using a Liapunov model tracker
- Gain adjustment based on explicit identification with Maximum Likelihood Estimation (MLE)

The MLE Baseline

An overall functional diagram of the recommended design is shown in Figure 1. The control laws consist of a quadratic-optimal C* model-followi system in the pitch axis and a first-order roll model-following system in th lateral-directional axes. High frequency roll-off compensation and integral action required for trim were incorporated directly into the optimal design formulation. The resulting feedback and feedforward gains were simplified and approximated as simple functions of estimated surface effectiveness by the adaptive algorithm.

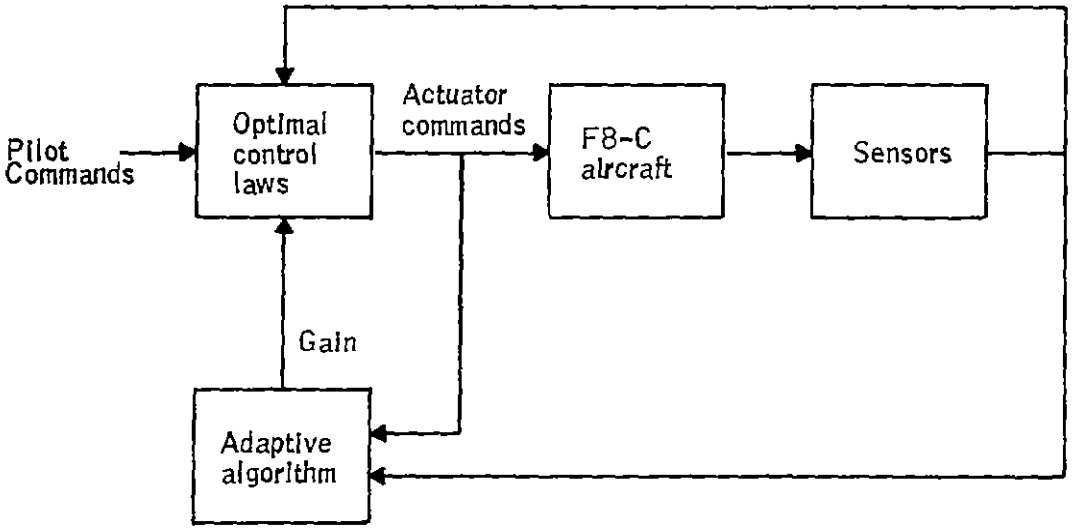

Figure 1. F-8C Adaptive Structure

Surface effectiveness estimates are obtained from an explicit pitch-axis parameter identifier based on standard MLE theory. To avoid on-board iterative calculations, the identifier uses a parallel channel implementation. Several Kalman filter channels operate at fixed locations in parameter spac Likelihood functions are computed for each. Sensitivity equations are then

solved only for the maximum likelihood channel and used to interpolate from there to the correct parameter value. Theoretical identifiability results were used to determine the number of parameters that could be identified with small test inputs. This accuracy analysis also provided insight into the number and location of the filter channels.

Five parallel channels suffice to handle the F-8C aircraft over its entire operational flight envelope. They estimate three parameters -- surface effectiveness ($M_{\delta o}$), pitching moment due to angle-of-attack (M_{α}), and airspeed (V). Estimation accuracy depends strongly on the signal levels in the control loop. For the small test signals tolerable in operational situations, errors of 10-20 percent in $M_{\delta o}$ and 20-30 percent in M_{α} and V are typical in six-degree-of-freedom simulation runs. Theoretical accuracy analyses confirm these error levels. The gain adjustment in the pitch and lateral control laws is a function of estimated $M_{\delta o}$ only. However, the MLE design was selected in large part for its potential to identify additional parameters which may be needed for scheduling in other applications (ref. 1).

Design Extensions

The design program was extended in 1975 to further develop the MLE concept. Three specific areas of study were selected:

- Improvement of the baseline pitch-axis identifier.- This research was directed toward improving the performance of the MLE algorithm by incorporating attitude data, estimating gust statistics for setting filter gains, and improving parameter tracking during changing flight conditions.

- Design of a lateral MLE algorithm.- The purpose of this algorithm was to improve true air speed and angle-of-attack estimates during lateral maneuvers. These

estimates could then be used as scheduling parameters in an inertially coordinated lateral CAS.

- Analytical redundancy.- The purpose of this task was to examine relationships between the pitch axis sensors inherent in the MLE design and to exploit them for sensor failure detection. Success of such techniques could reduce the number of redundant sensors required in flight control implementations.

Conclusions of the Extension Study

Research and design efforts performed under the extended program are documented in this report. They lead to the following major conclusions:

1) The pitch-axis study indicates that on-line estimation of gust statistics works well and will reduce test signal requirements and/or enhance accuracy. However, no significant improvement in accuracy is provided by incorporating attitude data. By restructuring the parameter interpolation as another Kalman filter, significant improvements in tracking time-varying parameters can also be achieved.

2) The lateral study shows that inertially coordinated lateral control systems can be implemented without air data measurements. A lateral identifier was designed to improve the baseline angle-of-attack and airspeed estimates. These were used to schedule an inertially coordinated CAS and show good damping and turn coordination. The resulting adaptive structure could potentially be simplified to a single extended Kalman filter.

3) Preliminary results on analytical redundancy indicate promising potential for sensor reduction in redundant systems. Three candidate analytical redundancy procedures were developed which exploit existing computations in the baseline identifier structure to detect and isolate gyro and accelerometer failures. Limited simulation evaluations of these procedures show promising performance of at least one candidate. Further evaluations are required to solidly establish false alarm and missed alarm characteristics.

Document Organization

This document is subdivided into six sections. This section is an overview of the extensions to the baseline F-8 Adaptive program. Section 2 presents a list of symbols used throughout the report. Section 3 presents the results of the modifications to the baseline pitch identifier. Section 4 presents the MLE lateral adaptive design. Section 5 presents the results of the analytical redundancy study. Section 6 presents conclusions and recommendations. Section 7 contains a list of references.

For additional details of the baseline in F-8C Adaptive Study, the reader is referred to the earlier report prepared under this contract (ref. 1).

SECTION 2

SYMBOLS

Operators

$\text{Arg}\{\min_{x} f(x)\}$	- minimizing argument of function $f(\cdot)$
$E(\cdot)$	- mathematical expectation
$\exp(\cdot)$	- exponential
$\ell n(\cdot)$	- natural logarithm
$\ell n \det(\cdot)$	- natural log of determinant
$p(x/y)$	- conditional probability distribution of x given y
s	- Laplace operator
z	- delay operator
$(\cdot) = \frac{d}{dt}$	- time derivative
$\Delta(\cdot)$	- increment
$\nabla(\cdot)$	- gradient vector with respect to parameter vector ζ
$\nabla^2(\cdot)$	- second partial derivative matrix with respect to parameters ζ
$\nabla_p(\cdot)$	- p-th component of $\nabla(\cdot)$
Σ	- summation
$\|x\|$	- absolute value
$\|\|x\|\|^2_M$	- quadratic form $x^T M x$

Superscripts

$\hat{(\ )}$	- estimated value
$\bar{(\ )}$	- one-step predicted value
$(\ )^{(i)}$	- value for parallel channel i
$(\ )^\circ$	- nominal value

Subscripts

$( )_m$	- measured value
$( )_k$	- value at time t_k
$( )_L$	- value for lateral identifier
$( )_P$	- value for pitch identifier
$( )_s$	- stability axis
$( )_t$	- true value

Upper Case Symbols

A	- discrete system dynamics matrix
B	- (1) discrete system input matrix (2) residual covariance matrix
C*	- response variable $N_z + V_{co}q$
D	- measurement matrix, y due to u
$G_{c*}, G_{LAT}, G_{ROLL}, G_{RSS}$	- control gains
H	- measurement matrix
H_i	- hypothesis number i
I	- identity matrix
I_a, I_g, I_{ar}	- failure flags for accelerometer, gyro and analytic test
J	- partial likelihood function L - $1/2 \sum \ell n \det B$
K	- Kalman filter gains
K_{RP}, K_{RUM}, K_{RPM}	- rudder control gains
K_{A_c}	- aileron control gain
L	- likelihood function

SYMBOLS (Continued)

L_v	- lateral gust field scale length
M	- number of parallel channels
M_q, M_α, $M_\delta(M_{\delta e})$, $M_{\dot{\alpha}}$	- pitching moment coefficients due to indicated variables
M_o	- trim pitching moment
$M_{\delta o}$	- M_δ value for rigid airframe (without quasistatic flexibility)
$M_{\delta t}$	- true value of $M_{\delta o}$
N	- number of data samples
N_z, N_y	- normal and lateral acceleration
P	- Kalman filter covariance matrix
P_o	- a priori parameter covariance matrix
Q_λ, $\dot{\lambda}$	- noise intensities for parameter process model
Q_i	- failure rate for element i
S	- Kalman filter design statistics
T	- transformation matrix
U_N	- sequence of N control inputs
V	- air speed
V_{co}	- crossover velocity in C* response
Y_β, $Y_{\delta a}$, Y_{dr}	- lateral force coefficients due to indicated variables
Y_N	- sequence of N measurements
Z_α, Z_δ	- normal force coefficients due to indicated variables

SYMBOLS (Continued)

Lower Case Symbols

$\underline{c}$, c_i	- parameter vector with components c_i
$\underline{c}_o$	- a priori estimate of c
$\underline{c}_t$	- true value of c
d	- sensor displacement from c. g. (4. 62m)
g, g_o	- gravity
h	- altitude
i*	- index of the minimum-L channel
n	- system order
p	- roll rate
$\bar{q}$	- dynamic pressure
r	- (1) yaw rate (2) number of measurements
t	- time
u	- control input vector
v	- lateral velocity perturbation
v_g	- lateral gust component
x	- state vector
y	- measurement vector
z	- test statistic in analytic test

Greek Symbols

Upper Case

Γ	- discrete system noise input matrix

Greek Lower Case

α	- angle-of-attack
α_g	- gust angle-of-attack
β	- angle of sideslip
β_g	- gust angle of sideslip
$\delta_e(\delta)$, δ_a, δ_r	- aerodynamic surface positions
ϵ	- stability-axis yaw rate error
ϵ_k, $\Delta\epsilon_k$	- generic likelihood filter states
γ_{ij}	- ij element of Γ
ζ	- dummy argument for values of parameter vector $\underline{c}$
η	- white noise process
θ	- pitch attitude
λ, $\dot{\lambda}$	- parameter model state variables
μ	- $\exp(-\Delta t/\tau)$
ν	- Kalman filter residuals
ξ	- white noise process
ρ	- air density
σ, σ_x	- standard deviation of variable x
τ	- time constant
ϕ	- roll attitude
ψ	- yaw attitude
ω	- natural frequency

SECTION 3
PITCH IDENTIFIER REFINEMENTS

This section includes research results on recommended refinements of the parallel-channel maximum likelihood identifier developed in ref. 1 . It includes a brief summary of the identifier's baseline design and performance characteristic, with emphasis on fundamental performance limitations which motivate the refinements. Three potential areas of improvement are discussed:

- Adaptation to changing gust level statistics,
- Incorporation of attitude measurements, and
- Parameter tracking aids.

Our investigations showed that the first and third of these areas provide substantive performance improvements for the identifier. Hence, design modifications are recommended to incorporate these features in the baseline system. The second area was found to offer only minor improvements which fail to justify design modifications.

Baseline Identifier Design Summary

The recommended baseline F-8C identifier, ref. 1 , is illustrated in Figure 2. It consists of a parallel-channel structure designed to perform on-line maximum likelihood estimation of three aircraft parameters: $M_{\delta o}$, c_2, c_3. These represent elevator surface effectiveness, pitching moment due to angle-of-attack, and velocity, respectively. Only pitch axis data (q_m, N_{z_m}, δ_m) is used for identification. This overall structure is a result of detailed identifiability analyses for the F-8C and tradeoff studies of several

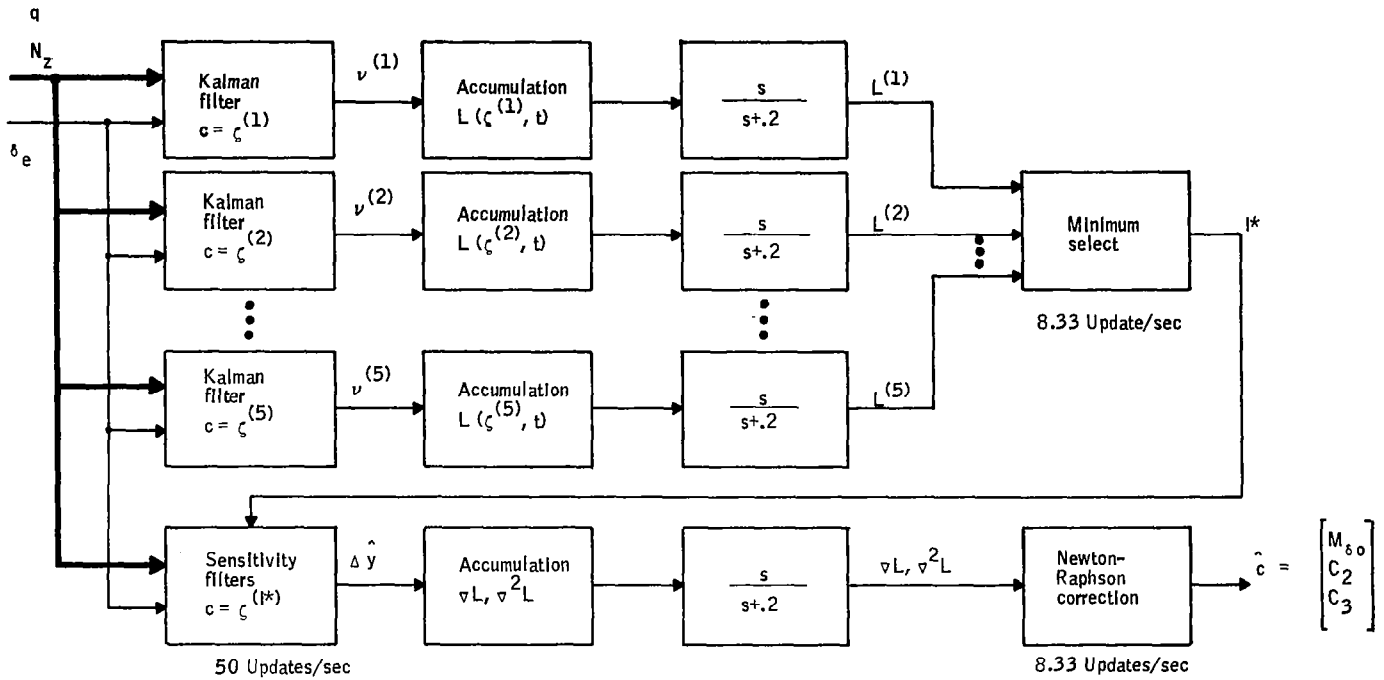

Figure 2. Parallel-Channel Maximum Likelihood Identifier

candidate identification algorithms, ref. 1 . Only selected design details are presented here which are relevant to the refinement studies.

Parallel minimization. - The main feature of the F-8C identifier is its parallel Kalman filter structure. This structure provides a non-iterative way to carry out the function minimizations required by maximum likelihood estimation. Recall that the maximum likelihood method provides a solution of the following identification problem:

$$\begin{aligned} &\text{Given: } x_k = A(\underline{c})\, x_{k-1} + B(\underline{c})\, u_{k-1} + \Gamma(\underline{c})\, \xi_k \\ &\qquad\quad y_k = H(\underline{c})\, x_k + D(\underline{c})\, u_k + \eta_k \qquad\qquad k = 0,\ 1,\ \ldots \\ &\text{Find : Unknown constant parameters } \underline{c} \end{aligned} \tag{1}$$

The usual interpretations apply: x's are states, u's are controls, y's are measurements, A, B, Γ, H, D are matrices (functions of $\underline{c}$), and ξ_k and η_k are discrete white noise processes. As shown in ref. 1 the theoretical maximum likelihood solution of this identification problem is

$$\begin{aligned} \hat{\underline{c}}_N &= \text{Arg}\{\max_{\zeta} p\,(Y_N | \underline{c} = \zeta,\ U_N)\} \\ &= \text{Arg}\{\min_{\zeta} - \ell n p\,(Y_N | \underline{c} = \zeta,\ U_N)\} \\ &= \text{Arg}\{\min \frac{1}{2} \sum_{k=1}^{N} \left[\left\| y_k - \hat{y}_k(\zeta) \right\|^2_{B^{-1}(\zeta)} + \ell n \det B(\zeta) \right]\} \end{aligned} \tag{2}$$

where $p(\alpha|\beta)$ denotes probability distributions of α conditioned on β, Y_N and U_N denote sequences of N measurements and N control inputs, $\hat{y}_k(\zeta)$ are Kalman filter predictions of y_k given Y_{k-1}, U_{k-1} and $\underline{c} = \zeta$, and $B(\zeta)$ is the error covariance matrix for those predictions.

The F-8C identifier approximates equation (2) in the following manner. First, it evaluates the function to be minimized [this is the likelihood function $L(\zeta, k)$] at several fixed values, $\zeta^{(i)}$, of the argument ζ. The best of these values, $\zeta^{(i*)}$, is then selected and a single Newton-Raphson step is taken from there to the parameter estimate, i.e.,

$$\hat{c}_N = \zeta^{(i*)} - (\nabla^2 L)^{-1} \nabla L \tag{3}$$

The symbols ∇L and $\nabla^2 L$ denote first and second partial derivatives of L with respect to ζ evaluated at $\zeta = \zeta^{(i*)}$. In order to keep calculations as simple as possible, the Newton-Raphson step is actually based on approximate versions of these derivatives, as summarized below.

$$\text{Let } \nu_k \triangleq y_k - \hat{y}_k(\zeta^{(i*)}) \tag{4}$$

Then

$$L \triangleq \frac{1}{2} \sum_{k=1}^{N} (\nu_k^T B^{-1} \nu_k + \ell n \det B) \tag{5}$$

$$\begin{aligned} \nabla L &= \sum_{k=1}^{N} [-\nabla \hat{y}_k B^{-1} \nu_k + \tfrac{1}{2} \mathrm{Tr}\,(\nu_k \nu_k^T - B)\, \nabla(B^{-1})] \\ &\simeq \sum_{k=1}^{N} - \nabla \hat{y}_k B^{-1} \nu_k \end{aligned} \tag{6}$$

(This is justified because $E(\nu\nu^T) \to B$ as $\zeta \to \underline{c}$)

$$\begin{aligned} \nabla^2 L = \sum_{k=1}^{N} \{ & -\nabla^2 \hat{y}_k B^{-1} \nu_k - \nabla \hat{y}_k \nabla(B^{-1}) \nu_k + \nabla \hat{y}_k B^{-1} \nabla \hat{y}_k^T \\ & + \tfrac{1}{2} \mathrm{TR}[(-2 \nabla \hat{y}_k \nu_k^T - \nabla B)\, \nabla(B^{-1}) + (\nu_k \nu_k^T - B)\, \nabla^2(B^{-1})] \} \\ \simeq \sum_{k=1}^{N} & (\nabla \hat{y}_k B^{-1} \nabla \hat{y}_k^T + \tfrac{1}{2} \mathrm{TR}\, \nabla B\, B^{-1}\, \nabla B\, B^{-1}) \end{aligned}$$

[This is justified because $\nu \rightarrow$ (zero mean white noise)

and $E(\nu\nu^T) \rightarrow B$ as $\zeta \rightarrow \underline{c}$]

$$\simeq \sum_{k=1}^{N} \nabla\hat{y}_k \, B^{-1} \, \nabla\hat{y}_k^T \tag{7}$$

(This assumes $\nabla B \, B^{-1}$ is small)

Equations (6) and (7) were used to define ∇L and $\nabla^2 L$ for purposes of identifier design.

Parameter tracking. - The theoretical MLE solution equation (2) is based on the assumption that the vector $\underline{c}$ is constant over the time interval covered by the data sequences U_N and Y_N. This means that current data receives equal weighting with past data in the L, ∇L and $\nabla^2 L$ summations of equation (5), (6) and (7), and large errors result in the event that $\underline{c}$ actually undergoes changes. Because the latter case is prevalent for aircraft in rapid flight transition, the identifier in Figure 2 employs high-pass filters to "forget" old accumulated likelihood data. This heuristic "fix" of the theory is actually equivalent to exponential de-weighting of terms in the likelihood summations. This can be readily verified by observing that a cascaded accumulation/high-pass operation has the following analog transfer function:

$$\left[\frac{1}{s}\right] \cdot \left[\frac{s}{s+\frac{1}{\tau}}\right] = \left[\frac{1}{s+\frac{1}{\tau}}\right]$$

In discrete-time form, this corresponds to

$$\epsilon_N = \mu\epsilon_{N-1} + \Delta\epsilon_N \tag{8}$$

$$= \mu\,(\mu\epsilon_{N-2} + \Delta\epsilon_{N-1}) + \Delta\epsilon_N$$

$$\bullet$$

$$\bullet$$

$$\bullet$$

$$= \sum_{k=1}^{N} \mu^{N-k} \, \Delta\epsilon_k \tag{9}$$

where $\mu = \exp(-\Delta t/\tau)$, and ϵ denotes a generic output variable of the combined accumulation/high-pass operation on the input sequence $\Delta\epsilon$. Letting ϵ be L, ∇L, and $\nabla^2 L$ with the appropriate substitution results in the following update equations:

$$L_N = \mu L_{N-1} + \frac{1}{2}(\nu_N{}^T B^{-1} \nu_N + \ell n \det B) \tag{10}$$

$$\nabla L_N = \mu \nabla L_{N-1} + (-\nabla \hat{y}_N B^{-1} \nu_N) \tag{11}$$

$$\nabla^2 L_N = \mu \nabla^2 L_{N-1} + (\nabla \hat{y}_N B^{-1} \nabla \hat{y}_N{}^T) \tag{12}$$

These equations are used to calculate L, ∇L, and $\nabla^2 L$ in the baseline identifier. A high-pass time constant of $\tau = 5$ sec was selected as an experimental compromise between tracking error and identification accuracy at fixed flight conditions (ref. 1).

Plant model and parameterization. - Each Kalman filter in the parallel identifier structure was designed for a fixed plant model whose coefficients are parameterized as functions of $M_{\delta o}$, c_2, and c_3. The model is summarized in Figure 3. It includes longitudinal short period aircraft states (q, α), two Brownian motion states to simulate trim (g/V, M_o), and three white noise disturbances to approximate gusts and trim changes;

$$\frac{d}{dt}\alpha_g \cong \gamma_{21}\,\eta_1 \text{ with } \gamma_{21} \triangleq \sigma_w \sqrt{2/VL_w}$$

$$\frac{d}{dt}\frac{g}{V} \cong \gamma_{32}\,\eta_2 \text{ with } \gamma_{32} \triangleq \sigma_\gamma \sqrt{(g_o/V)}$$

$$\frac{d}{dt} M_o \cong \gamma_{43}\,\eta_3 \text{ with } \gamma_{43} \triangleq \sigma_{\delta_{trim}} M_\delta .$$

Measurements are represented by algebraic sensor output equations for pitch rate, normal acceleration and surface position. All are corrupted by discrete white noise sequences.

State Equations:

$$\frac{d}{dt}\begin{bmatrix} q \\ \alpha+\alpha_g \\ g/V \\ M_0 \end{bmatrix} = \begin{bmatrix} M_q & M_\alpha & 0 & 1 \\ 1 & Z_\alpha & 1 & 0 \\ 0 & 0 & 0 & 0 \\ 0 & 0 & 0 & 0 \end{bmatrix} \begin{bmatrix} q \\ \alpha+\alpha_g \\ g/V \\ M_o \end{bmatrix} + \begin{bmatrix} M_\delta \\ Z_\delta \\ 0 \\ 0 \end{bmatrix} \delta + \begin{bmatrix} 0 & 0 & 0 \\ \gamma_{21} & 0 & 0 \\ 0 & \gamma_{32} & 0 \\ 0 & 0 & \gamma_{43} \end{bmatrix} \eta$$

Measurements:

$$y_k = \begin{bmatrix} q_m \\ N_{zm} \\ \delta_m \end{bmatrix}_k = \begin{bmatrix} 1 & 0 & 0 & 0 \\ dM_q & dM_\alpha - Z_\alpha V & 0 & d \\ 0 & 0 & 0 & 0 \end{bmatrix} \begin{bmatrix} q \\ \alpha+\alpha_g \\ g/V \\ M_0 \end{bmatrix}_k + \begin{bmatrix} 0 \\ dM_\delta - Z_\delta V \\ 1 \end{bmatrix} \delta_k + \begin{bmatrix} \sigma_g & 0 & 0 \\ 0 & \sigma_{Nz} & 0 \\ 0 & 0 & \sigma_\delta \end{bmatrix} \xi_k$$

$k = 0, 1, 2, \ldots$

Parameterization:

$$\begin{bmatrix} M_\delta \\ M_q \\ M_\alpha \\ V \\ Z_\alpha V \\ Z_\delta V \end{bmatrix} \simeq \begin{bmatrix} M_{\delta o}\,(1 + .016\, M_{\delta o} + .0002\, M_{\delta o}^2) \\ -.23 + (.028 - .017\, c_2)\, M_{\delta o} \\ (.61 + .92\, c_2)\, M_{\delta o} \\ (200 + c_3)\, M_{\delta o} \\ 53.0\, M_{\delta o} \\ 7.7\, M_\delta \end{bmatrix}$$

Figure 3. Plant Model for F-8C Identifier

Coefficient in the model are defined in terms of $M_{\delta o}$, c_2, and c_3 according to the parameterization given in Figure 3. Together with specified values for the six environmental statistics

$$S \triangleq (\sigma_w, \sigma_\gamma, \sigma_{\delta_{trim}}, \sigma_q, \sigma_{Nz}, \sigma_\delta), \tag{13}$$

this parameterization completely defines the Kalman filter gains, $K(\zeta^{(i)}, S)$, and error covariance matrices, $B(\zeta^{(i)}, S)$, in the parallel structure. The gains alone are actually valid for a broader class of statistics, namely the specified set in equation (13) with each element multiplied by an arbitrary common scale factor $\sigma \neq 0$; i.e.,

$$K(\zeta, \sigma S) \equiv K(\zeta, S). \tag{14}$$

The matrices B for the same class of statistics are given by

$$B(\zeta, \sigma S) = \sigma^2 B(\zeta, S). \tag{15}$$

This means that the likelihood function accumulations in equations (10), (11), and (12) change as σ changes but the parallel filters themselves do not. The F-8C identifier takes advantage of these relationships by using nominal values for the design statistics, $S = S^\circ$, but allowing a common scale factor to vary. The latter is estimated on-board and used to scale the likelihood functions accumulated in equation (10).

This process of "adapting to proportional noise statistics" prevents performance deteriorations due to changing values of the scale factor. The following nominal design statistics were used for S:

$$S^\circ = (6.0, .017, .001, .0026, .644, .0008) \tag{16}$$

Since these numbers are fixed for all operating conditions (i.e., with and without sensor noise, with and without gusts, with slow or fast trim changes, etc.), they represent experimental compromises over many simulation runs. As seen later in the performance summaries, further performance benefit can be gained by adaptively adjusting the relative values of these statistics as well as their common scale factor.

Channel locations. - As indicated in Figure 2, a total of five parallel channels suffice to handle F-8C parameter identification over the entire flight envelope. Their locations in parameter-space are tabulated below and illustrated on the M_{α} - $M_{\delta o}$ plane in Figure 4. The most significant feature of these locations is their logarithmic distribution along the $M_{\delta o}$ coordinate axis. Each channel "covers" a fixed percentage range (±50 percent about its nominal $M_{\delta o}$ value). This distribution is motiviated by identification accuracy studies which indicate that theoretical identification errors are directly proportional to the true $M_{\delta o}$ values (ref. 1).

Channel location	Subsonic range				Supersonic range
	1	2	3	4	5
$\underline{c} = \begin{bmatrix} M_{\delta o} \\ c_2 \\ c_3 \end{bmatrix}$	-2.34 0 0	-5.27 0 0	-11.9 0 0	-26.7 0 0	-26.7 1.0 60.0

Baseline Identifier Performance Summary

The identifier's performance was evaluated on NASA Langley's nonlinear six-degree-of-freedom F-8C simulator (ref. 3) against four "measures of goodness":

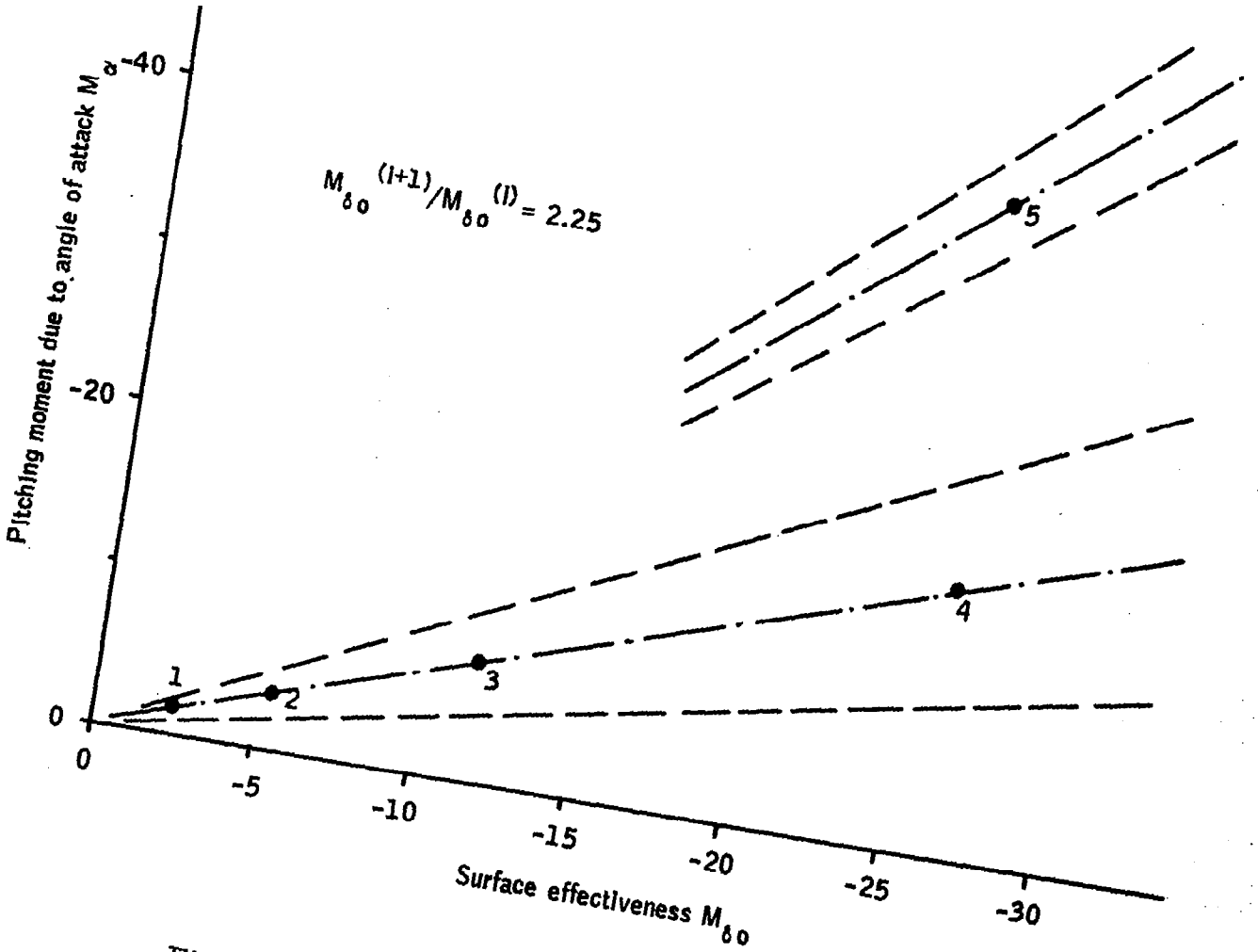

Figure 4. F-8C Identifier Channel Locations

- Identification accuracy at fixed flight conditions
- Convergence characteristics
- Parameter tracking during standard flight transitions
- Response to major maneuvers and configuration changes

Results show good performance throughout the flight envelope. Identification errors are consistently below 10-30 percent which is more than adequate to schedule the pitch and (reduced-measurement) lateral control laws. Accuracy deteriorates somewhat during rapid flight transitions but remains satisfactory for gain scheduling. Convergence from incorrect parameter initialization is smooth and rapid, taking approximately one second to reach 80 percent of final estimated parameter values. There are also no major difficulties with large maneuver (various rolls, high-g pullups, step gusts, etc.) and configuration changes (speed brake deployment, gear and wing transitions, and c. g. motion).

Like all realistic designs, however, there are design compromises, operational issues, and fundamental limitations which constrain the performance achieved. For the baseline F-8C identifier, these constraining items include:

- Accuracy compromises due to fixed filter design statistics,
- Test signal requirements, and
- Tracking errors.

Accuracy compromises due to fixed filter statistics are illustrated in Figure 5. This figure shows simulator traces of a standard accuracy test at fixed flight condition FC10 (h = 0. m, Mach 0. 7). The controlled aircraft was "flown" for 30 seconds under quiescent conditions (sensor noise plus test signal only). This is followed by a C* doublet command, then a 30-second period of turbulence (2 m/sec rms), another C*-doublet, and finally quiescence again.

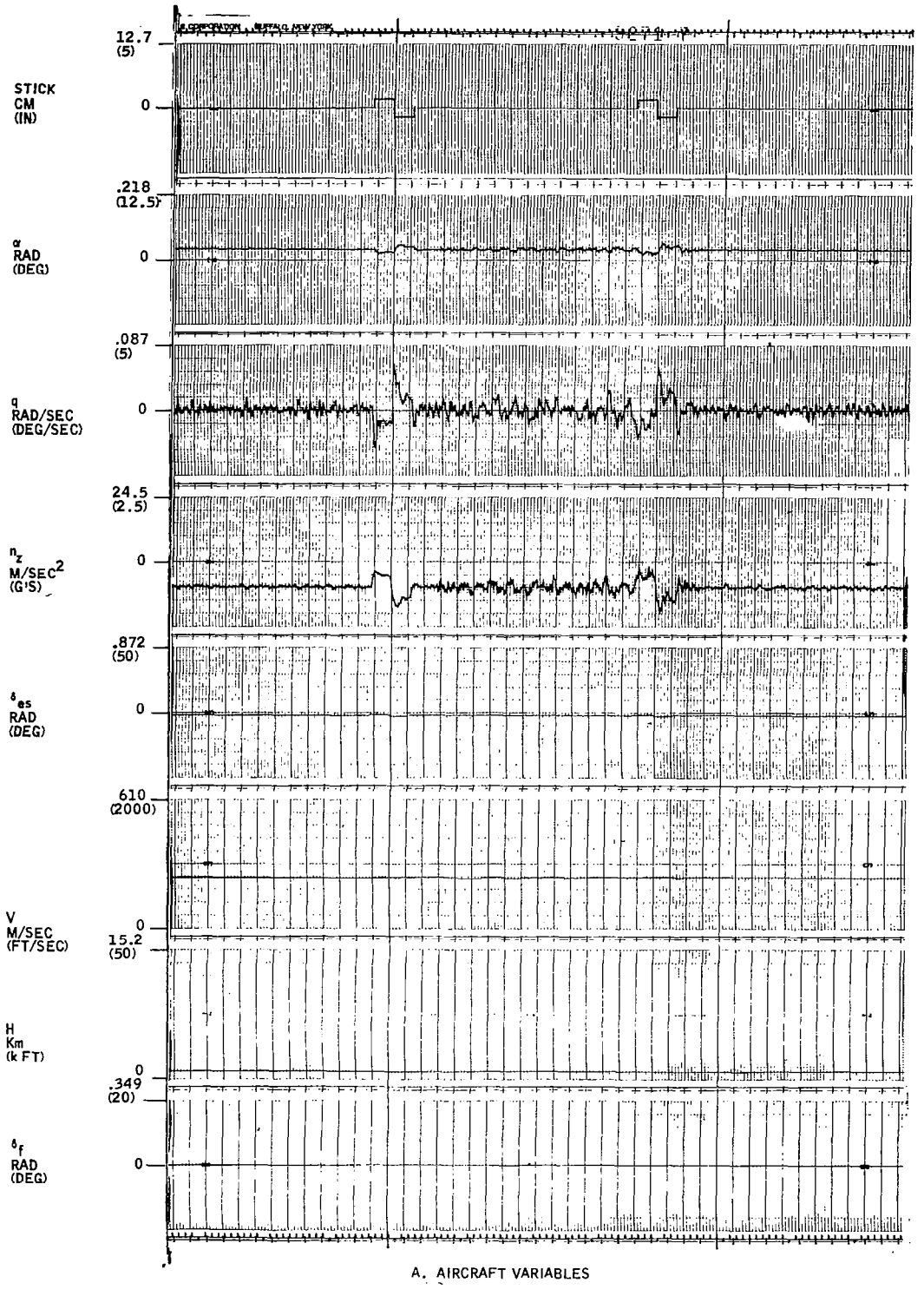

Figure 5. Standard Accuracy Test Traces at FC10

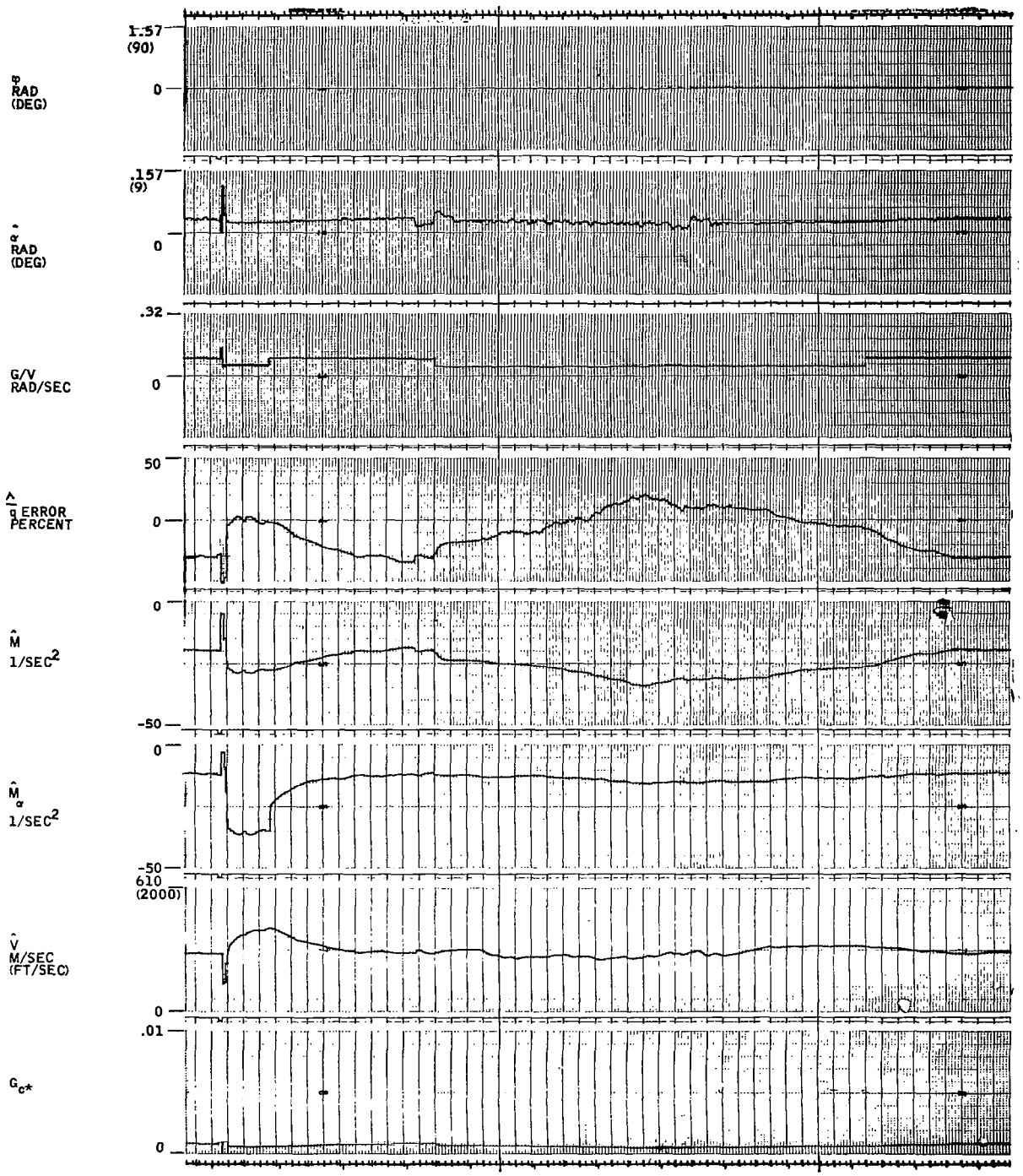

Figure 5. Standard Accuracy Test Traces at FC10 (Concluded)

This standard test sequence matches assumed filter design statistics for the central turbulence time segment only. Errors which result when the assumptions are violated are clearly evident on the $\hat{\bar{q}}$ error trace $\Delta\bar{q} = (\bar{q} - \hat{\bar{q}})/\bar{q}$.

Test signal levels required for the simulator evaluations in (ref. 1) are tabulated below:

FC	h(m)	Mach	Rms g's due to test signals
5	6090.	0.4	0.01
1	6090.	0.67	0.025
8	12180.	1.2	0.02
10	0.	0.7	0.04

While these numbers cannot be used directly to predict aircraft requirements, they are high enough at FC10 to suggest that test signals may become an important issue in flight. Test signal requirements interact strongly with identification accuracy and with design compromises which reduce accuracy. The errors due to fixed statistics in Figure 5, for example, can be completely eliminated with sufficiently large pilot commands or test input levels. Conversely, command and/or test signal levels can be reduced with inherently more accurate identifier designs.

Tracking error limitations are illustrated by the simulator traces shown in Figure 6. These recordings correspond to a standard max-power acceleration maneuver starting at FC5. They show estimation errors in excess of 30 percent on the $\Delta\bar{q}$ trace as the maneuver is executed. Errors as high as 50-70 percent have been observed during more dramatic flight transitions and configuration changes. Fundamentally, such "tracking errors" are due to incompatabilities between fixed-parameter MLE theory and actual aircraft parameter behavior. Even augmented with the heuristic high-pass filters in Figure 2, the theory offers only limited tracking performance.

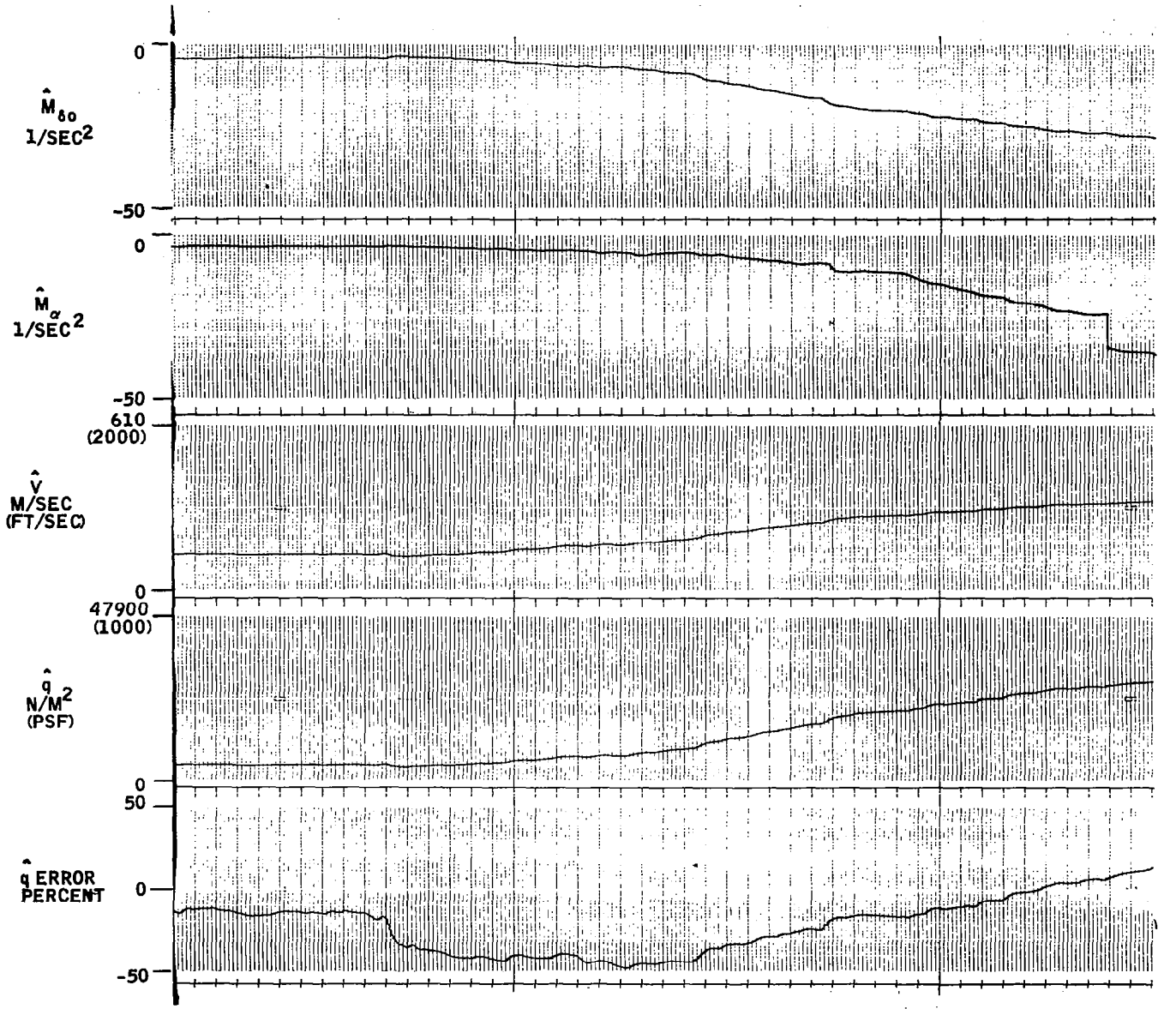

Figure 6. Standard Tracking Test Traces: Baseline Identifier

TABLE 1. - THEORETICAL GUST LEVEL ESTIMATION ACCURACY

Conditions

FC1 - 6090m, Mach .67

Data Length - 10 sec

Test Signal - .015 g's square wave

Sensor Noise - gyro 0.15 deg/sec rms
accel 0.02 g's rms

Accuracy (lower bound)

ACTUAL σ_{wo}	Percent error, $\sigma_\zeta / \lvert\zeta\rvert$			
m/sec	$M_{\delta o}$	M_α	V	σ_{wo}
0.3	7.8	13	15	30
1.0	5.0	12	15	18
2.0	3.1	10	14	16

Gust level estimation algorithms. - In the face of this limited accuracy potential, it was decided that continuous gust level estimation algorithms (and continuous readjustment of filter gains) would prove unjustified. As an alternative, a much simpler discrete algorithm was adopted which only discriminates between two levels of gust intensity--high and low--without attempting to estimate σ_w explicitly. The discrimination is done with a straightforward comparison of likelihood functions. Suppose we designate the two gust levels as

$$\sigma_w \Big|_{\text{low}} = \ell$$
$$\sigma_w \Big|_{\text{high}} = \overline{\ell} \qquad (20)$$

and assume that $\sigma_w = \ell$ is currently true. Then maximum likelihood theory assures the following inequality for N sufficiently large:

$$L(\zeta', N)\Big|_{\zeta' = (\underline{c}_t,\ \ell)} < L(\zeta', N)\Big|_{\zeta' = (\underline{c}_t,\ \bar{\ell})} \tag{21}$$

It is reasonable to assume that this inequality will also hold if ζ is not precisely equal to c_t and if σ_{wt} is not precisely equal to ℓ. This has been verified with experimental calculation of sample likelihood functions. The inequality can then be used as a discriminant function between two effective gust levels, i.e.,

$$\begin{aligned} &\text{High level if } L\Big|_{\zeta' = (\zeta^{(i*)},\ \ell)} > L\Big|_{\zeta' = (\zeta^{(i*)},\ \bar{\ell})} \\ &\text{Low level if } L\Big|_{\zeta' = (\zeta^{(i*)},\ \ell)} < L\Big|_{\zeta' = (\zeta^{(i*)},\ \bar{\ell})} \end{aligned} \tag{22}$$

Identifier modification. - These discrete discrimination equations are appealing because they can be readily incorporated in the baseline identifier. All that is needed is a sixth parallel channel located at $\zeta = \zeta^{(i*)}$ in parameter space but operating with the opposite gust level, i.e., with $\sigma_w = \bar{\ell}$ when the rest of the identifier is using $\sigma_w = \ell$ and vice versa. The difference between likelihood functions $L^{(6)}$ and $L^{(i*)}$ can then be monitored and the identifier switched from ℓ to $\bar{\ell}$ (or vice-versa) whenever $L^{(6)}$ falls (sufficiently) below $L^{(i*)}$. The fact that only two gust levels are utilized makes switching particularly easy. Two sets of filter gains (and gain sensitivities) corresponding to $\sigma_w = \ell,\ \bar{\ell}$ can be stored in memory for each parameter value $\zeta^{(i)}$ and brought on-line in accordance with the $L^{(6)} - L^{(i*)}$ comparison.

A block diagram of the baseline identifier with these modifications is shown in Figure 7.

Performance of the modified identifier. - The baseline identifier was modified as illustrated in Figure 7, and evaluated on the F-8C simulator at NASA Langley Research Center. A flow diagram of the new implementation is given in Appendix A. Its high and low gust statistics were chosen as $\overline{\ell}$ = 1.5 m/sec and ℓ = 0.3 m/sec, respectively. Sizeable hysteresis levels were included on the $L^{(6)}$ - $L^{(i^*)}$ decision logic in order to prevent chattering, and the original σ estimate (common scale factor) was tightly constrained to prevent incorrect gust level decisions during periods of large pilot activity. These details are documented in Appendix A.

Evaluation emphasis was placed on identification accuracy at fixed flight conditions, test signal requirements, and functional characteristics of the gust level decision logic. The principal results are shown in Figures 8 - 12. These are standard accuracy tests, one each at FC1, FC5, and FC8, and two at FC10′ (h = 914 m, M = 0.8). These tests consist of the same maneuver sequence discussed earlier - 30 seconds of quiescence, a C* doublet, 30 seconds of turbulence, another C* doublet, and quiescence again - all flown with sensor noise and test signals. The traces show uniformly good performance of the gust level decision logic (the channel flag trace) and improved accuracy over the baseline identifier at FC10′ (compare the $\Delta\bar{q}$ traces in Figure 5 and 12). The modified identifier also exhibits lower test signal requirements on the simulator. This is evident in Figure 13 which was run with 0.25 x nominal test signals and shows no noticeable accuracy deterioration over Figure 12.

By comparing Figures 11 and 12 with 8 - 11, it is apparent that the modified identifier still exhibits some residual sensitivity to gust levels ($\simeq$ 20 percent in $\Delta\bar{q}$) in high dynamic pressure flight. We conjecture that this remaining error is due to inaccuracies in the long Newton-Raphson extrapolation

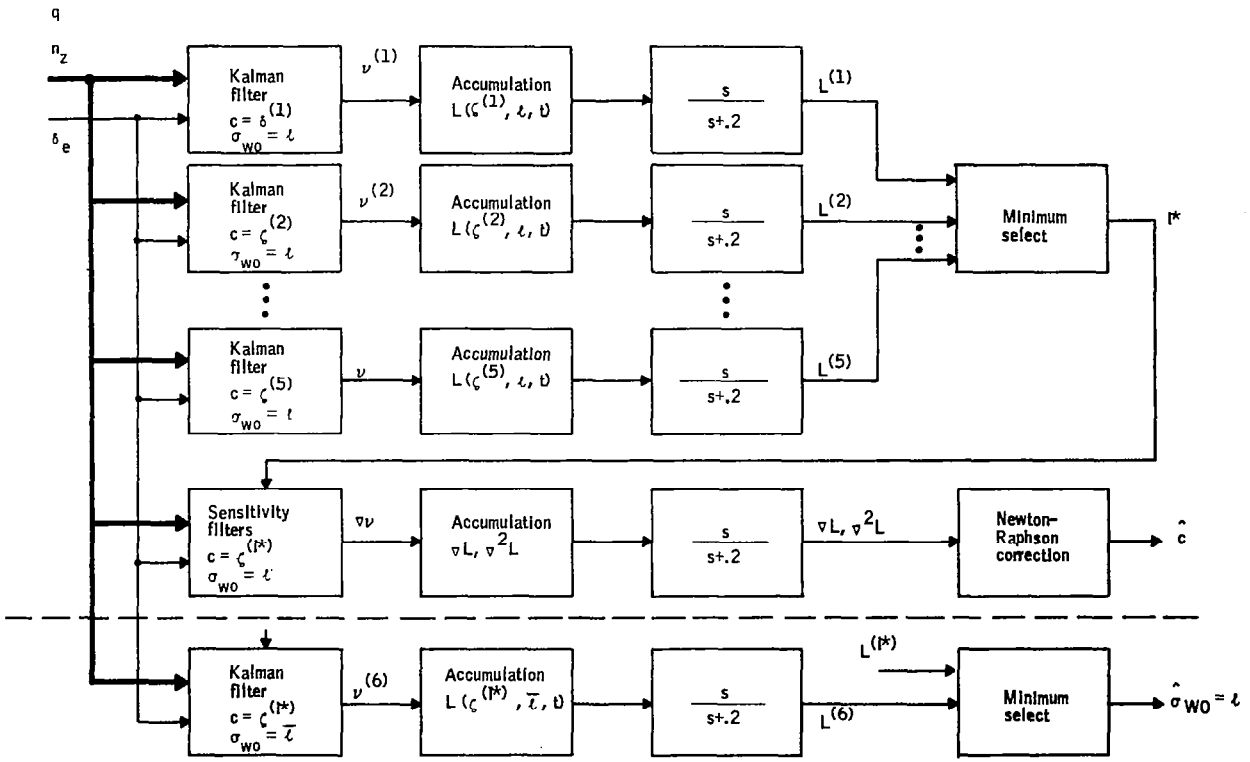

Figure 7. Identifier with Two-Level Gust Estimation

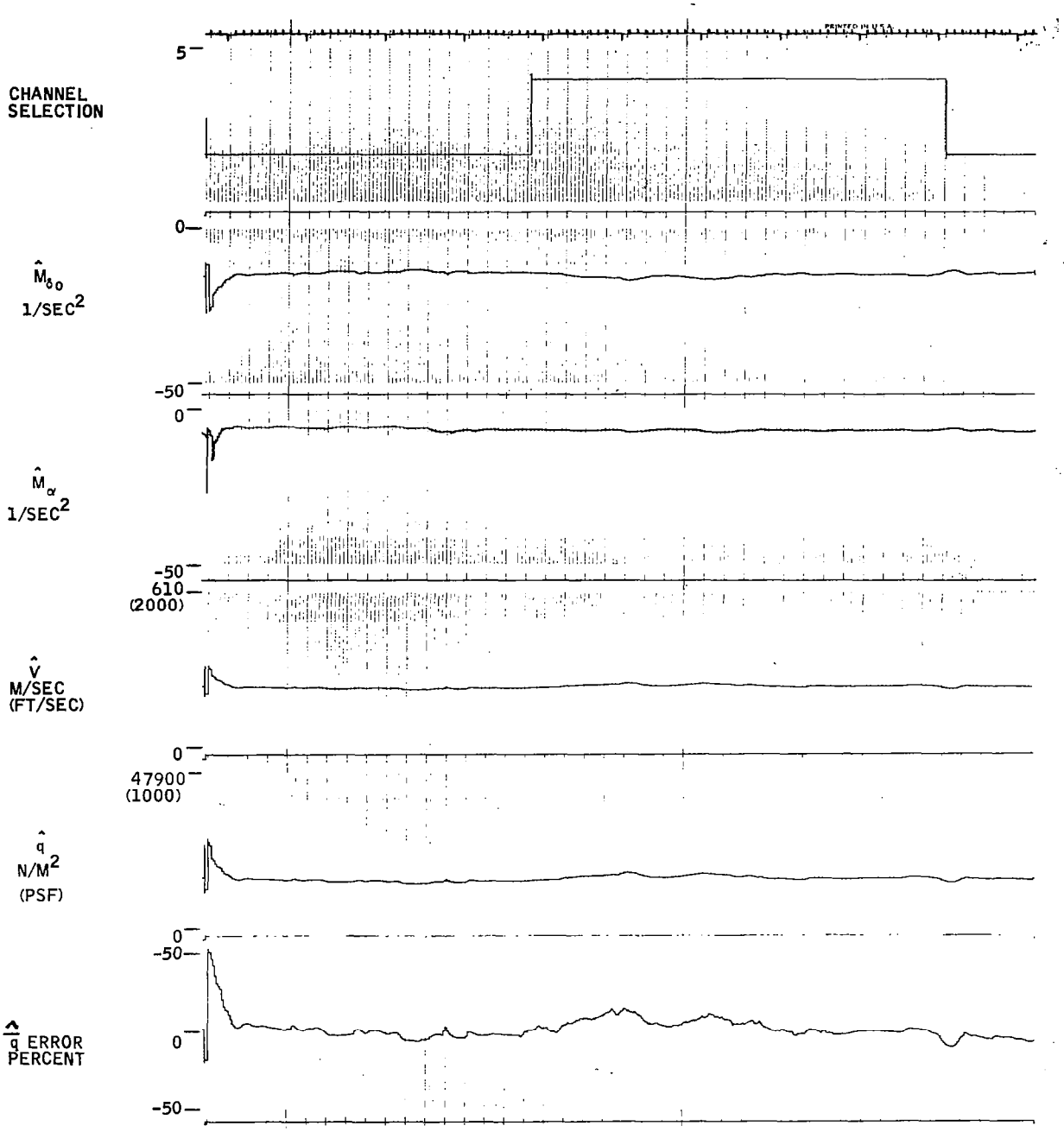

Figure 8. Accuracy Test Traces at FC1 with Gust Level Estimation

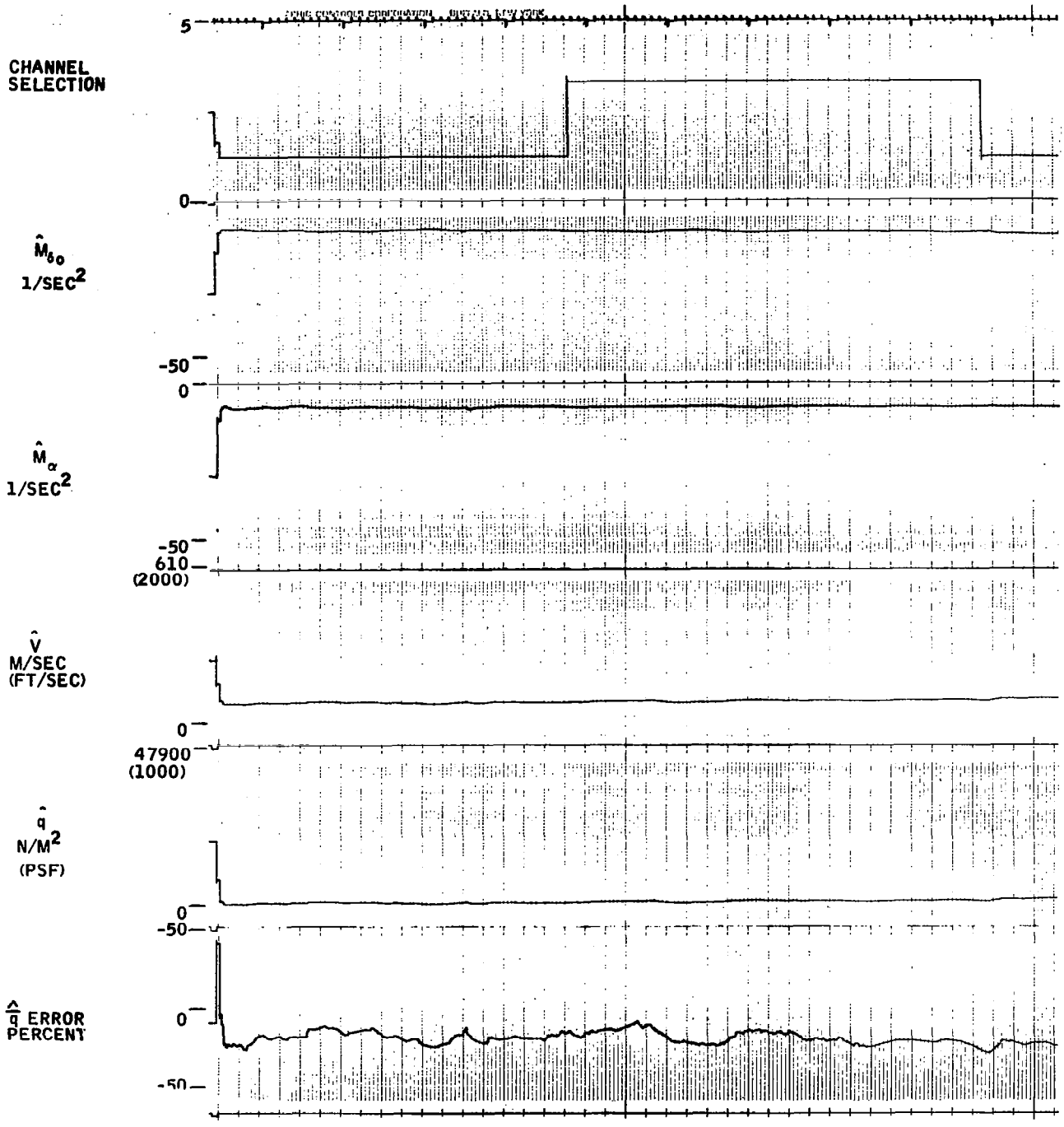

Figure 9. Accuracy Test Traces at FC5 with Gust Level Estimation

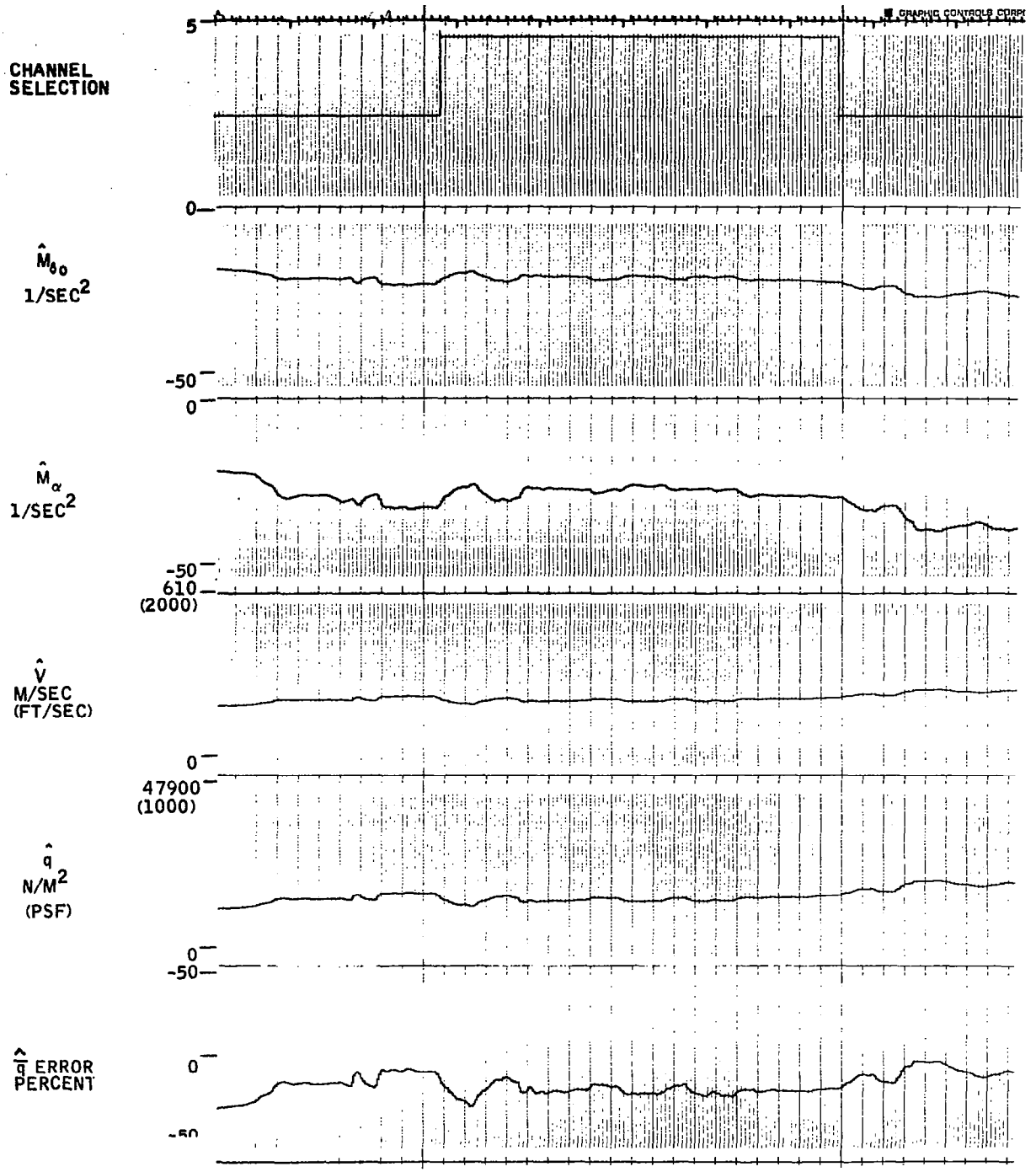

Figure 10. Accuracy Test Traces at FC 8 with Gust Level Estimation

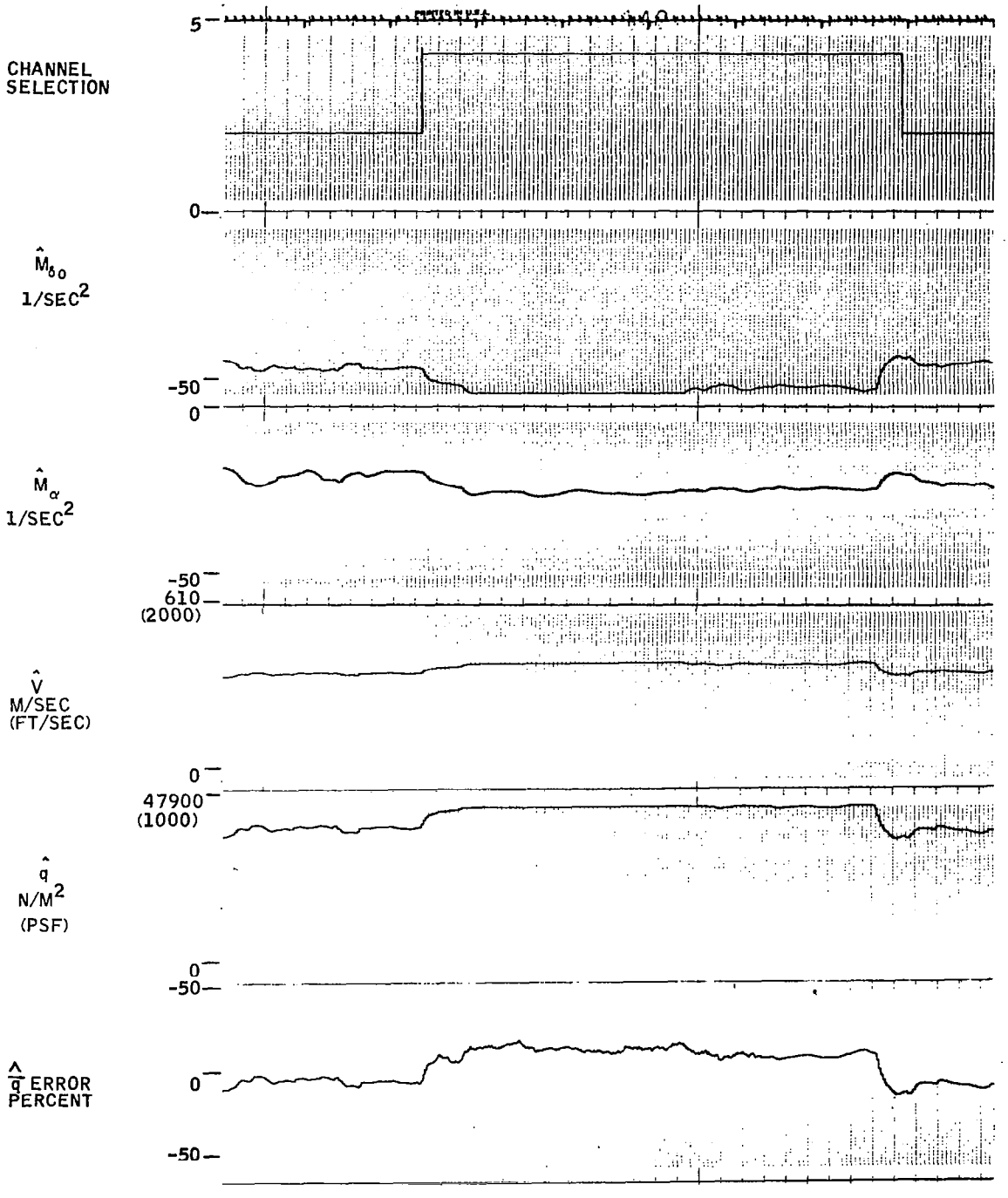

Figure 11. Accuracy Test Traces at FC 10' with Gust Level Estimation (Nominal Test Signal)

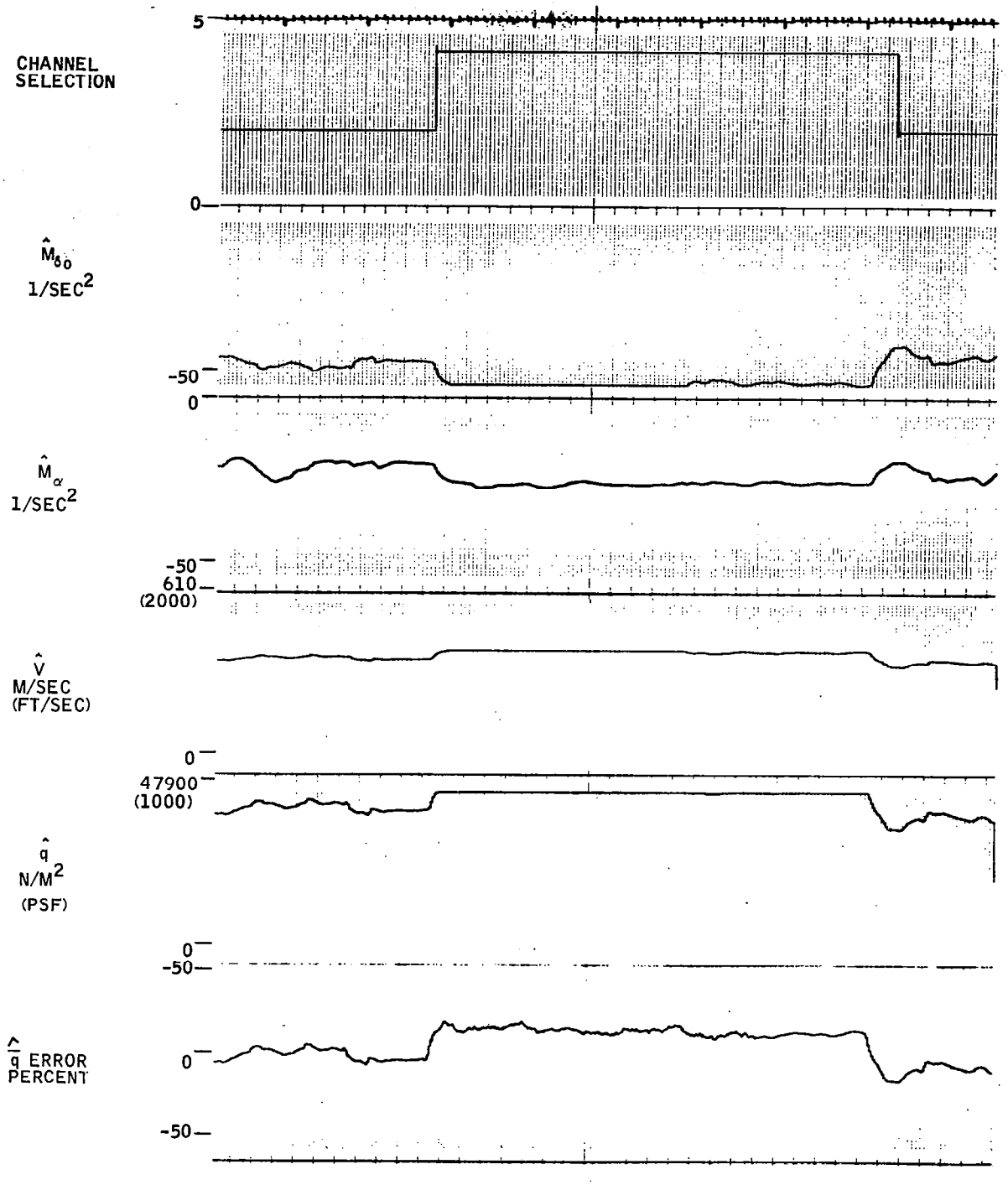

Figure 12. **Accuracy Test Traces at FC 10' with Gust Level Estimation (0.25x Test Signal)**

which must be made from the min-L channel, Channel 4 located at $M_{\delta o} = -26.7$, to the true parameter value at FC10′, $M_{\delta o} \simeq -43$. Figure 4 confirms that this is a significant parameter separation. In theory, of course, the Newton-Raphson step will be accurate only if the likelihood function $L(\zeta, N)$ is quadratic in ζ. This is known to be untrue from experimental plots of the function (ref. 1) and, hence, some extrapolation error must be expected. The conjecture has been further confirmed by locating Channel 4 at $M_{\delta o} = -40$ temporarily. This virtually eliminates the remaining gust sensitivity in Figures 12 and 13.

Incorporation of Attitude Data

The second topic which was investigated for potential accuracy improvements is the use of pitch attitude measurements in the identifier. These measurements were explicitly ruled out for the baseline design because the test aircraft is not equipped with an all-attitude platform. Successful all-attitude operation is a groundrule for the overall adaptive system. This groundrule is relaxed here for the specific purpose of investigating accuracy improvements offered by the use of attitude data.

As always, the investigation began with evaluations of the theoretical identification accuracy achievable with and without pitch attitude measurements. It did not proceed further because these evaluations showed that attitude data has no significant impact on accuracy. Representative results which illustrate this conclusion are given in Table 2. This table compares lower bounds on identification accuracy for six pitch dynamic parameters including the three parameters $M_{\delta o}$, c_2, c_3 recognized by the baseline identifier and three other small perturbation parameters c_1, c_4, c_6 which were neglected due to poor identifiability (ref. 1). The test condition is FC1 with standard test signals, sensor noise and gust levels. The first column in the table represents initial uncertainties (RMS) of the indicated parameters, the second

TABLE 2. - THEORETICAL IDENTIFICATION ACCURACY WITH AND WITHOUT ATTITUDE DATA

Conditions

FC1 - 6090 m, Mach .67

Data Length - 10 sec

Test Signal - .015 g's square wave

Sensor Noise - Gyro 0.15 deg/sec rms
Acceleration 0.02 g's rms
Attitude 0.25 deg rms

Gust Level - 2 m/sec

Accuracy (Lower Bound)

Parameter	A-priori standard deviation	Standard deviation without θ measurement	Standard deviation with θ measurement
C_1 (M_q)	.065	.0552	.0550
C_2 (M_α)	.135	.0394	.0394
C_3 (V)	31.5	26.3	26.3
C_4 (Z_α V)	5.0	4.38	4.38
$M_{\delta o}$	15.0	.408	.404
C_6 (Z_δ V)	.075	.0750	.0750

represents uncertainties after processing 10 seconds of pitch rate and normal acceleration measurements, and the third represents uncertainties after processing 10 seconds of rate, acceleration and pitch attitude measurements. As in (ref. 1), these before-and-after comparisons show that only $M_{\delta o}$, c_2 and to some extent, c_3 can be identified. More importantly, they also show that attitude measurements offer very small accuracy improvements - no more than one percent at best. Such improvements provide insufficient justification for the added complexity required to incorporate pitch measurements in the identifier.

Tracking Aids

The third topic investigated for identifier improvements was the "tracking error" issue. As discussed earlier, tracking errors are inherent in the constant-parameter MLE theory, and the heuristic high-pass filters of the baseline identifier alleviate them only partially. Initial objectives of the investigation were to improve the heuristic high-pass solution by automatically adjusting the high-pass time constants with measured maneuver conditions. This quickly proved ineffective because shorter time constants produce noisier parameter estimates with only modest reduction of tracking error. Despite their lack of success, however, these early efforts contributed increased understanding of the tracking error phenomenon and led eventually to identifier design modifications with much improved tracking capability. A major discovery of the early studies was that tracking errors are caused not only by constant-parameter limitation of the MLE theory (i. e. , lags due to likelihood accumulation) but also by uncompensated trim transients during flight transition. These two error mechanisms are discussed separately below.

Tracking errors due to trim. - The plant model, Figure 3, is valid in the short-period frequency range only, from perhaps 1.0 to 30 rad/sec. This is true despite the presence of the "trim states", g/V and M_o. The latter are crude representations of steady state (trim) disturbance levels which do not properly represent low frequency dynamic behavior such as phugoid motion and trim changes during flight transitions. In fact, the trim states turn out to be only slightly more general than ordinary first order washout filters (high-passes) on the measurements q_m, N_{zm} and δ_m. Hence, they have the same limited capability to compensate for unmodeled low frequency dynamics.

A comparison of low frequency compensation methods with trim states and with washouts is given in Figure 13. In the first method, each channel of the identifier is based on four states (q, α, g/V, M_o) and accepts data directly from the sensors. In the second method, each channel is based on two states (q, α) and accepts data through high-pass filters. Dynamically these two systems are similar. Method 2 has three small real roots at s = -a and one fast second-order root pair for the (closed-loop) Kalman filter. Eigenvalue analysis of the Kalman filters in Method 1 shows almost the same second-order pair and also two small real roots, with exact locations determined by design statistics σ_ϕ and $\sigma_{\delta_{trim}}$. Performance-wise the two systems prove equivalent if design statistics are chosen such that the slow roots in Method 1 are approximately equal to those of Method 2.

Both methods fall short of providing adequate low frequency trim compensation. This is illustrated in Figure 14 which shows traces of individual likelihood function for the five baseline channel locations. The traces were recorded during the standard flight transition in Figure 6. Method 2 was used for trim compensation, with washout frequency $\omega = a = 2.0$. Since the acceleration maneuver starts at FC5, the minimum likelihood function is $L^{(2)}$ immediately before full power is applied. Ideally, $L^{(2)}$ should remain the best channel early in the transition, passing later to $L^{(3)}$, then to $L^{(4)}$ and finally

Method 1: With Trim States

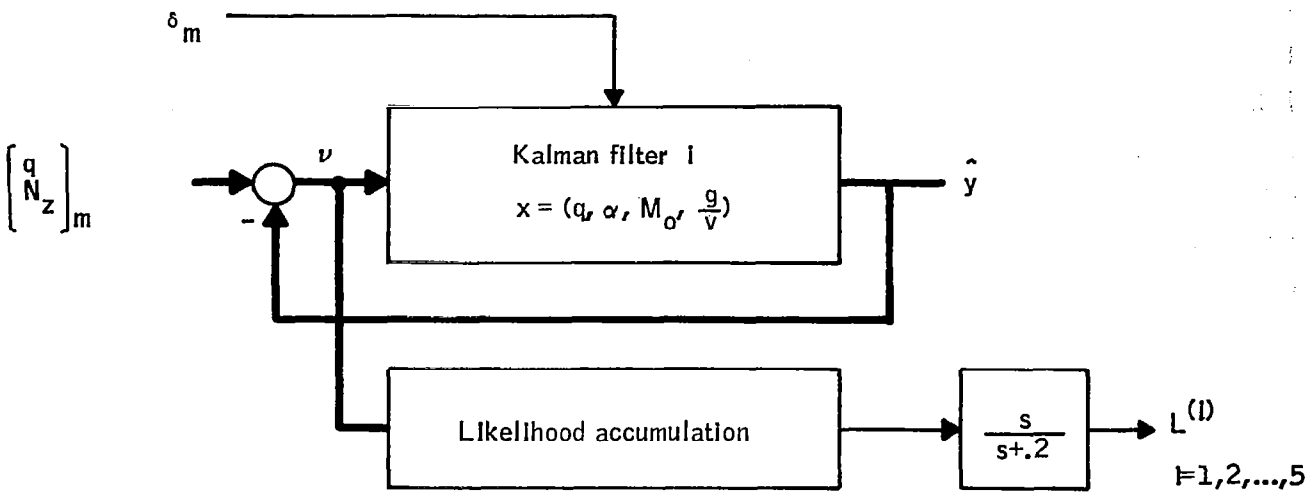

Method 2: With First Order Washouts

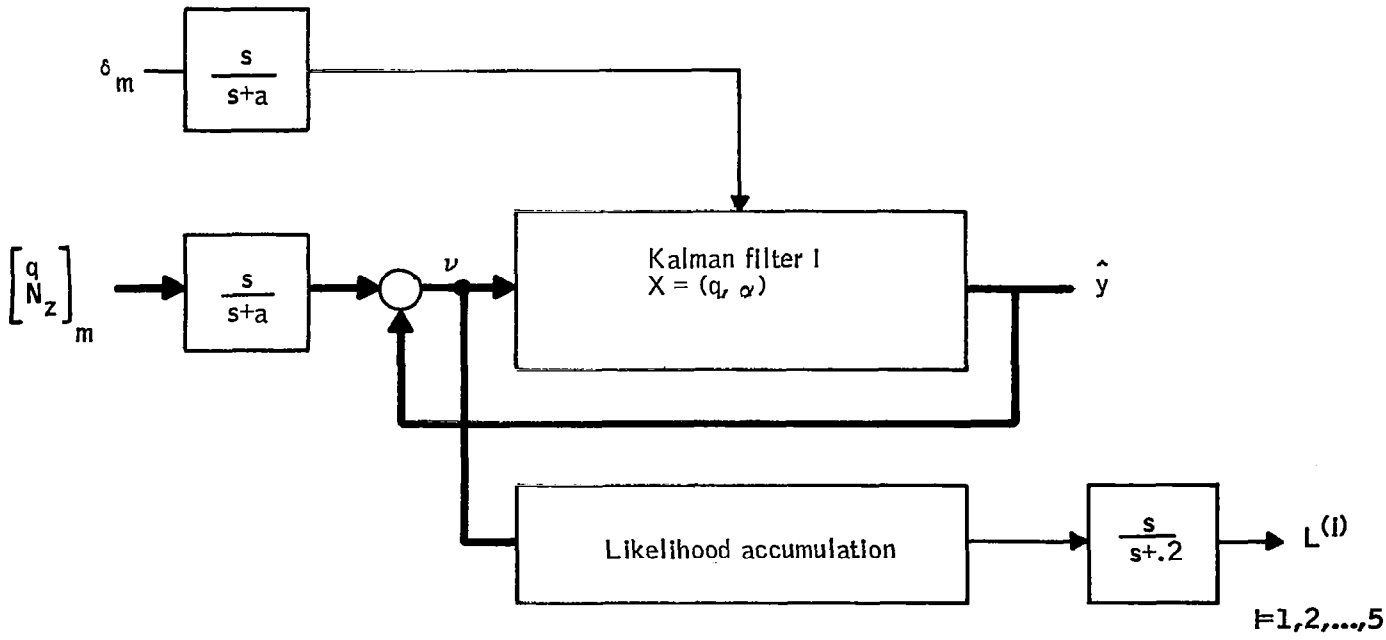

Figure 13. Low Frequency Compensation

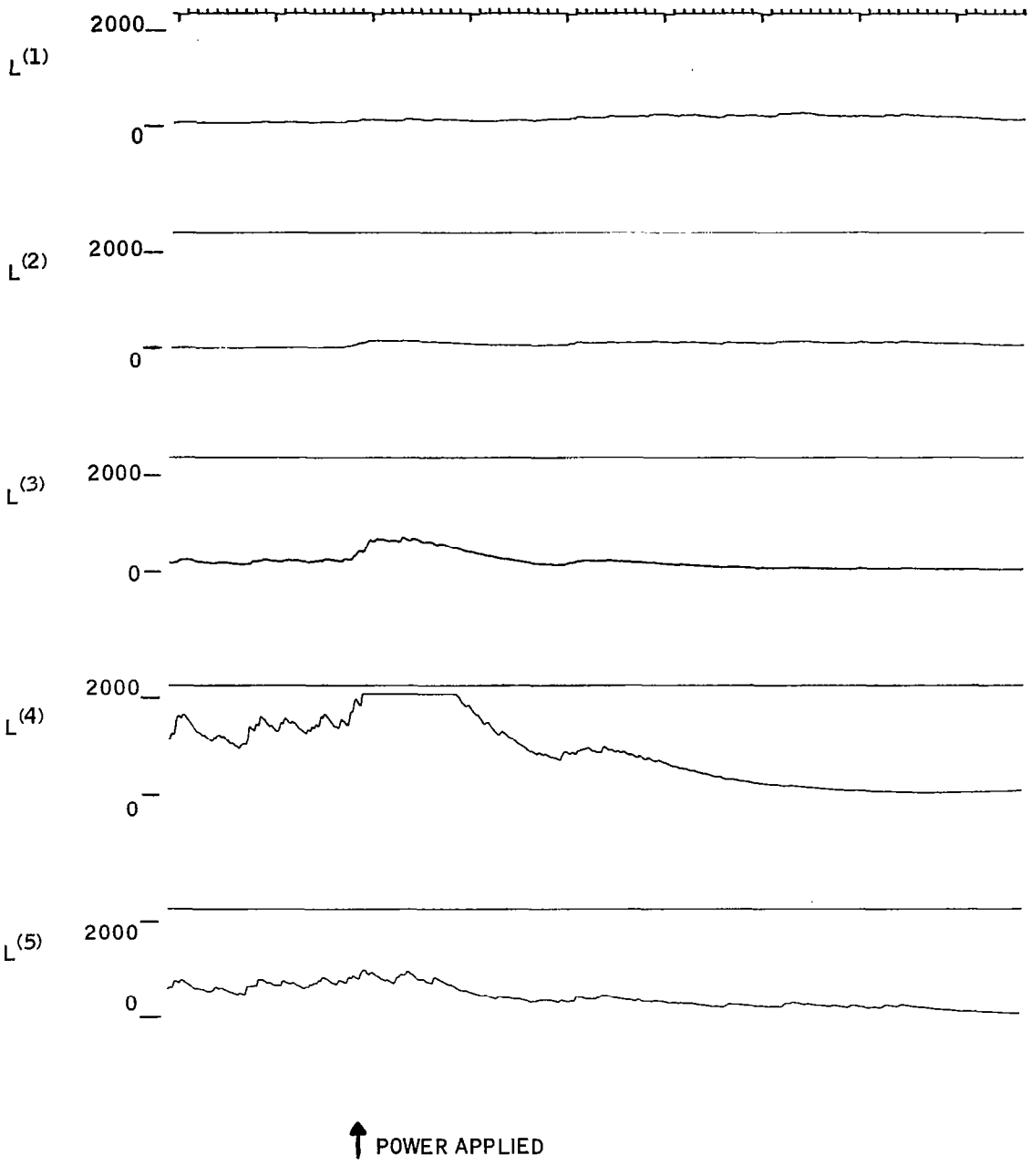

Figure 14. Likelihood Traces During Standard Flight Transition (First Order Trim Compensation, $a_i = 2$)

to the supersonic channel $L^{(5)}$. The run shows that something different actually happens. Large transients appear early in the transition which cause $L^{(1)}$ to minimize initially and pass control back to $L^{(2)}$, $L^{(3)}$, $L^{(4)}$, and $L^{(5)}$ only later in the maneuver. Interpreted in Figure 6, the temporary selection of $L^{(1)}$ over $L^{(2)}$ indicates that incorrect low $|M_{\delta o}|$ values (also low $\bar{q}$ values and negative $\Delta\bar{q}$ values) minimize the likelihood function temporarily.

The fact that these transient errors are at least partly due to inadequate trim compensation is verified in Figure 15. This figure shows likelihood function traces for the same flight transition maneuver but with different trim compensation filters. In addition, all test signals and other external excitation have been removed to highlight trim-induced errors. Two cases are shown, both using second-order washout filters of the form $s^2/(s^2 + 1.5\,\omega s + \omega^2)$. In Case 1 ω is 0.5 rad/sec, and in Case 2 it is 2.0. The traces clearly demonstrate that substantial trim transients exist when the washouts pass signals at low frequencies. For ω sufficiently high, the transients are virtually eliminated. Comparisons of Case 2 and Figure 15 also indicates that second-order washout filters are dramatically superior to first-order filters. This can be explained by the ramp-like character of trim surface position during the standard transition maneuver. Second-order washouts remove ramps much more effectively than first-order washouts.

Based on the above findings, improved second-order trim compensation filters (Method 2) were incorporated in the baseline identifier. Method 2 was selected over Method 1 because the latter requires second-order disturbance models for M_o and g/V in each Kalman filter channel in order to achieve the same performance benefits as three second-order washouts on q_m, N_{zm}, and δ_m, with outputs fed to all channels. The plant model for Method 2 was changed slightly from that implied in Figure 14. It includes δ_e as a state variable in order to permit the identifier to utilize servo position as its control input measurement. Details are given in the flow diagrams of Appendix A.

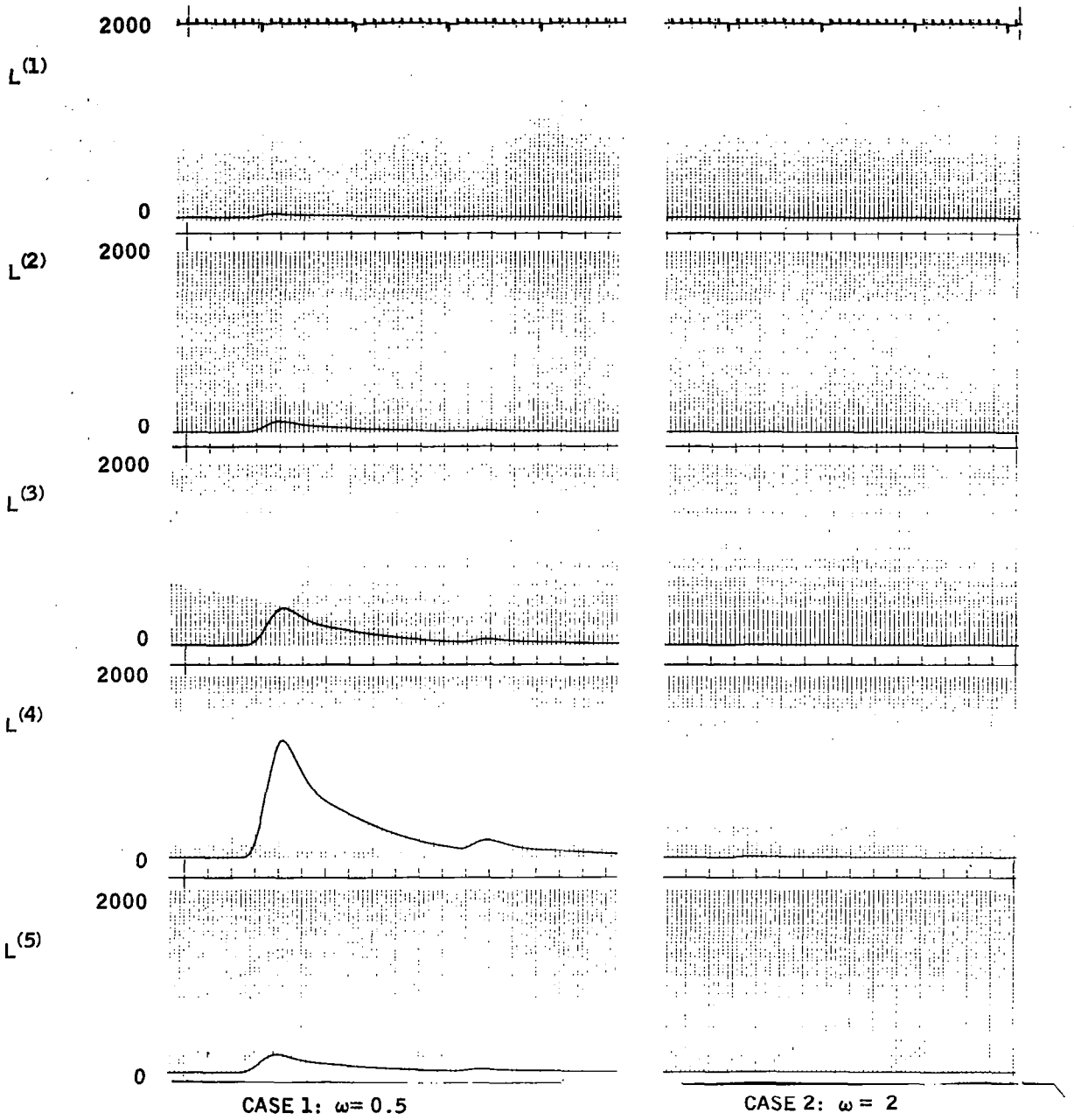

Figure 15. Likelihood Function Traces During Standard Flight Transition (Second Order Trim Compensation)

Tracking performance with these modifications is illustrated in Figure 16. This figure corresponds directly to Figure 5 for the baseline identifier. It is evident that improved trim compensation has reduced the tracking error problem. However, substantial errors still remain. These are due to limitations of MLE theory as discussed next.

Tracking errors due to MLE limitations. - The second principal source of tracking errors can be attributed to fundamental limitations of constant-parameter MLE theory. These limitations can be appreciated most easily in terms of a new interpretation of the baseline parallel-channel algorithm which was developed in the course of the tracking error investigation.

The new interpretation shows that the Newton-Raphson correction of the baseline identifier is entirely equivalent to a Kalman filter which estimates the "states", $\lambda = \underline{c} - \zeta^{(i*)}$, using a constant-parameter model, $\frac{d}{dt}\lambda = 0$, and "measurements" corresponding to the min-L channel residuals. Based on known properties of Kalman filters, this interpretation immediately implies that the estimates will lag behind if λ is in fact not constant. It also suggests that such errors can be alleviated by using other models for the parameter process. In particular, we show below that appropriate models can be selected to derive the heuristic high-pass filters of the baseline identifier. More importantly, parameter models can be selected which give significantly improved tracking performance.

Equivalence of (approximate) Newton-Raphson steps and Kalman filters. - First, we show the Newton-Raphson step (3) with approximate first and second partials equations (6) and (7) is equivalent to a Kalman filter. To do this, note first that the second partials approximation can be generated recursively; i. e.,

$$\text{Let } P_{\ell} \triangleq \left[\sum_{k=1}^{\ell} \nabla \hat{y}_k \, B^{-1} \, \nabla \hat{y}_k^{T}\right]^{-1} \tag{23}$$

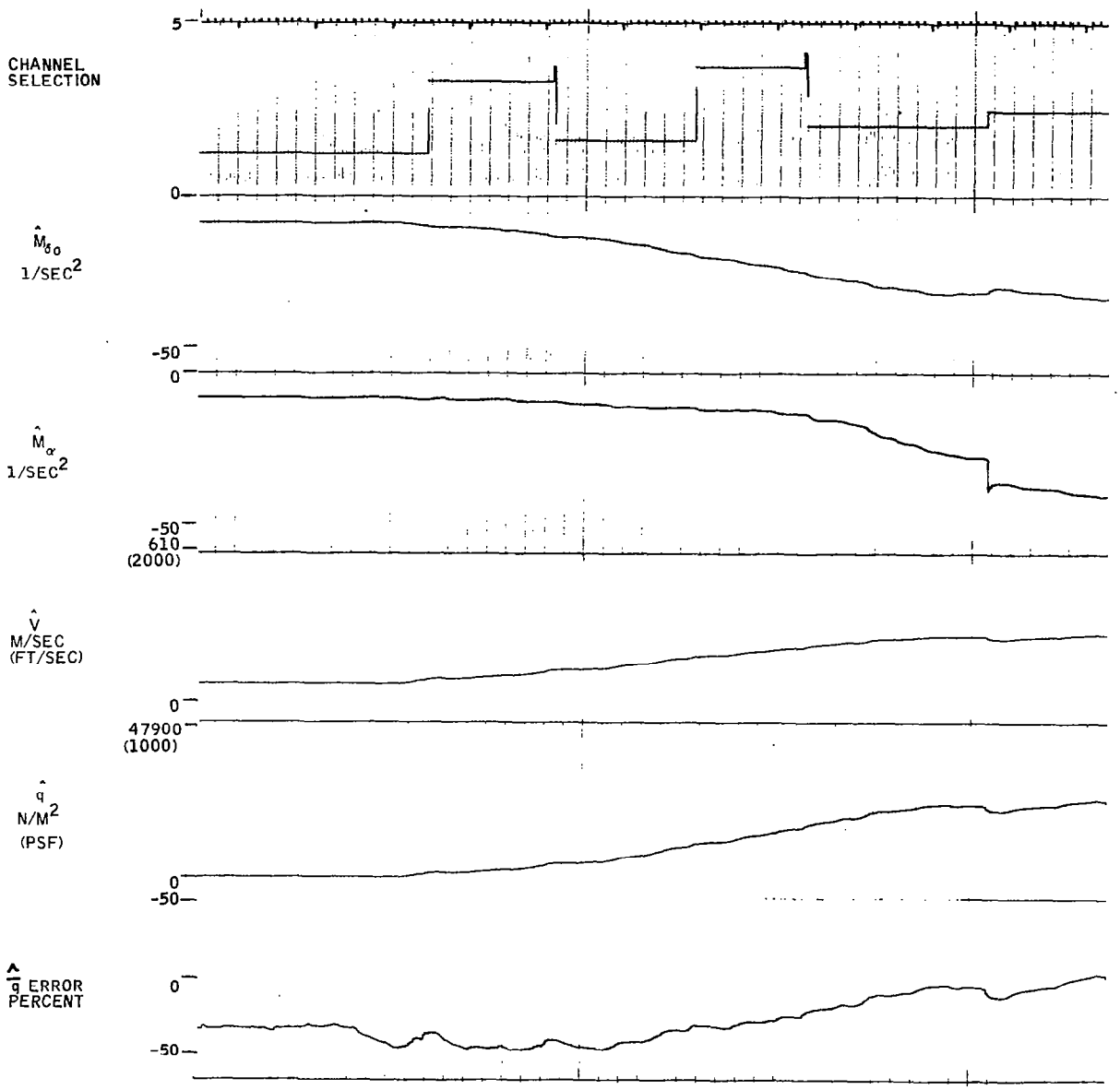

Figure 16. Standard Tracking Traces with Gust Level Estimation and Second Order Trim Compensation

$$\text{Then } P_N = \left[\sum_{k=1}^{N-1} \nabla\hat{y}_k B^{-1} \nabla\hat{y}_k^T + \nabla\hat{y}_N B^{-1} \nabla\hat{y}_N^T \right]^{-1}$$

$$= \left[P_{N-1}^{-1} + \nabla\hat{y}_N B^{-1} \nabla\hat{y}_N^T \right]^{-1} \tag{24}$$

$$= P_{N-1} - P_{N-1} \nabla\hat{y}_N (\nabla\hat{y}_N^T P_{N-1} \nabla\hat{y}_N + B)^{-1} \nabla\hat{y}_N^T P_{N-1}$$

where the last step is based on the "Matrix Inversion Lemma" (ref. 4). Similarly, we can write the entire Newton-Raphson step recursively.

$$\text{Let } \hat{\lambda}_\ell \triangleq \hat{\underline{c}}_\ell - \zeta^{(i^*)} \tag{25}$$

$$\text{Then } \lambda_N = - \left[\sum_{1}^{N} \nabla\hat{y}_k B^{-1} \nabla\hat{y}_k^T \right]^{-1} \left[\sum_{1}^{N} - \nabla\hat{y}_k B^{-1} \nu_k \right]$$

$$= P_N P_{N-1}^{-1} P_{N-1} \left(\sum_{1}^{N-1} \nabla\hat{y}_k B^{-1} \nu_k \right) + \nabla\hat{y}_N B^{-1} \nu_N \tag{26}$$

$$= P_N \left[P_{N-1}^{-1} \hat{\lambda}_{N-1} + P_N \nabla\hat{y}_N B^{-1} \nu_N \right]$$

Now note that equation (24) implies

$$P_N P_{N-1}^{-1} = I - P_{N-1} \nabla\hat{y}_N (\nabla\hat{y}_N^T P_{N-1} \nabla\hat{y}_N + B)^{-1} \nabla\hat{y}_N^T \tag{27}$$

and

$$P_N \hat{\nabla y}_N B^{-1} = P_{N-1} \hat{\nabla y}_N \left[I - (\hat{\nabla y}_N^T P_{N-1} \hat{\nabla y}_N + B)^{-1} \hat{\nabla y}_N^T P_{N-1} \hat{\nabla y}_N \right] B^{-1} \tag{28}$$

$$= P_{N-1} \hat{\nabla y}_N (\hat{\nabla y}_N^T P_{N-1} \hat{\nabla y}_N + B)^{-1}$$

Substituting these into equation (11) gives

$$\hat{\lambda}_N = \hat{\lambda}_{N-1} + P_{N-1} \hat{\nabla y}_N (\hat{\nabla y}_N^T P_{N-1} \hat{\nabla y}_N + B)^{-1} \left[\nu_N - \hat{\nabla y}_N^T \hat{\lambda}_{N-1} \right] \tag{29}$$

Equations (29) and (24) can be recognized as Kalman filter and covariance equations for the following system model and measurement equation:

$$\begin{aligned} \lambda_N &= \lambda_{N-1} \\ m_N &= \nu_N = \hat{\nabla y}_N^T \lambda_N + \nu^*_N \end{aligned} \tag{30}$$

where ν^* is a white noise sequence with $E(\nu^*_k \nu^*_\ell) = B\delta_{k\ell}$.

Hence, with proper initial conditions on equations (29) and (24), the approximate Newton-Raphson step, equation (3), is equivalent to a Kalman filter for a constant parameter process with "measurements" taken to be the filter residuals, equation (4), of the (i*)-th parallel channel. Moreover, these "measurements" are treated as linear functions of the parameter error of that channel; i. e.,

$$\nu_N \simeq \hat{\nabla y}_N^T \left[c_N - \zeta^{(i*)} \right] + \nu^*_N, \tag{31}$$

with "measurement noise", ν^*, corresponding to the theoretical residual sequence (innovations) under assumptions $c = \zeta^{(i^*)}$.

Identification of time varying parameters. - With the above Kalman filter interpretation, extensions of the parallel-channel concept to time-varying parameters become self-evident.

Case 1: First-order time variation: The simplest extension is to assume that the parameters are first order Brownian motion processes with growth rate Q_λ instead of constants. Then the Newton-Raphson correction of Figure 2 would be replaced by the following Kalman filter:

$$\hat{\lambda}_N = \hat{\lambda}_{N-1} + M_{N-1}\,\hat{\nabla y}_N(\hat{\nabla y}_N^T\, M_{N-1}\,\hat{\nabla y}_N + B)^{-1}\,(\nu_N - \hat{\nabla y}_N^T\,\hat{\lambda}_{N-1}) \quad (32)$$

$$M_{N-1} = P_{N-1} + Q_\lambda \quad (33)$$

$$P_N = M_{N-1} - M_{N-1}\,\hat{\nabla y}_N(\hat{\nabla y}_N^T\, M_{N-1}\,\hat{\nabla y}_N + B)^{-1}\,\hat{\nabla y}_N^T\, M_{N-1} \quad (34)$$

This filter provides first order tracking characteristics: zero steady state error for constant parameters, lag errors inversely proportional to $K\hat{\nabla y}^T = M\,\hat{\nabla y}(\hat{\nabla y}^T M \hat{\nabla y} + B)^{-1}\,\hat{\nabla y}^T$ for ramp parameter changes, and unbounded errors for all higher-order parameter variations. These characteristics are much like the tracking behavior achieved with the heuristic high-pass filters added in Figure 2. In fact, the heuristic high-passes are entirely equivalent to equations (32), (33), and (34) for a particular choice of Q_λ, namely

$$Q_\lambda = P_{N-1}(1 - \mu)/\mu \quad (35)$$

with

$$\mu = \exp(-\Delta t/\tau).$$

To verify this, we substitute equation (35) into equations (32), (33), and (34) and work backwards through the steps in equations (23) through (29). First, consider the covariance equations.

$$
\begin{aligned}
M_{N-1} &= P_{N-1} + Q_\lambda = P_{N-1}/\mu \\
P_N &= \left[M_{N-1}^{-1} + \nabla\hat{y}_N \, B^{-1} \, \nabla\hat{y}_N^T \right]^{-1} \\
&= \left[\mu \, P_{N-1}^{-1} + \nabla\hat{y}_N \, B^{-1} \, \nabla\hat{y}_N^T \right] \\
&= \left\{ \mu \left[\mu \, P_{N-1}^{-1} + \nabla\hat{y}_{N-1} \, B^{-1} \, \nabla\hat{y}_{N-1}^T \right] + \nabla\hat{y}_N \, B^{-1} \, \nabla\hat{y}_N^T \right\} \\
&\quad \bullet \\
&\quad \bullet \\
&\quad \bullet \\
P_N &= \left\{ \sum_{k=1}^{N} \mu^{(N-k)} \, \nabla\hat{y}_k \, B^{-1} \, \nabla\hat{y}_k^T \right\}
\end{aligned}
\tag{36}
$$

Hence, P_N [defined by equations (33) and (34)] is equivalent to P_N of equation (23), except with exponentially deweighted summands. Similar arguments apply to the estimator equation. Rewrite equation (32):

$$
\begin{aligned}
\hat{\lambda}_N &= \left[I - M_{N-1} \, \nabla\hat{y}_N (\nabla\hat{y}_N^T \, M_{N-1} \, \nabla\hat{y}_N + B)^{-1} \, \nabla\hat{y}_N^T \right] \hat{\lambda}_{N-1} \\
&\quad + M_{N-1} \, \nabla\hat{y}_N (\nabla\hat{y}_N^T \, M_{N-1} \, \nabla\hat{y}_N + B)^{-1} \, \nu_N .
\end{aligned}
\tag{37}
$$

Then reverse equations (27) and (28):

$$
\begin{aligned}
\left[I - M_{N-1} \, \nabla\hat{y}_N (\nabla\hat{y}_N^T \, M_{N-1} \, \hat{y}_N + B)^{-1} \, \nabla\hat{y}_N^T \right] &= P_N \, M_{N-1}^{-1} \\
&= P_N (\mu \, P_{N-1}^{-1})
\end{aligned}
\tag{38}
$$

$$M_{N-1}\,\hat{\nabla y}_N(\hat{\nabla y}_N^{T}\,M_{N-1}\,\hat{\nabla y}_N + B)^{-1} = P_N\,\hat{\nabla y}_N B^{-1} \tag{39}$$

Now, substitute these results into equation (37):

$$\begin{aligned}
\hat{\lambda}_N &= P_N\left[\mu\,P_{N-1}^{-1}\,\hat{\lambda}_{N-1} + \hat{\nabla y}_N\,B^{-1}\,\nu_N\right] \\
&= P_N\Big\{\mu\,P_{N-1}^{-1}\left[P_{N-1}(\mu P_{N-1}^{-1}\,\hat{\lambda}_{N-2} + \hat{\nabla y}_{N-1}\,B^{-1}\,\nu_{N-1})\right] \\
&\qquad + \hat{\nabla y}_N B^{-1}\,\nu_N\Big\} \\
&\;\;\circ \\
&\;\;\circ \\
&\;\;\circ \\
\hat{\lambda}_N &= P_N\left\{\sum_{k=1}^{N}\mu^{(N-k)}\,\hat{\nabla y}_k\,B^{-1}\,\nu_k\right\}.
\end{aligned} \tag{40}$$

This is equivalent to equation (25) with exponentially deweighted summands. Hence, first-order Brownian motion parameter models result in the heuristic high-pass filters for appropriate choice of Q.

Case 2: Second-order time variation: The filter [equations (32), (33), and (34)] can obviously be modified to track higher-order parameter variations. For the F-8C in particular, ramp parameter variations are common during level accelerations, dives, or climbs. Zero steady state errors for these changes can be achieved with second-order parameter variation models such as the following:

$$\lambda_k = \lambda_{k-1} + \Delta t\, \dot{\lambda}_{k-1}$$

$$\dot{\lambda}_k = \dot{\lambda}_{k-1} + w_{k-1} \qquad E(w_k w_\ell^T) = Q_\lambda^{\cdot}\, \delta_{k\ell} \tag{41}$$

$$m_k = \hat{\nabla y}_K\, \lambda_k + \nu^*_k$$

Kalman filters for this model work quite well for F-8C flight transitions. An example is shown in Figure 18. This figure compares the tracking performance of the baseline Newton-Raphson step (equation 3) with heuristic exponential deweighting against the performance of Kalman filters designed for model, equation (41). The flight transitions were generated with linear time-varying perturbation equations, and hence do not include tracking errors due to trim transients. They approximate rapid level-flight acceleration using a hypothetical engine three times as powerful as the F-8C's. Standard random test signals were applied with less than 0.04 g's rms acceleration levels at the pilot station (ref. 1). Figure 17 clearly demonstrates the superiority of second-order parameter models for ramp-like parameter variations.

Other Features

In addition to these time variation solutions, the Kalman filter interpretation above suggests two other potential improvements of the overall identifier. The first concerns the use of residual data from several parallel identifier channels. Recall that the Kalman filter interpretation treats the min-L channel as a sensor whose "measurement" is the channel's residual sequence. It follows that other parallel channels with small likelihood functions can be viewed as additional sensors and a single Kalman filter can be designed to combine several such channel "measurements". These sensors will have correlated measurement noise, of course, because each residual sequence

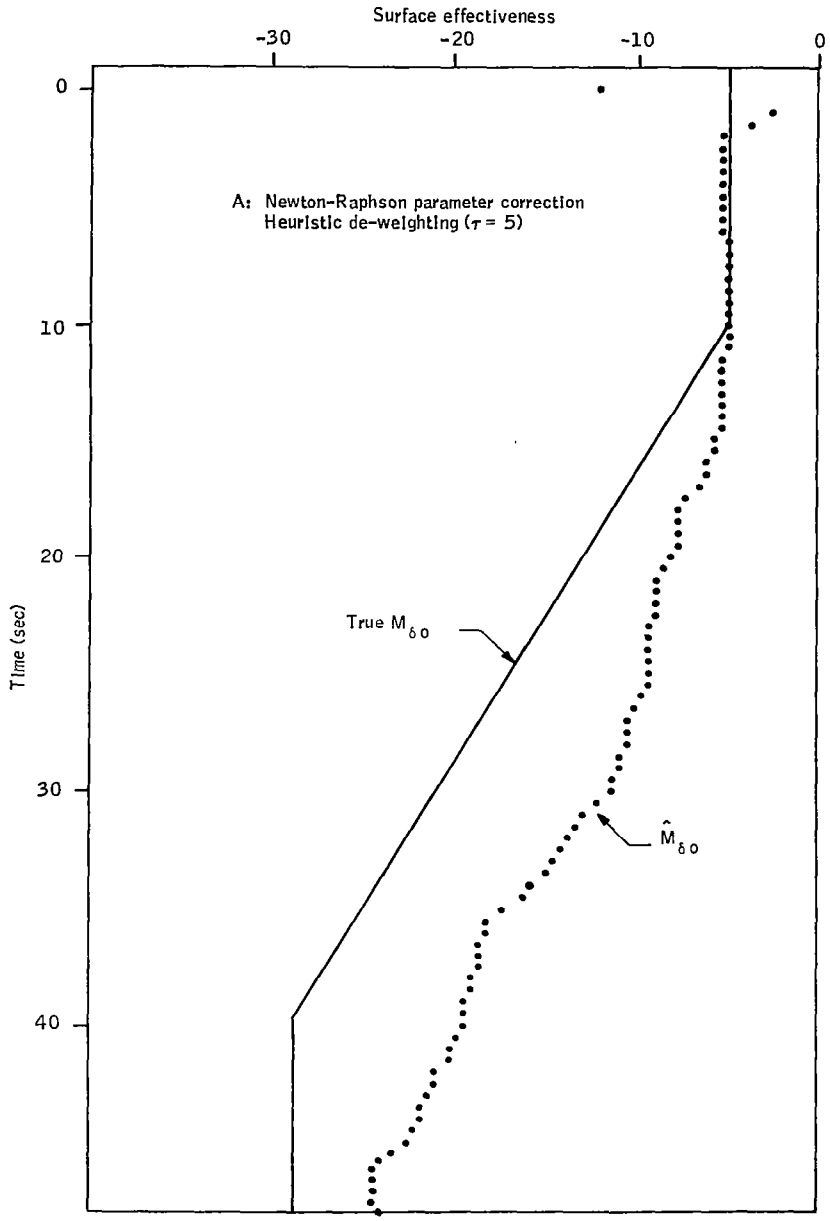

Figure 17. F-8C Identification

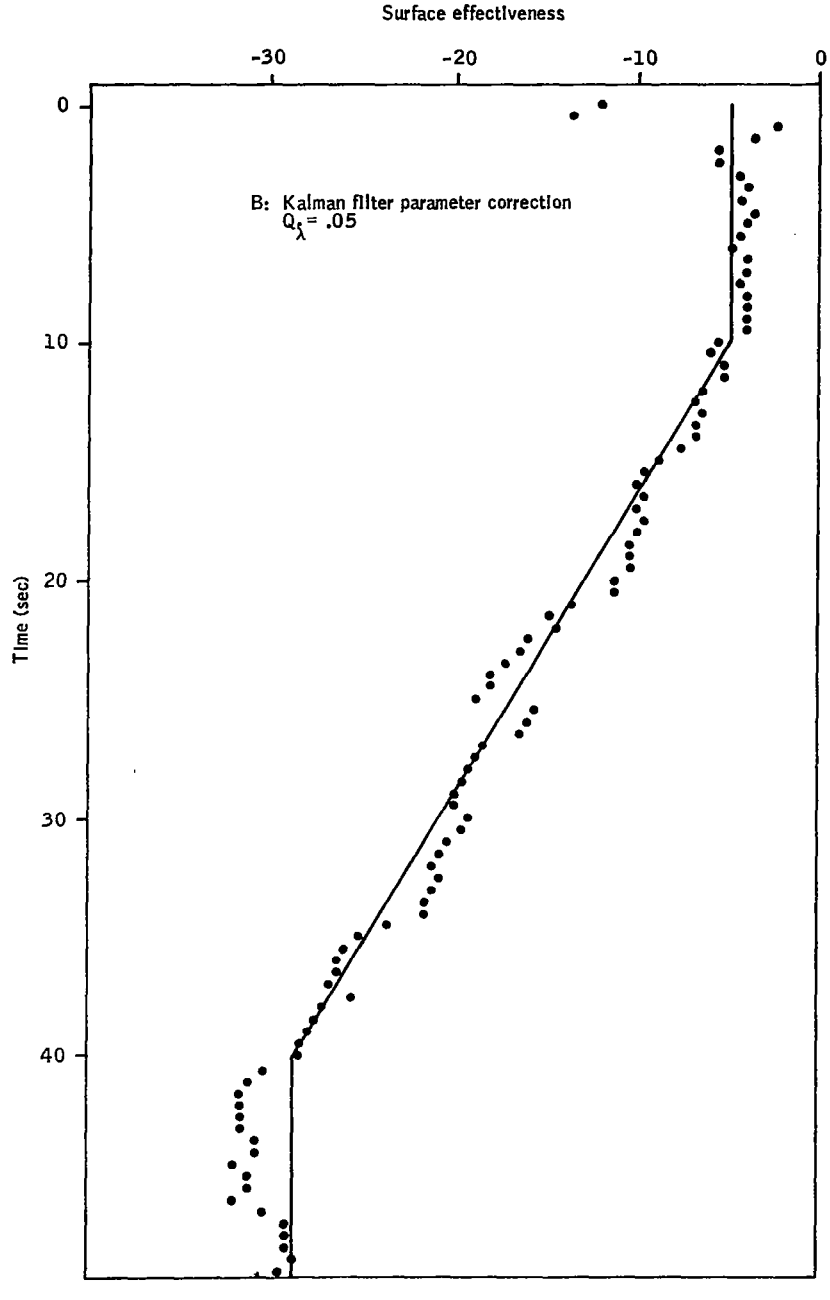

Figure 17. F-8C Identification (Continued)

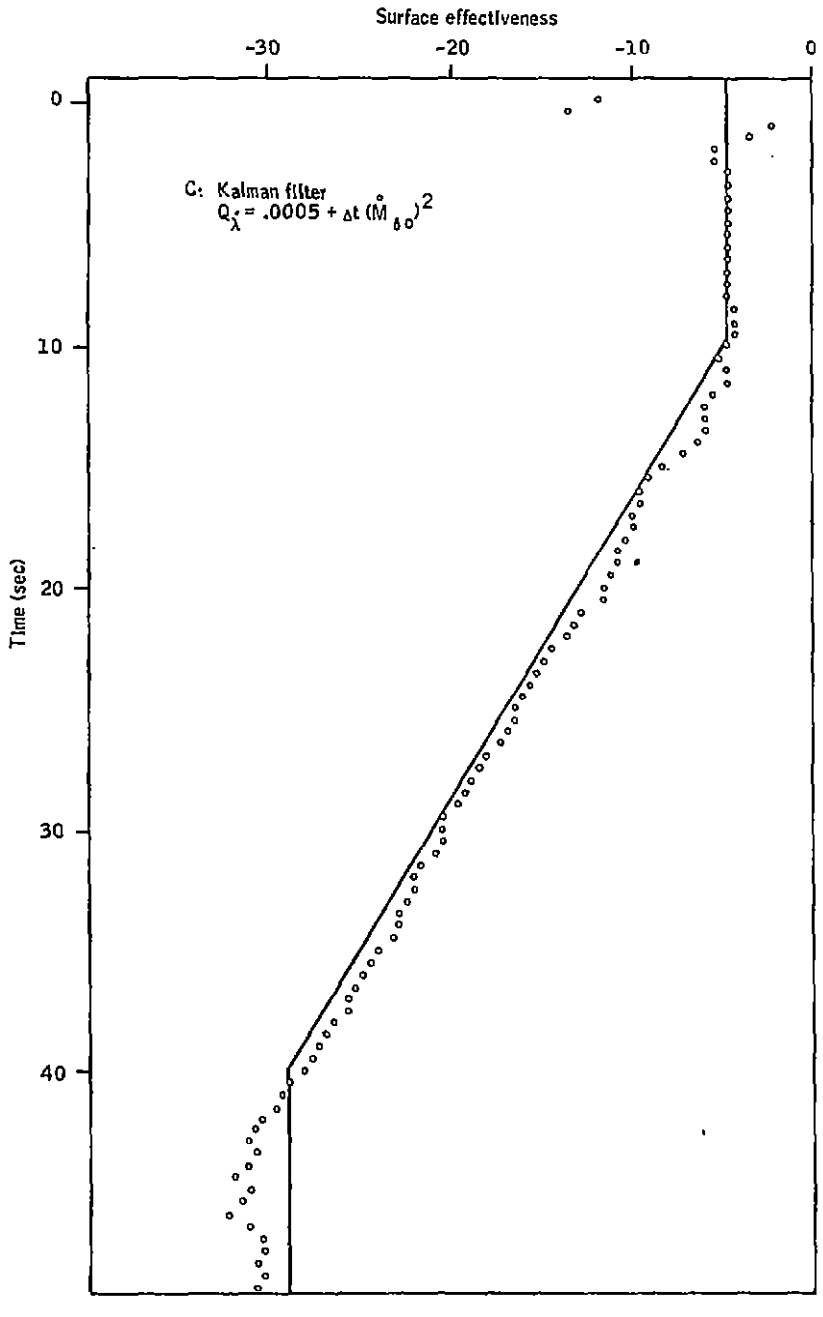

Figure 17. F-8C Identification (Continued)

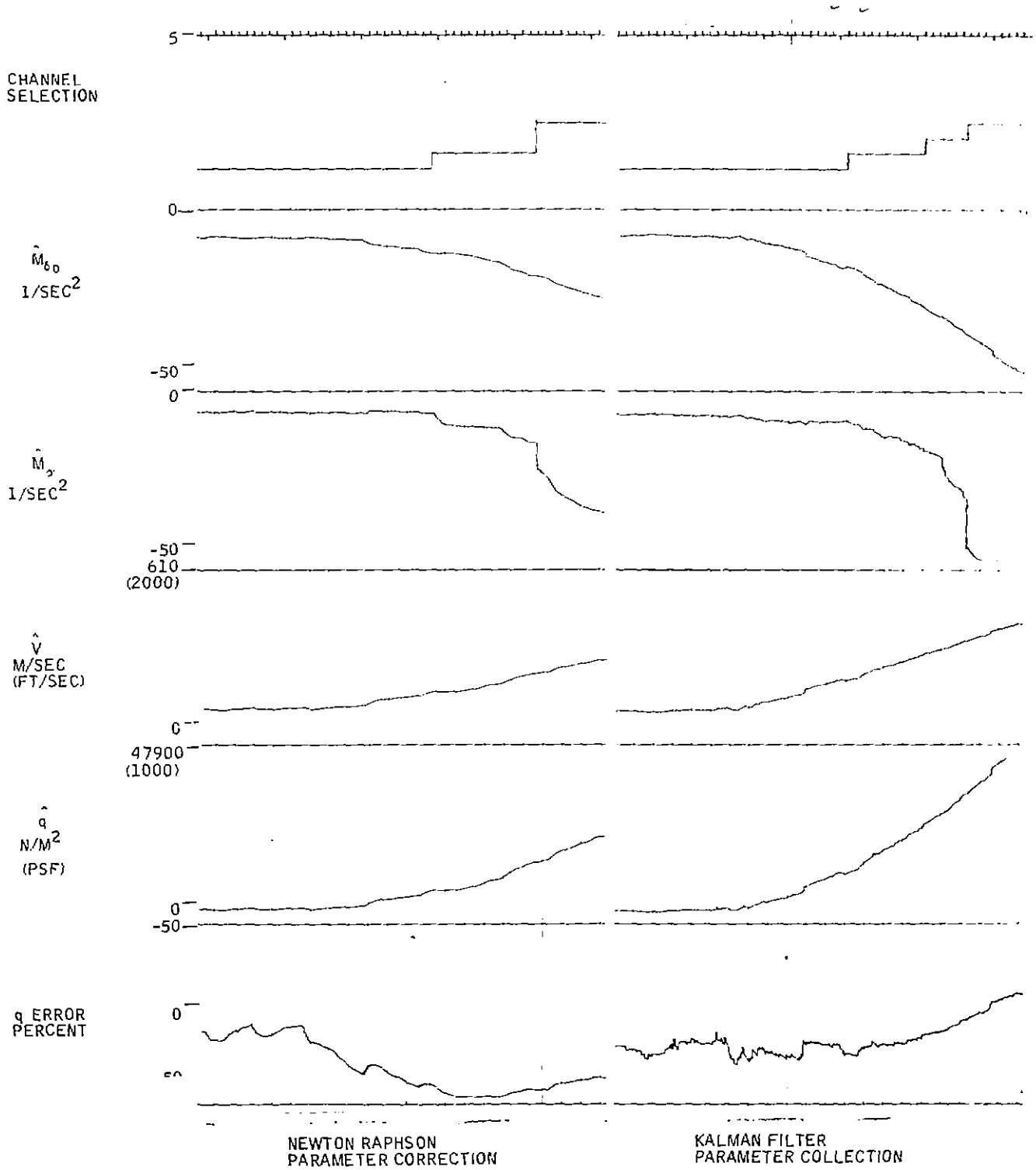

Figure 17. F-8C Identification (Concluded)

results from the same basic data sequence $Y_{\hat{N}}$. Sensitivity solutions would be required for each added channel (to get ∇y) and, hence, a tradeoff between accuracy improvements and added computations is called for. These questions were not investigated under the current program.

The second potential improvement concerns the use of other external data about parameter variations. In the F-8C case, for example, an approximate time derivative of $\bar{q}$ (and hence $M_{\delta o}$) can be constructed from three-axis accelerometers and attitude sensors as follows:

$$\bar{q} = \frac{1}{2} \rho V^2$$

$$\frac{d}{dt} \bar{q} = \frac{1}{2} \frac{d\rho}{dh} \frac{dh}{dt} V^2 + \rho V \frac{dV}{dt}$$

$$= \bar{q} \frac{1}{\rho} \frac{d\rho}{dh} \frac{dh}{dt} + \frac{2}{V} \frac{dV}{dt}$$

Substituting the approximations

$$M_{\delta o} \simeq -22 \bar{q}, \qquad \text{Reference [1]}$$

$$\frac{1}{\rho} \frac{d\rho}{dh} \simeq -.00001 \text{ m}^{-1}, \qquad \text{Reference [5]}$$

$$\left.\begin{aligned} \frac{dh}{dt} &\simeq V(\sin \theta - \alpha \cos \theta \cos \phi), \\ \frac{dV}{dt} &\simeq a_x + \alpha a_z - g (\sin \theta - \alpha \cos \theta \cos \phi), \end{aligned}\right\} \text{small } \beta$$

gives

$$\frac{d}{dt} M_{\delta o} \simeq \frac{2M_{\delta o}}{V} \left[a_x + \alpha a_z - \left(g + \frac{V^2}{200\,000}\right) (\sin\theta - \alpha \cos\theta \cos\phi) \right]$$

$$\simeq \frac{2M_{\delta o}}{V} \left[a_x + \alpha a_z - g(\sin\theta - \alpha\cos\theta \cos\phi) \right] \tag{42}$$

As above, this data can be treated as added measurements in the parameter variation model to be incorporated directly in the Kalman filter design. The data can also be used to adjust the statistics of parameter variations on-line. This was done to generate Figure 17C.

Theoretical Validity

It is important to recognize that the parallel-channel concept with Kalman filter corrections instead of Newton-Raphson steps is still an approximate solution of the theoretical "time-varying identification problem". After all, the identification problem posed by equation (1) with dynamics appended for parameters $\underline{c}$ is really a nonlinear filtering problem. These generally required infinite dimensional solutions. The degree to which the parallel concept is valid, however, can be assessed qualitatively from equation (31). The concept depends fundamentally on the assumption that the residual sequence of the min-L channel is equal to the theoretical innovations process plus linear functions of the parameter error. It can be shown that this assumption is fully satisfied under the following two conditions:

- Parameters $\underline{c}$ enter only in the matrices G and D of equation (1). All other matrices are known.
- The functional dependence of G and D on $\underline{c}$ is linear.

Because these special conditions assure linear residuals for all channel locations, they are further distinguished by requiring only one channel in the parallel-channel structure. Under other conditions, equation (31) holds only approximately. The approximation is good if the min-L channel is sufficiently close to the true parameter value and if, simultaneously, the parameter rates of change are sufficiently small.

SECTION 4
LATERAL ADAPTIVE CONTROL

This section presents the design of the lateral axis adaptive algorithm. The design includes a first order Kalman filter that uses a maximum likelihood procedure to estimate air data dependent aircraft parameters. The filter is initialized by the pitch axis identifier and provides refined estimates of angle-of-attack, true airspeed, and surface effectiveness. These are used to schedule gains in an "inertially coordinated" lateral control law.

In addition we include inertial turn coordination requirements, parameterizations and theoretical identifiability results for the lateral axis. Finally, we show the performance of the adaptive design on Langley's F-8C simulator.

Inertial Turn Coordination

"Inertial coordination" is a way to achieve good dutch roll damping and good turn coordination at all angles of attack. The basic principle of the method is illustrated in Figure 18. It consists of maintaining stability-axis yaw rate at the value needed to balance centrifugal and gravity forces along the body y-axis. This balanced condition corresponds to coordinated turns. The required rate is

$$\begin{aligned} r_s &= r - \alpha p \\ &= \frac{g}{V} \cos\theta \sin\phi \end{aligned} \tag{43}$$

The inertial coordination principle has been used to develop several flight-quality lateral-directional control laws. One design is part of the F-8C CCV package (ref. 6). It was derived using optimal control theory with

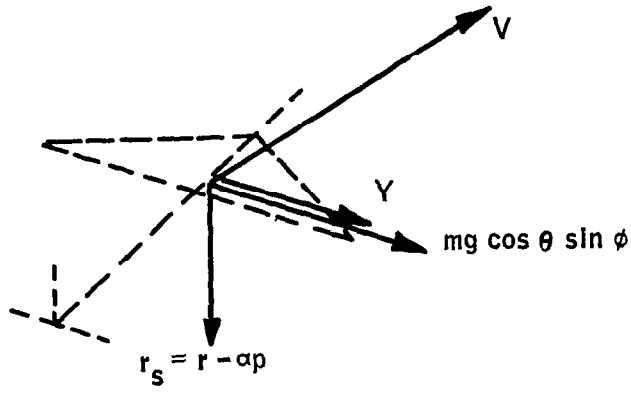

$$mVr_s = mg \cos\theta \sin\phi + Y$$

$$Y = 0 \qquad r_s - \frac{g}{V} \cos\theta \sin\phi = 0$$

Figure 18. Inertial Turn Coordination

quadratic penalties on control effort, on roll rate model-following error (p_m-p), and on the error (ϵ) between actual and desired stability-axis yaw rate, i.e.,

$$\epsilon = r_{s\,(\text{derived})} - r_s$$
$$= \frac{g}{V}\cos\theta\,\sin\phi - (r - \alpha p) \qquad (44)^*$$

The latter was included specifically to achieve turn coordination by means of inertial coordination. The block diagram that resulted after simplification is shown in Figure 19. It includes a dominant ϵ-feedback to the rudder for damping and coordination plus various other state feedbacks and crossfeeds. The gains $K_{A\epsilon}$, K_{RP}, K_{RUM}, K_{RPM} are scheduled with α. Their scheduling functions were developed from optimal controllers designed for a set of flight conditions. Expressions for the functions are given in Table 3.

A second lateral CAS using the inertial coordination principle but designed by frequency domain methods was flight-tested as part of the Air Force's A-7D Multimode Program. Flight results have confirmed improved damping and turn coordination properties over conventional yaw dampers (ref. 7).

*The error ϵ is sometimes called a kinematic sideslip rate since it can be derived from an expression for $\dot{\beta}$ by assuming the side forces are zero (i.e., $Y_\beta\beta + Y_{\delta r}\delta r \doteq 0$). Then $\dot{\beta} = \alpha p - r + \frac{g}{V}\sin\phi\cos\theta$ which is equal to ϵ.

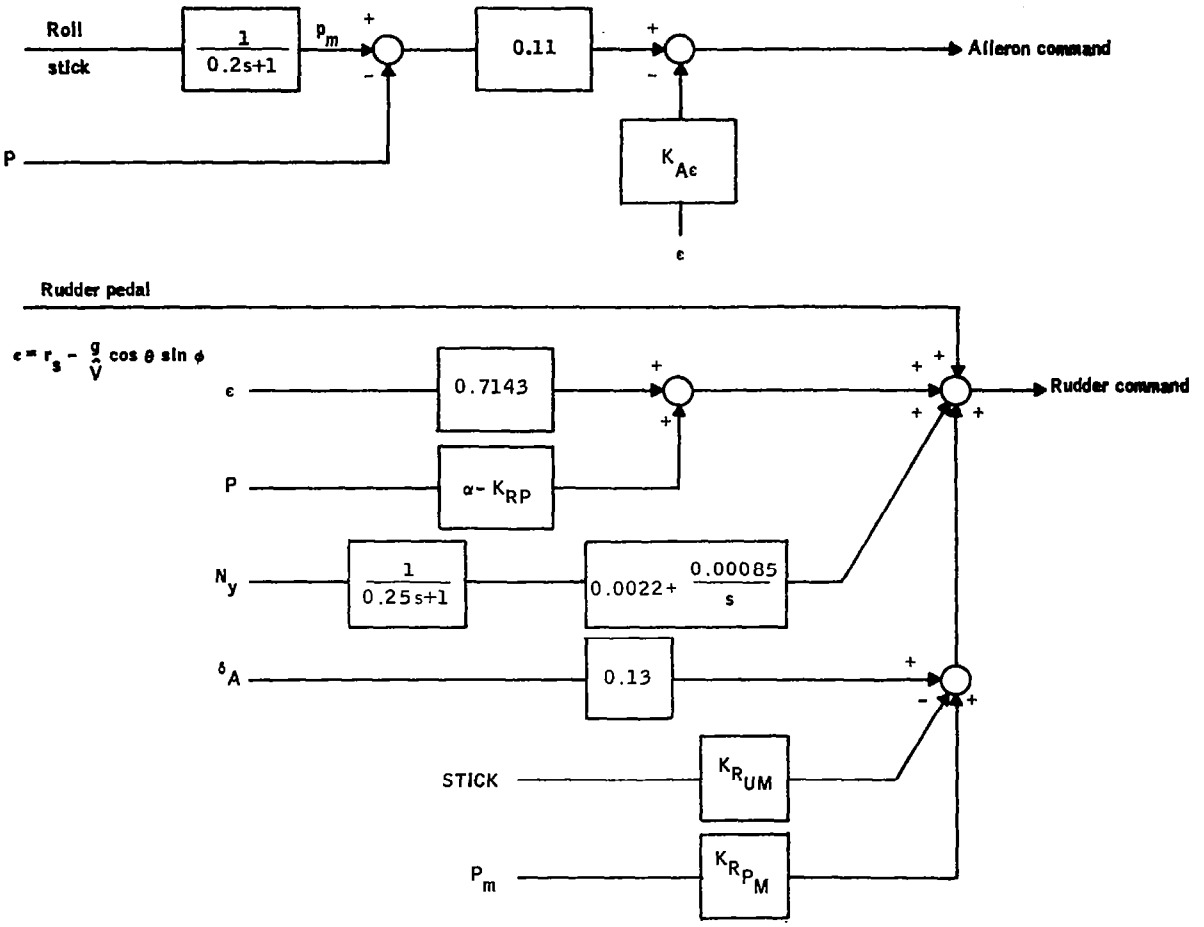

Figure 19. Lateral Control Law with Inertial Coordination

TABLE 3.- LATERAL GAIN SCHEDULES

Gain	Function	
$K_{A\epsilon}$	0.5α	<0.005
	$-7.29\alpha + 0.54$	$0.005 \leq \alpha < 0.15$
	$-2.0\alpha - 0.274$	$0.15 \leq \alpha \leq 0.275$
	-0.875	$0.275 \leq \alpha$
K_{RP}	0.0474	$\alpha < 0.01$
	$0.54\alpha + 0.042$	$0.01 \leq \alpha < 0.3$
	0.4	$0.3 \leq \alpha$
K_{RUM}	0.0096	$\alpha < 0.01$
	$0.16\alpha + 0.008$	$0.01 < \alpha < 0.3$
	0.05	$0.3 \leq \alpha$
K_{RPM}	0.0095	$\alpha < 0.03$
	$-0.1\alpha + 0.012$	$0.03 \leq \alpha \leq 0.12$
	0	$0.12 < \alpha$

Accuracy Requirements

The problem in implementing inertial coordination is the requirement for accurate estimates of angle-of-attack, true air speed, and aircraft attitude. These signals usually require external sensors and may cause reliability problems.

The required air speed accuracy, for example, can be determined by assuming that the controller gains are sufficiently high such that

$$\epsilon = r_s - \frac{g}{V}\cos\theta \sin\phi = 0$$

From Figure 19 the expression for side force then is

$$mVr_s = mg\cos\theta\sin\phi + Y$$

and lateral acceleration is

$$N_y = \frac{Y}{m} = Vr_s - g\cos\theta\sin\phi + \Delta Vr_s$$

$$= Vr_s - g\cos\theta\sin\phi + \Delta V\frac{g}{V}\cos\theta\sin\phi$$

$$N_y = g\cos\theta\sin\phi\left(-1 + \frac{\Delta V}{V}\right) + Vr_s$$

Hence, ΔN_y due to velocity errors is

$$\Delta N_y = g\cos\theta\sin\phi\,\frac{\Delta V}{V} \tag{45}$$

Now if we specify tolerable ΔN_y levels as 0.02 g's and let $\sin\phi \simeq 1$ and $\cos\theta \simeq 1$, we get

$$|\Delta V/V| \leq 0.02,$$

which indicates that ±2.0 percent accuracy is required for the air speed data source. This number is pessimistic, however, because all coordination was assumed to come from ε. In practice, some coordination is also obtained from direct N_y feedback and from control surface crossfeeds. These contributors reduce the required accuracy to approximately ±5 percent. Similar accuracy requirements can also be derived for the angle-of-attack and attitude signals.

Identifier Design

Signals with the above accuracy must usually be obtained from high-quality air data sensors and an all-attitude platform. The objective of the lateral identifier design task was to examine the potential of getting sufficiently good angle-of-attack and airspeed estimates on-line to remove the need for the air data sensors. As already noted in Section 3 the pitch-axis identifier alone falls well short of this goal primarily because the needed parameters are weakly identifiable in the baselined low signal pitch environment (ref. 1). It should be noted, however, that the inertial coordination requirements do not apply when signal levels are low. They are only important during significant lateral maneuvers, becoming progressively more severe as the maneuver magnitude increases. It is reasonable to expect that parameter values will be "more identifiable" during such large maneuver periods, and, hence, that the required accuracy can be achieved by designing a separate identifier for the lateral axis.

Design approach. - The lateral identifier was constructed in accordance with the MLE design procedure already developed for pitch (ref. 1). The first step of this procedure calls for model selection and parameterization. The next step is a theoretical identifiability study to verify that the desired goals can be achieved and to isolate significant parameters in the model's parameterization. This is followed by detailed identifier design, and, finally, by simulation verifications. Results of these steps for the lateral identifier are summarized below.

Lateral model and parameterization. - Inner loop lateral-directional dynamics are usually represented by a fourth-order linear model with roll rate, yaw rate, angle-of-sideslip, and roll angle as state variables

$$x = (p,\ r,\ \beta,\ \phi)^T$$

and with the following inputs and measured outputs:

$$u = (\delta_a,\ \delta_r)^T$$

$$y = (p_m,\ r_m,\ N_{ym},\ \phi_m)^T$$

For purposes of identifier design in large maneuvers, this model was simplified to first-order by treating p, r, and ϕ as known inputs with β as the only state variable. The resulting model is

$$\begin{aligned} \frac{d}{dt}\beta &= Y_\beta \beta + \left[-1 \;\; \alpha \;\; \frac{1}{V} Y_{\delta_r} \;\; Y_{\delta_a}\right] u_m + \sqrt{\frac{2V}{L_v}}\, \sigma_{vg}\, \xi \\ y = N_{y_m} &= (Y_\beta V)\beta + \left[0 \;\; 0 \;\; 0 \;\; \left(Y_{\delta_r} V\right) \;\; \left(Y_{\delta_a} V\right)\right] u_m + \eta \end{aligned} \tag{46}$$

with u_m defined by

$$u_m = (r_m,\ p_m,\ g\cos\theta_m \sin\phi_m,\ \delta_{r_m},\ \delta_{a_m})^T$$

The unknown coefficients of this model are α, $1/V$, $(Y_\beta V)$, $(Y_{\delta r} V)$, and $(Y_{\delta_a} V)$. These were parameterized in terms of known estimates from the pitch axis identifier plus six new unknown small perturbations (C_L). The parameterization is shown in Table 4.

Theoretical identifiability. - As the next step of the design process, an evaluation was made of the theoretical accuracy to which the six new parameters [plus gust level, σ_{vg}, and initial condition, $\beta(o)$] can be identified during large lateral maneuvers. The methodology for these evaluations is described in (ref. 1) and reviewed in an earlier section. Results are summarized in Figures 20 through 25.

TABLE 4.- LATERAL MODEL PARAMETERIZATION

Original coefficient*	New parameter	New parameter a priori uncertainty**
$\alpha = \hat{\alpha}_p + C_{L1}$	C_{L1}	$0.3\,\hat{\alpha}_p$
$1/V = 1/\hat{V}_p + C_{L2}$	C_{L2}	$0.2/\hat{V}_p$
$(Y_\beta V) = (12 + C_{L4})\,[(\hat{M}_{\delta o})_p + C_{L3}]$	C_{L3}	$0.2\,(\hat{M}_{\delta o})_p$
	C_{L4}	1.3
$(Y_{\delta r} V) = -(2.5 - 1.6\,\hat{C}_{2p} + C_{L5})\,[(\hat{M}_{\delta o})_p + C_{L3}]$	C_{L5}	0.35
$(Y_{\delta_a} V) = -(0.22 + C_{L6})\,[(\hat{M}_{\delta o})_p + C_{L3}]$	C_{L6}	0.062

*$(\hat{M}_{\delta o})_p$, $\hat{\alpha}_p$, and $\hat{V}_p$ are estimates from the pitch axis identifier.

**A priori uncertainties are taken from pitch axis identifier performance and from Table 13 (ref. 1).

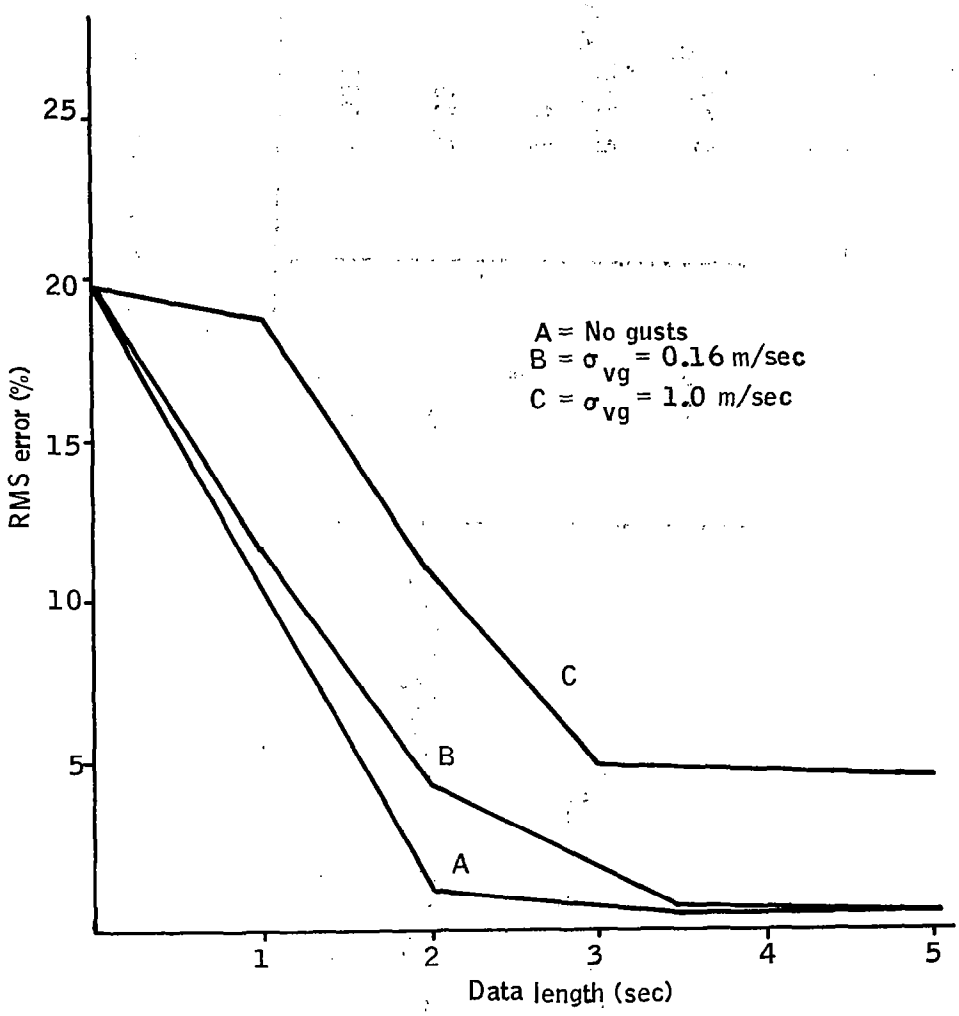

Figure 20. Theoretical Identification Accuracy Parameter: $\frac{1}{V}$, Large Maneuver

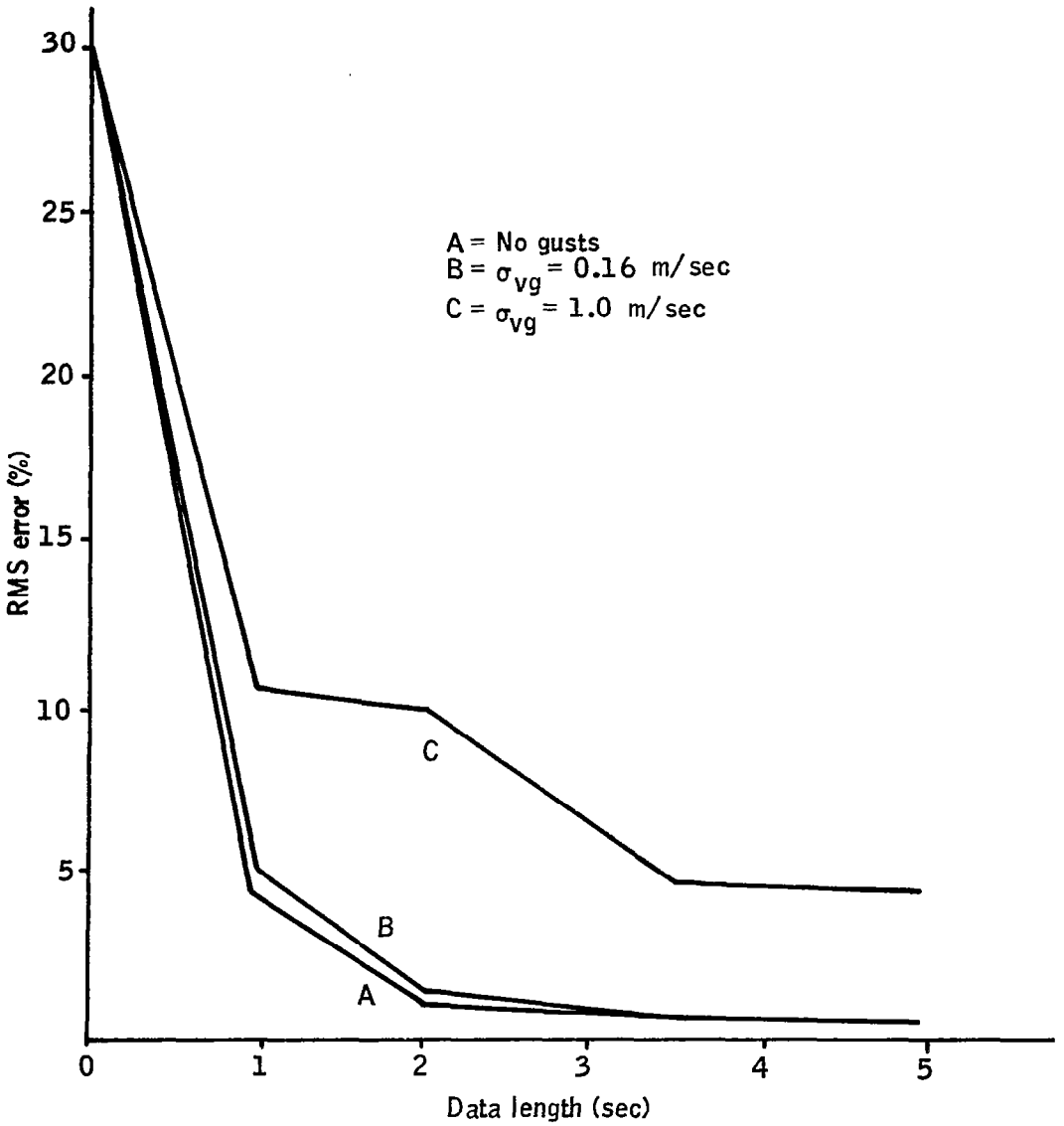

Figure 21. Theoretical Identification Accuracy Parameter: α, Large Maneuver

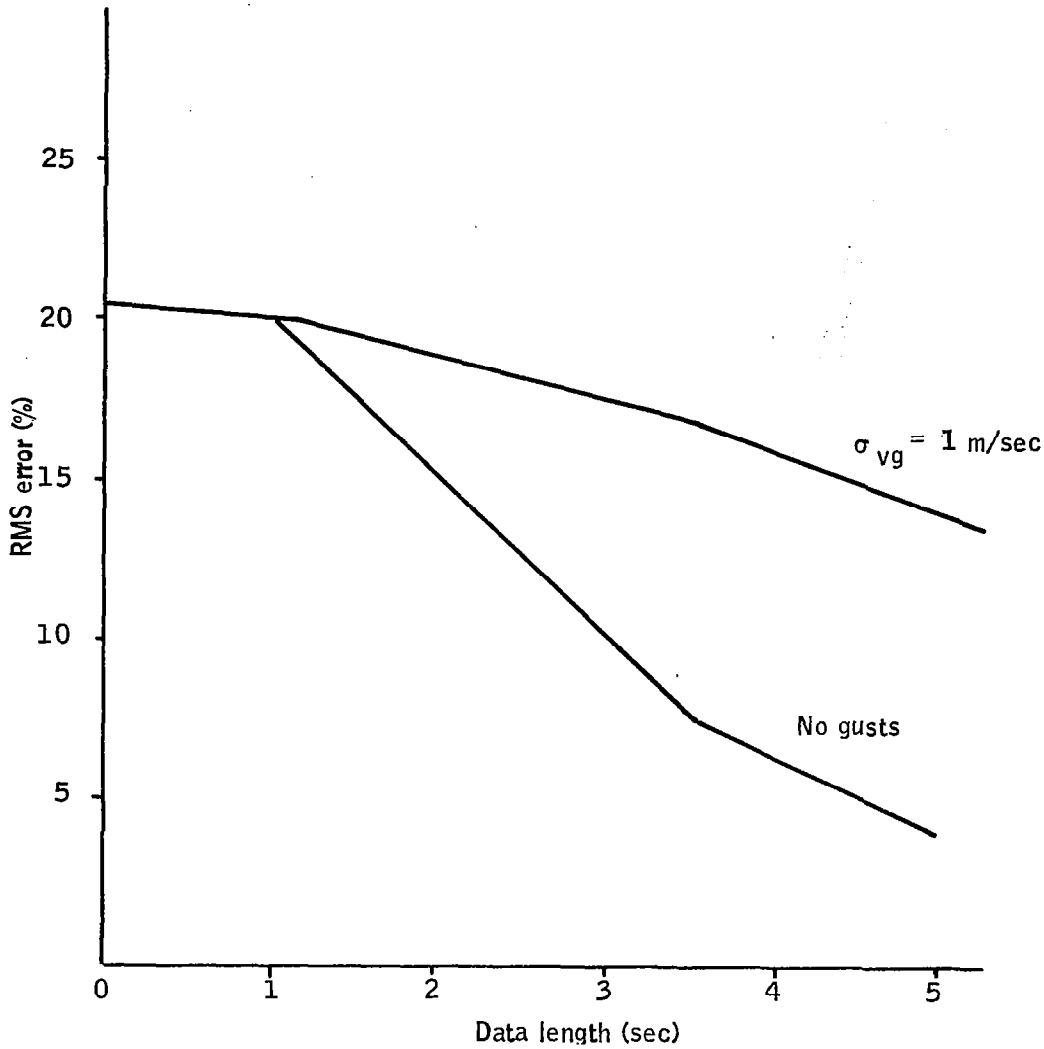

Figure 22. Theoretical Identification Accuracy Parameter: $\frac{1}{V}$, Small Maneuver

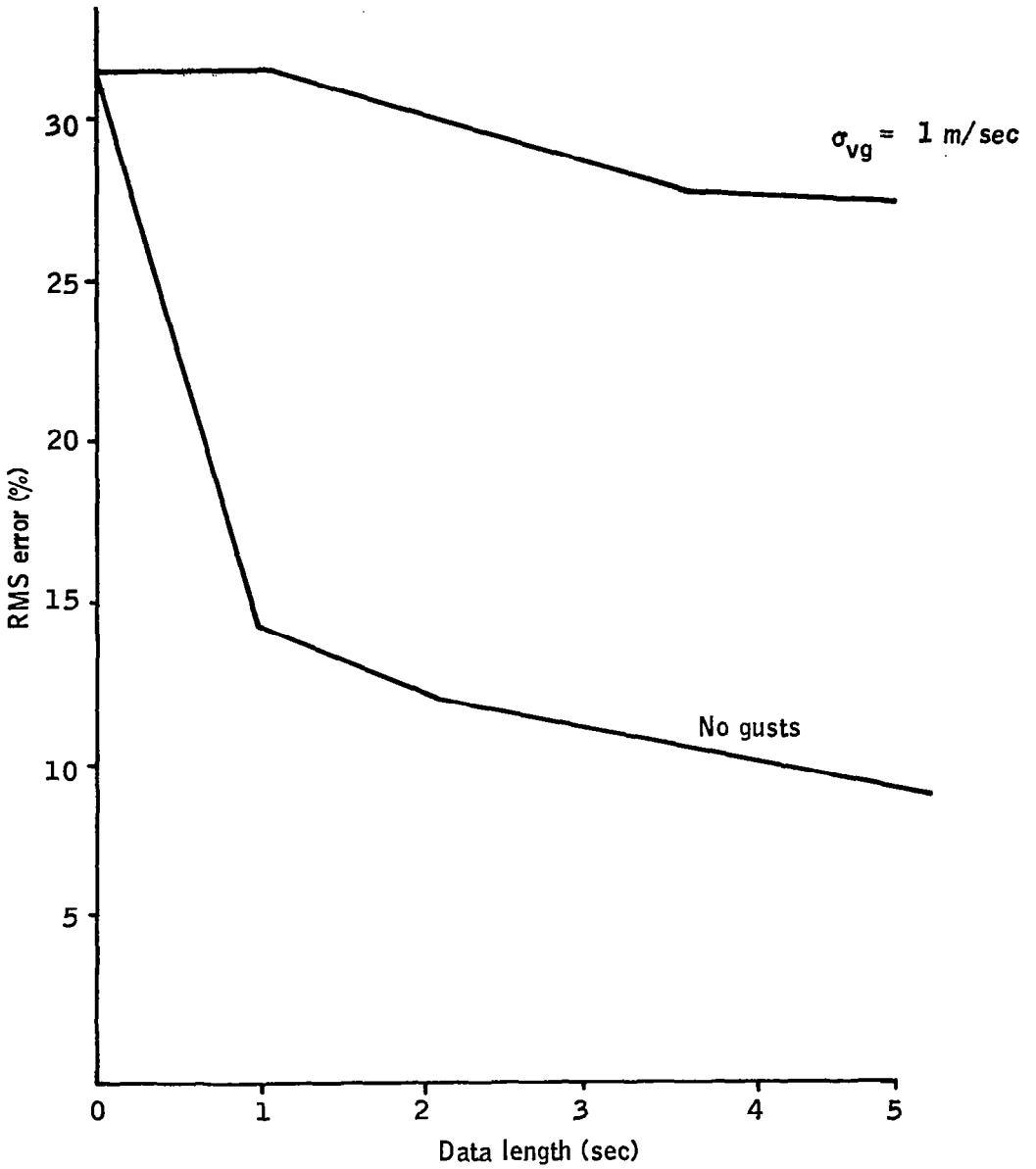

Figure 23. Theoretical Identification Accuracy Parameter: α, Small Maneuver

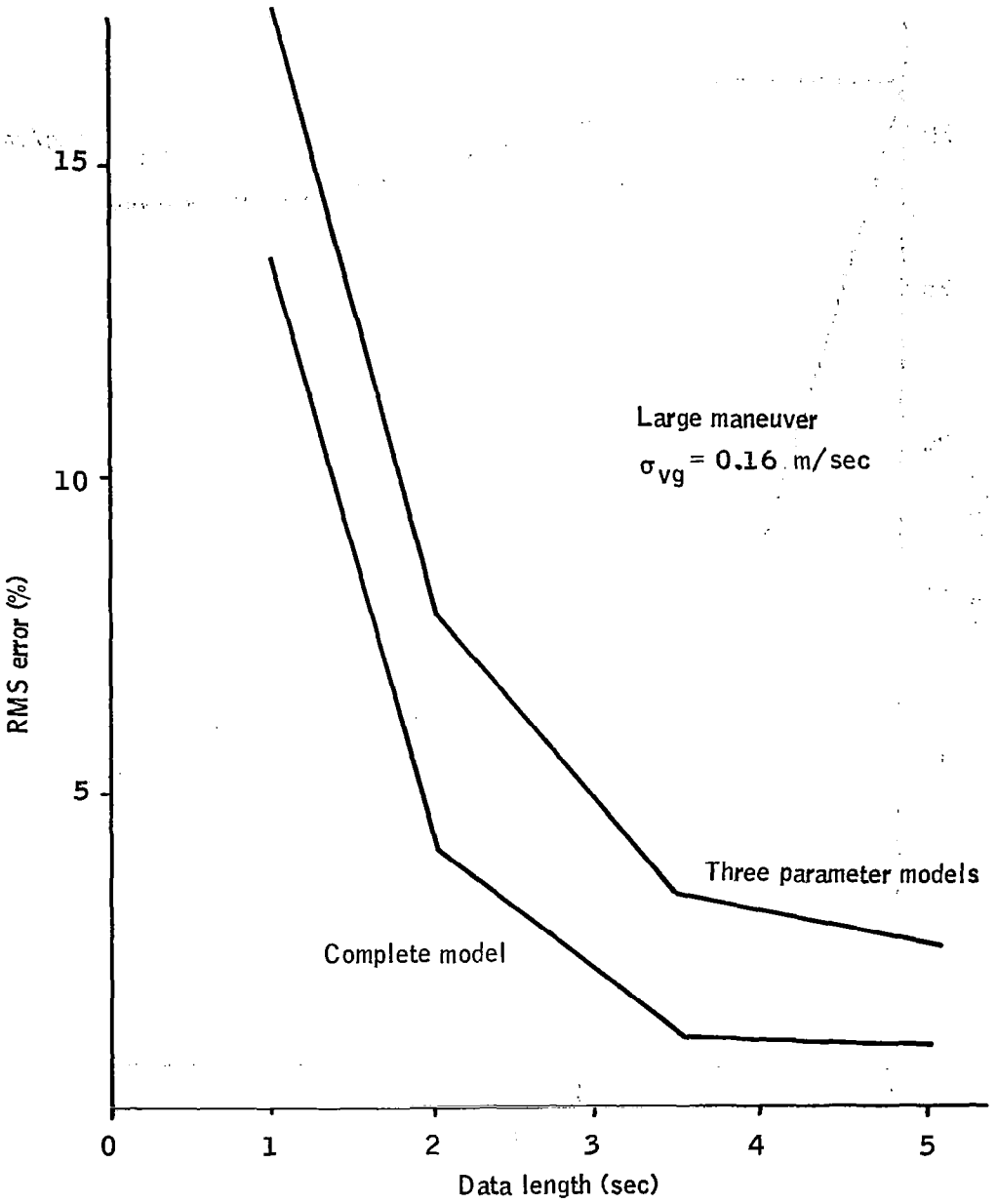

Figure 24. Theoretical Identification Accuracy with Reduced Parameter Models
Parameter: $\frac{1}{V}$

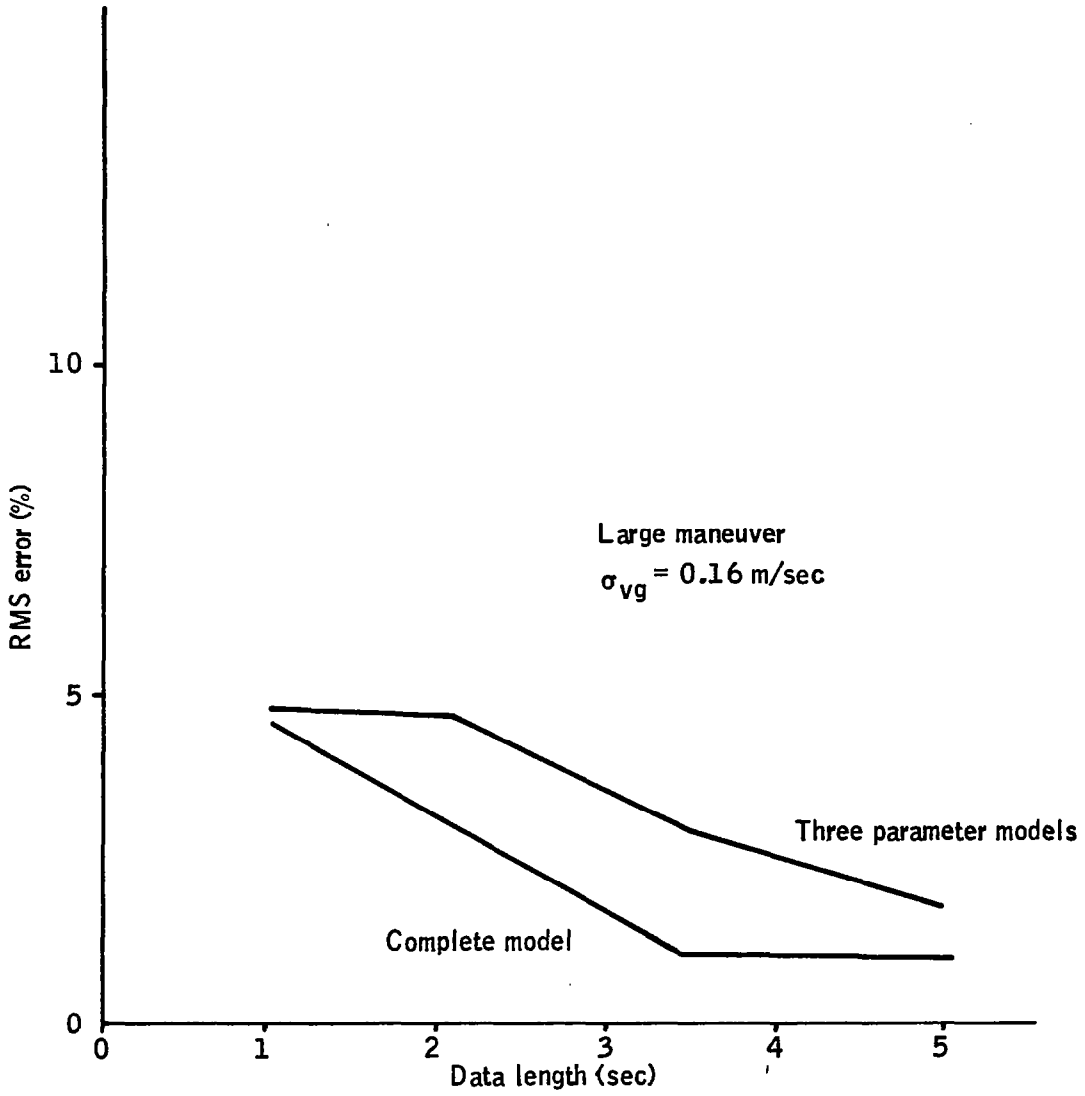

Figure 25. Theoretical Identification Accuracy with Reduced Parameter Models
Parameter: α

Figures 21 and 22 show theoretical identification errors for 1/V (C_{L2}) and α (C_{L1}), respectively, as a function of data length for a large rolling maneuver and three gust intensities. The RMS sensor noises (for a 100-radian bandwidth) were:

- Rate gyro (yaw, roll) 0.15 deg/sec
- Bank angle 0.25 deg
- Surface positions (δ_a, δ_r) 0.04 deg
- Lateral accelerometer 0.003 g

The maneuver consisted of a square wave sequence of ±50 deg/sec roll rate commands with a period of four seconds. The curves verify that the required inertial coordination accuracy is at least theoretically achievable within one to two seconds after the maneuver is initiated.

Figures 23 and 24 show similar results for a much smaller maneuver, ±5 deg/sec. As expected, accuracy for this case is poorer. However, it still meets the relaxed requirements of inertial coordination at small roll angles.

Figures 25 and 26 show accuracy predictions for the large maneuver case when only three of the six parameters in C_L [plus $\beta(o)$] are recognized by the identifier. This is commonly called "reduced parameter identification." It achieves poorer performance than the full parameter case because errors in the unrecognized parameters contribute to incorrect identification. As seen from the figures, however, these contributions are small enough to justify the reduced parameter approach.

Detailed design. - Based on the above identifiability findings, a three-parameter MLE identifier was developed to estimate C_{L1}, C_{L2}, and C_{L3}. As shown in Table 4, these correspond to small deviations from pitch-axis estimates of α, 1/V, and $M_{\delta o}$, respectively. A block diagram of the identifier is shown in Figure 26. It uses a single parallel Kalman filter channel

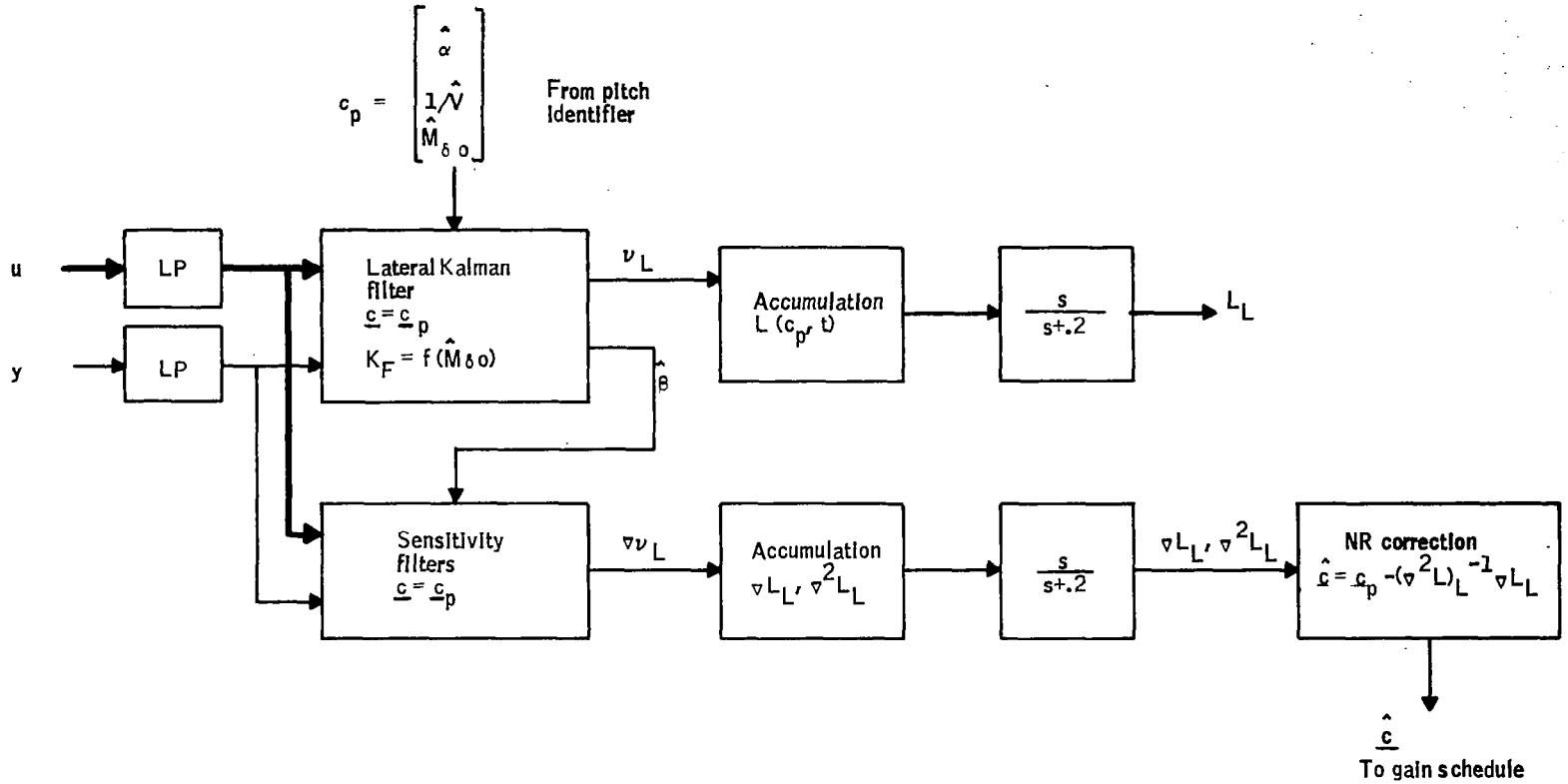

Figure 26. Lateral Identifier Block Diagram

which is not fixed in parameter space, as the pitch-axis channels are, but rather moves around to follow the pitch estimates. The usual single Newton-Raphson correction is taken from its current location to reach the final estimate. Models for the Kalman filter and sensitivity filters of the identifier were developed by discretizing equation (46) to first order terms and rearranging the input vector, u_m, for greater computational efficiency. Details are provided in the flow diagram of Appendix A.

Simulation verification. - Because of the transient nature of lateral identification (i. e., good accuracy achieved only during large maneuvers) the lateral identifier was not evaluated in an open-loop fashion with emphasis on identification errors. Instead, it was evaluated closed loop -- lateral estimates ($\hat{\alpha}$, 1/V) used to schedule the inertially coordinated CAS of Figure 18, Table 3 -- with emphasis placed on the damping and turn coordination achieved by the overall adaptive system. Investigations were carried out on NASA Langley's F-8C simulator at FC1, FC5, FC8, and FC10. As defined earlier, these flight conditions correspond to a middle-of-the-envelope condition, a low-$\bar{q}$ condition, a supersonic condition, and a high-dynamic-pressure condition. Time histories from the simulator are given in Figures 27 through 34. The adaptive system's performance (labeled "MLE") is compared in these figures with two other lateral-directional controllers. One is the lateral CAS from the baseline adaptive program (ref. 1). This is labeled "RM," for reduced measurement. The second is the same inertially coordinated CAS of Figure 18, Table 3, but scheduled with perfect values of angle-of-attack and velocity. It is labeled "IC."

Comparisons of these three systems are shown for rolling maneuvers and followed in the succeeding illustration with step β gust responses. The first displays turn coordination quality in terms of the N_y and β magnitudes developed during a turn. The second displays dutch roll damping. It is apparent from these comparisons that the adaptive system (MLE) matches the damping characteristics of the perfectly scheduled one (IC) quite closely. Both are significantly better than the baseline system (RM).

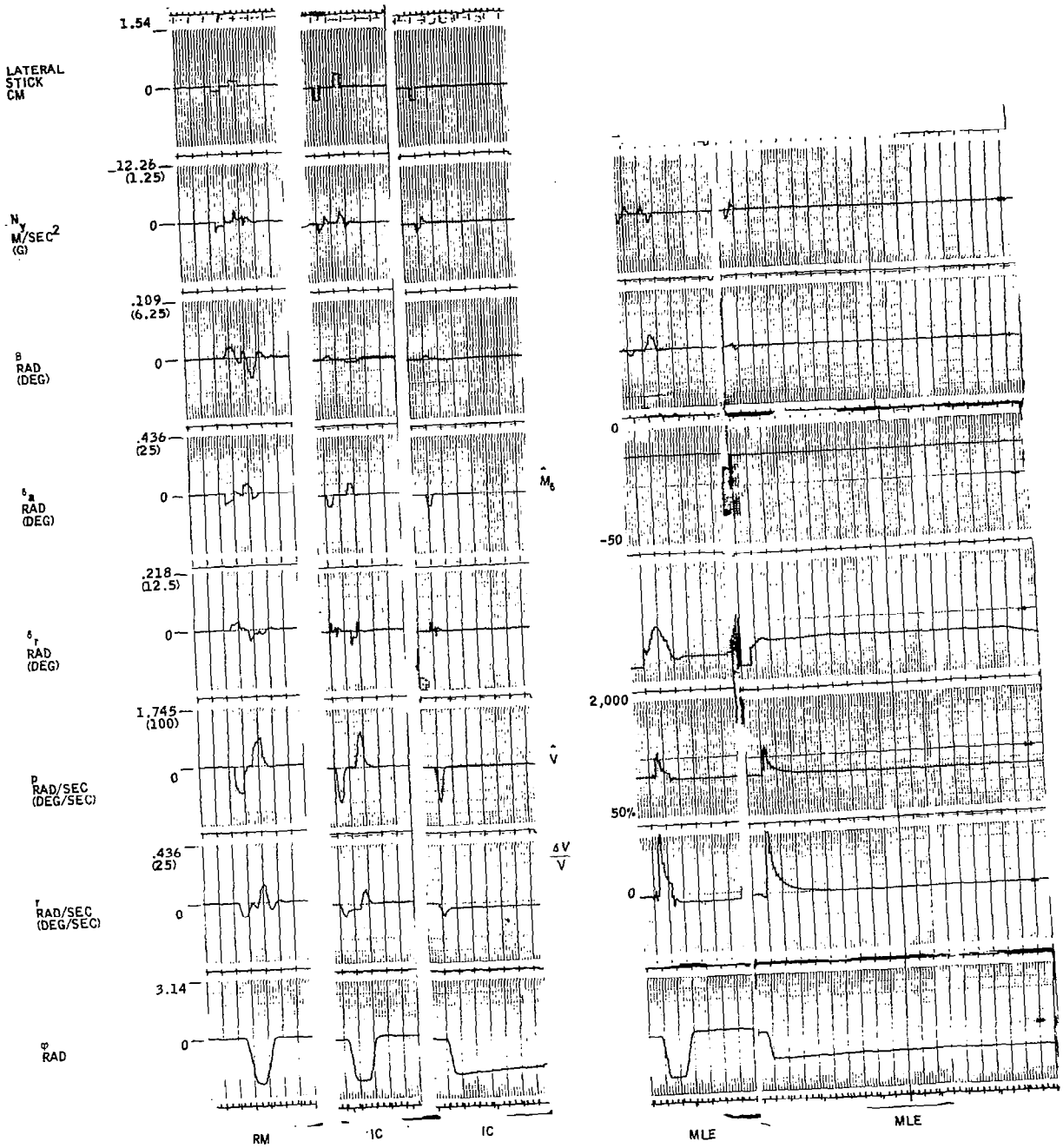

Figure 27. Rolling Maneuvers FC1

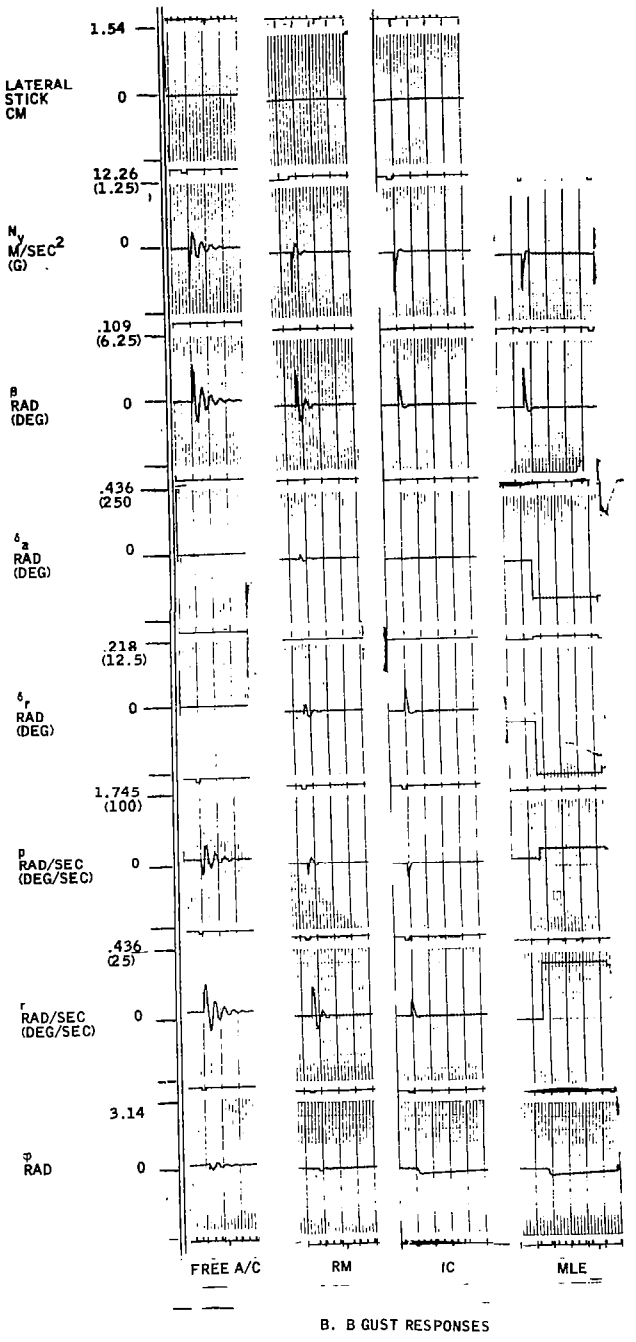

Figure 28. Step B Gust Responses, FC1

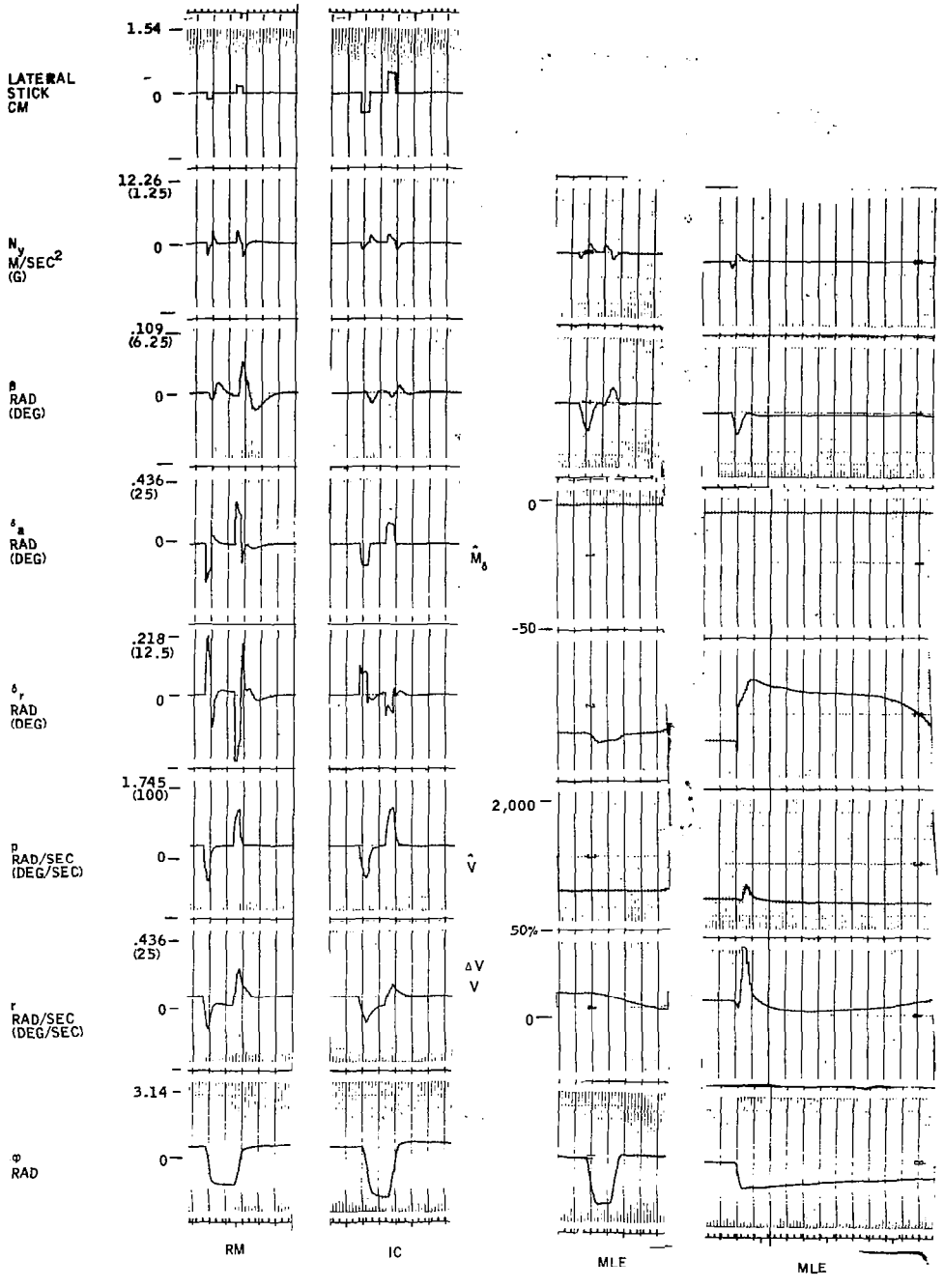

Figure 29. Rolling Maneuvers, FC5

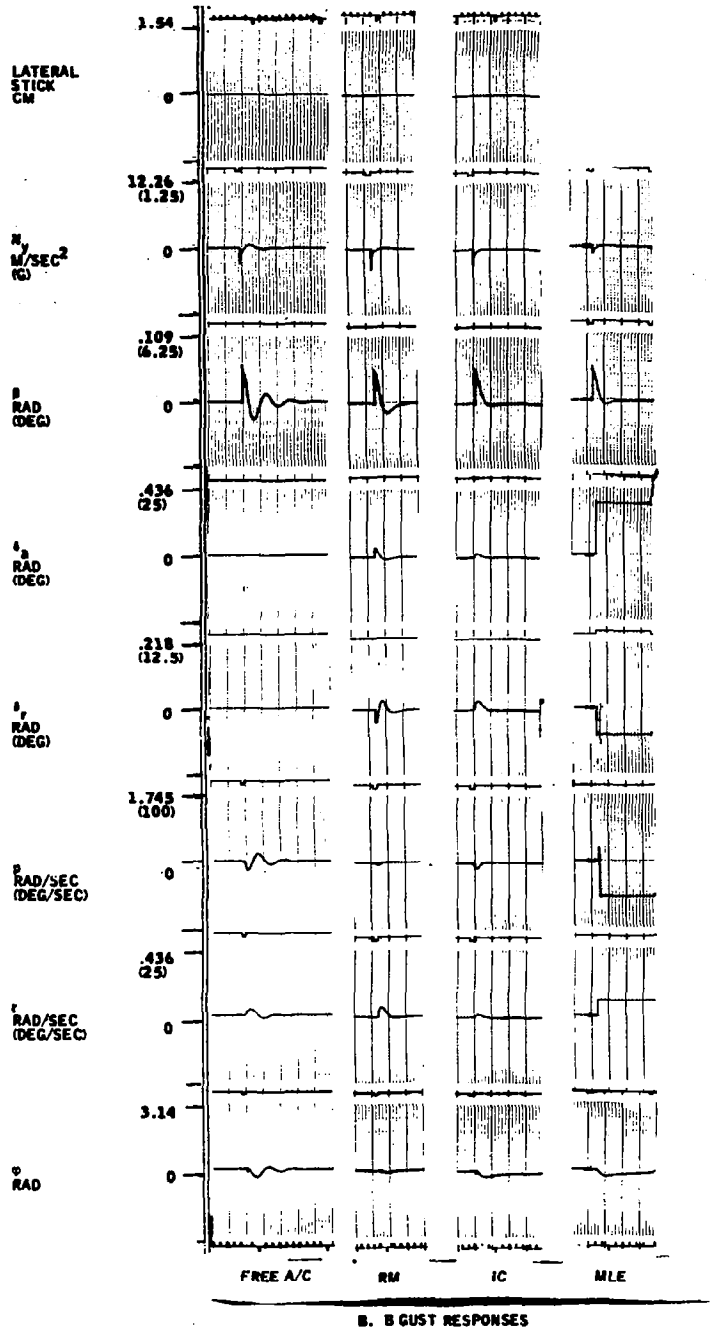

Figure 30. Step B Gust Responses, FC5

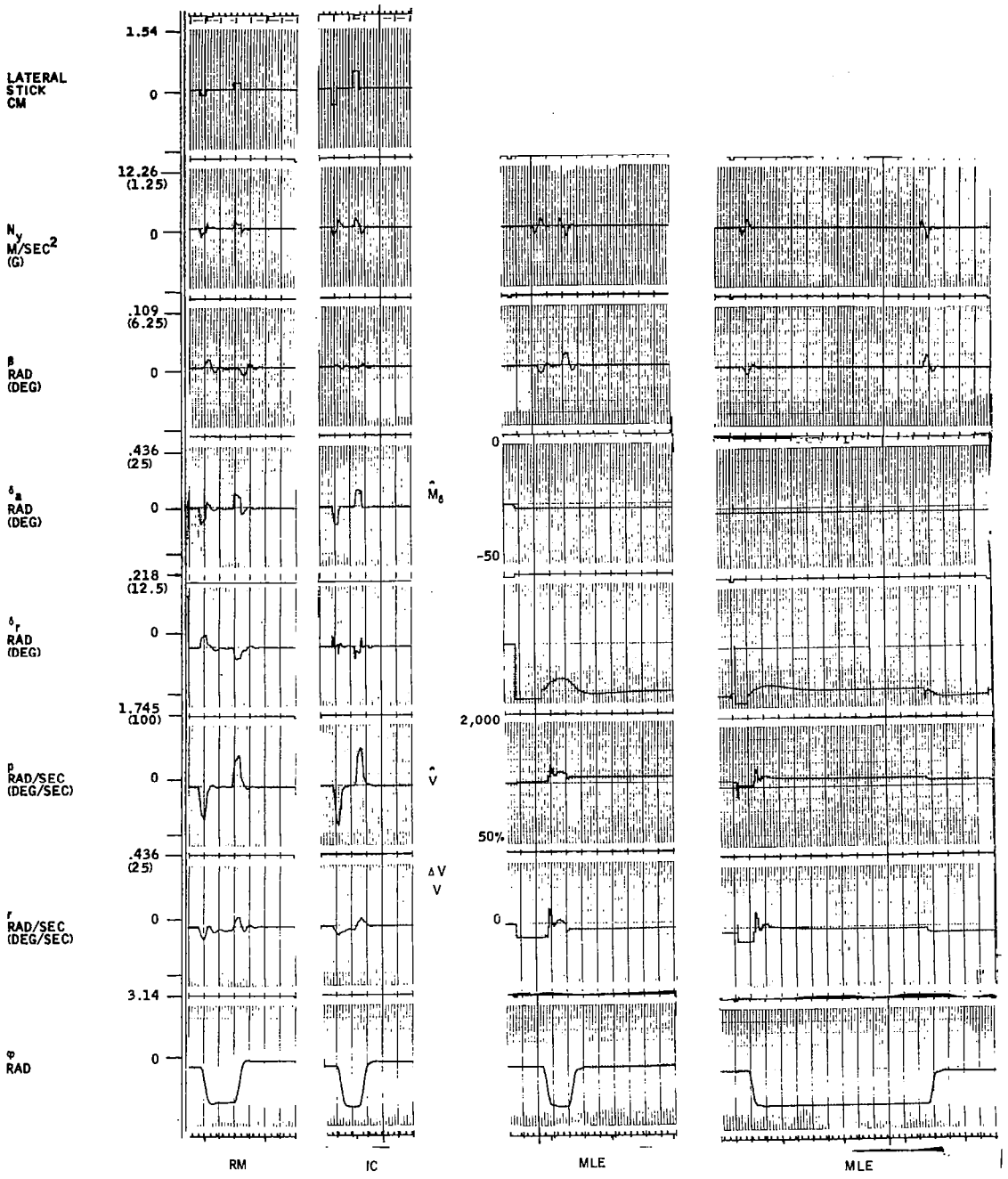

A. ROLL COMMAND RESPONSES

Figure 31. Rolling Maneuvers, FC8

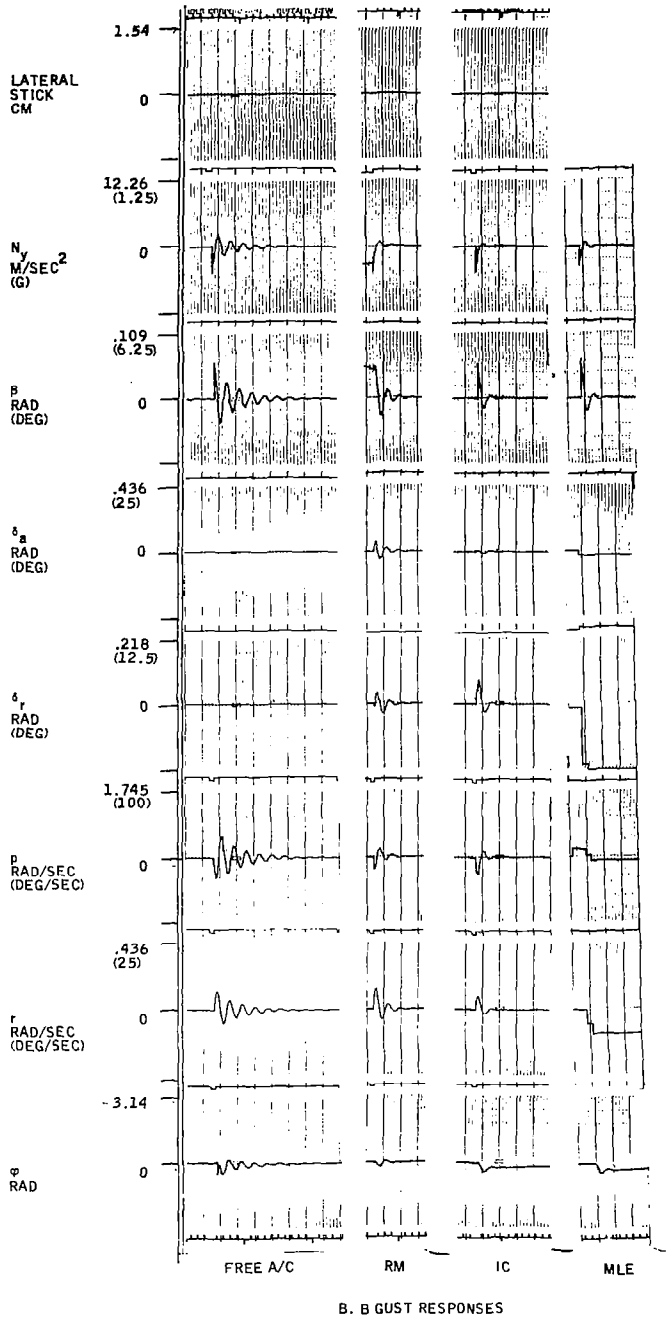

B. B GUST RESPONSES

Figure 32. Step B Gust Responses, FC8

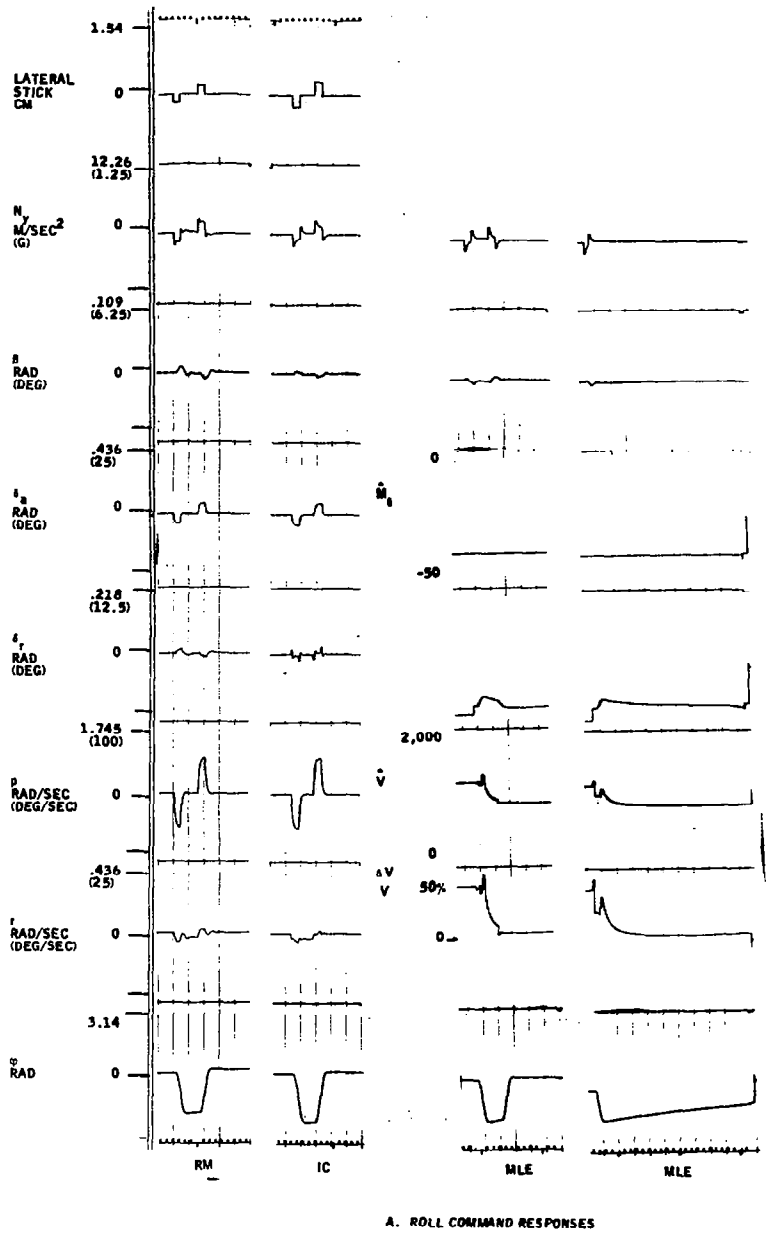

A. ROLL COMMAND RESPONSES

Figure 33. Rolling Manuevers, FC10

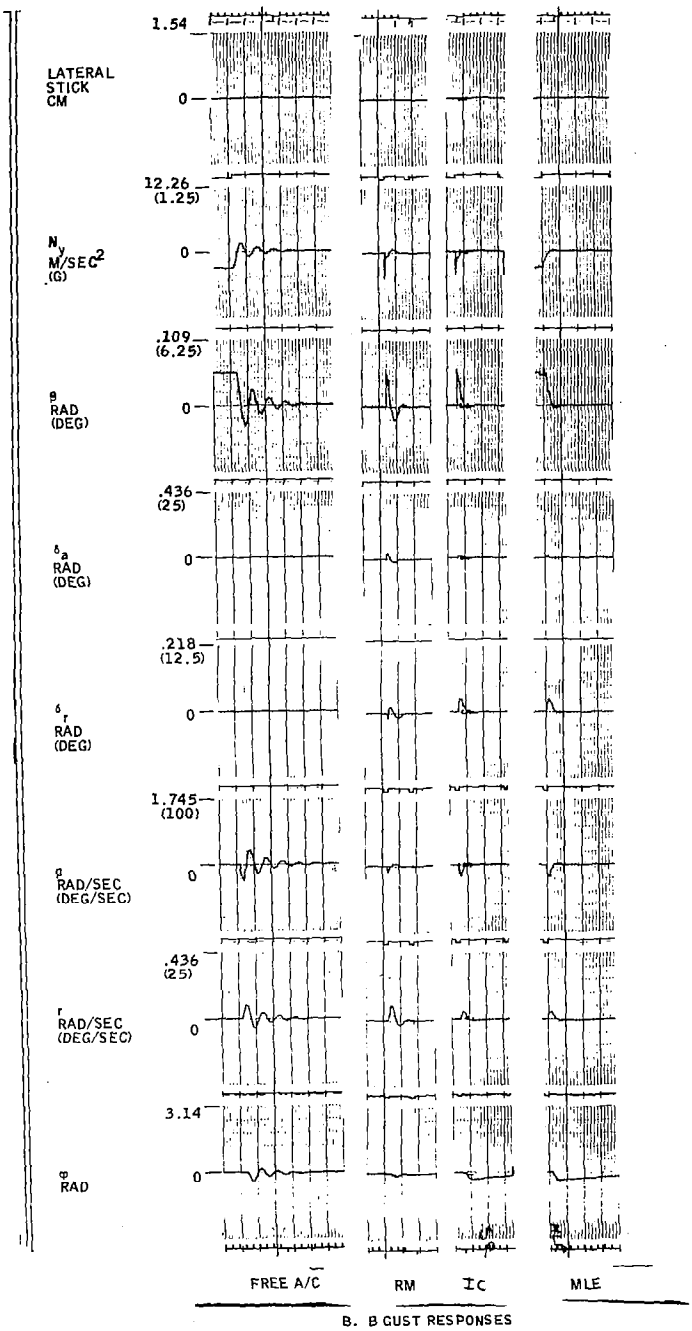

Figure 34. Step B Gust Responses, FC10

The turn coordination comparisons show a close match of the N_y traces for the MLE and IC systems but larger β excursions for MLE. These excursions are no larger, however, than those of the RM system. Since the latter meets all turn coordination requirements for the F-8C (ref. 6), the MLE system is also satisfactory.

Although the above comparisons are limited in scope, they suggest that good turn coordination and dutch roll damping without conflict can indeed be achieved with on-line identification and no air data. The technique is worthy of further investigation and eventual flight test. Topics of particular interest for further study include direct estimation of the error quantity, ϵ, instead of its scheduling components α and $1/V$, and replacement of the Newton-Raphson step in Figure 27 with Kalman filter corrections as described in Section 3.

SECTION 5
ANALYTICAL REDUNDANCY

The objective of this task was to examine analytical redundancy within the context of the existing structure and computations of the baseline MLE identification algorithm. This task was motivated by the recognition that most analytical redundancy approaches use Kalman filters of the type already available within the identifier to perform failure detection and isolation functions. Three candidate concepts were developed and tested on NASA's F-8C simulator. Simulation results indicate the feasibility of these preliminary designs. Objective performance standards for analytical redundancy were then derived from flight safety and mission reliability requirements. Further evaluations of the concepts are recommended to demonstrate that these performance standards can be achieved.

Review of Analytical Redundancy Procedures

Analytical redundancy is based on exploiting known dynamic and kinematic relationships to estimate sensor outputs. These estimates are useful in detecting sensor failures. In this section published procedures are reviewed to identify suitable techniques for the F-8C application.

A number of failure detection approaches were suggested by R. K. Mehra and J. I. Peschon (ref. 8) based on the theoretical properties of Kalman filter residuals. Tests that apply to Kalman filter residuals include:

- Tests of whiteness - The residuals should be independent at different time instants.
- Tests of mean - Sample means should be zero.
- Tests of covariance - Covariance of residuals should equal apriori values.

Another alternative related to the test of whiteness is the test of orthogonality: The residuals and the estimated measurements should be uncorrelated.

The notion of using Kalman filters as the failure detection device was applied by Meier, et. al. (ref. 9) and later by Maybeck (ref. 10) to the F-4 sensor complement. Each Kalman filter processed several sensors. In addition, isolation of the failure was usually accomplished by noting a large filter residual for that sensor and failure indications from other Kalman filters.

Kerr (ref. 11) reported a different approach based on suboptimal Kalman filters. The state was augmented with failure states (whose zero implies no failure) and a test was designed to detect departures from the "no failure" trajectory. Isolation of the failure was accomplished by combining groups of tests, each with an appropriate set of failure states. This test is intended for filters that are known to be suboptimal (i. e., reduced order) and hence do not produce residuals with known theoretical properties.

Montgomery et. al. (ref. 12) have used multiple hypothesis tests to detect and isolate failures. A bank of Kalman filters generate sensor residuals under a set of different hypothesis. These residuals are accumulated as likelihood functions with the minimum function indicating the current most likely hypothesis.

Other researchers such as Willsky (ref. 13) have developed generalized likelihood ratio methods to reduce the complexity of hypothesis tests. Those techniques use one Kalman filter. Its residuals are correlated against stored sets of residual responses, one for each hypothesis. The highest correlation then indicates the most likely hypothesis.

At this point it is apparent that a common element in many of these fault detection procedures is the Kalman filter. This element is also a key part of

the F-8C MLE adaptive algorithm. Therefore, it seems reasonable to build analytical redundancy concepts around the Kalman filters that already exist in the adaptive system. Those concepts model the short-period motion of the pitch axis and use a rate gyro and an accelerometer as input sensors. In the next section three specific redundancy concepts are developed to detect failure of these sensors. Each concept is based on monitoring filter residuals or likelihood functions to detect sensor failures. Isolation is accomplished by including hardware comparison of like sensors or other analytical tests.

Specific designs for the F-8C. - Two designs had the objective of detecting and isolating a failure in a dual channel sensor set. The third design was aimed at detecting a sensor fault in a single sensor complement but was not required to isolate the failure.

The first two designs use the existing set of pitch axis Kalman filters augmented with one extra channel to process measurements from redundant sensors. Both designs are based on comparing likelihood functions from the minimum-L channel with the redundant channel. The model and filter gains in the redundant channel are slaved to the minimum-L channel determined by the adaptive algorithm. The only difference between these two channels is the set of measurements they process. The structure is shown in Figure 35. Large deviations in the two likelihood functions indicate that one set of measurements is inconsistent (i.e., a sensor failure). Since likelihood functions are used for comparison, the larger one will be the result of the failed sensor.

The third design processes the filter residual of a single channel only.

Design details for the three concepts are discussed in the remainder of this section.

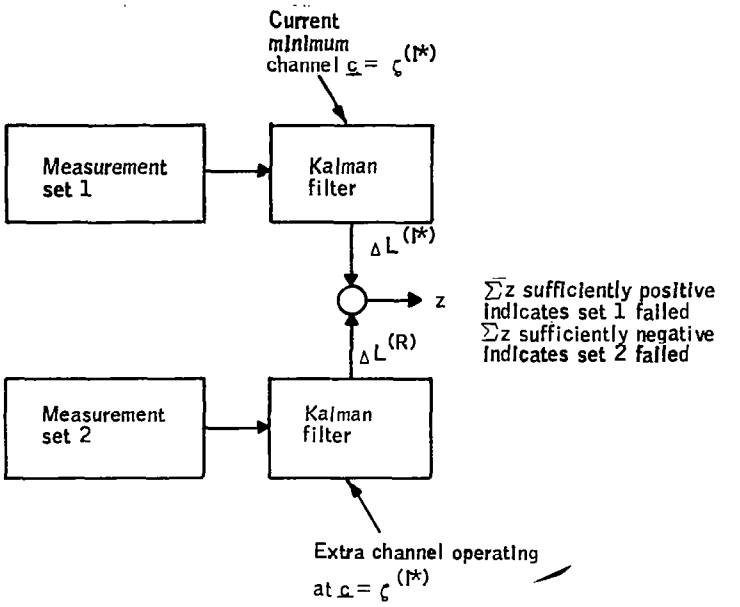

Figure 35. Analytical Failure Detection - Designs 1 and 2

Design 1: The objective of this design is to detect and isolate sensor failures in two redundant sensor sets. The detection is performed by comparison monitoring of like sensors, and isolation is accomplished with an analytical test of the difference of likelihood functions as shown in Figure 35.

The isolation logic can be described in the form of a truth table, (Table 5). Let $I_g = 1$ indicate a miscomparison of the two gyros, $I_a = 1$, a miscomparison of the two accelerometers, and $I_{ar} = 1$, an analytic failure indication for sensor set 1. Then simple combinations of these error flags will detect and isolate failures in each of the four sensors since the error flag pattern is unique for each hypothesis.

TABLE 5. - FAULT ISOLATION LOGIC

Sensor failed	Error flag		
	I_g	I_a	I_{ar}
None	0	0	0
Gyro 1	1	0	1
Accelerometer 1	0	1	1
Gyro 2	1	0	0
Accelerometer 2	0	1	0

The analytical failure flag, I_{ar}, was mechanized by testing the statistic

$$z_k = \Delta L_k^{(i^*)} - \Delta L_k^{(R)} = (L_k^{(i^*)} - L_{k-1}^{(i^*)}) - (L_k^{(R)} - L_{k-1}^{(R)}) \quad (47)$$

for presence of biases. This statistic was selected because it is sensitive to sensor failures but not sensitive to errors introduced by anticipated deviations between true aircraft parameters, $\underline{c} = \underline{c}_t$, and Kalman filter parameters, $\underline{c} = \zeta^{(i^*)}$. To see this, recall that the residual for the (i*)-th Kalman filter (with sensor set 1) is

$$\nu_k^{(i^*)} = y_k(\underline{c}_t) - \hat{y}_k(\zeta^{(i^*)}), \qquad k = 0, 1, 2 \ldots$$

It can be expanded in a power series about the true parameter $\underline{c}_t$ as follows:

$$\nu_k^{(i^*)} = y_k(\underline{c}_t) - \hat{y}_k^{(i^*)}(\underline{c}_t) - \nabla\hat{y}_k^{(i^*)}(\zeta^{(i^*)} - \underline{c}_t) + \text{h. o. t.} \quad (48)$$

$$= \xi_k^{(i^*)} - \nabla\hat{y}_k^{(i^*)}(\zeta^{(i^*)} - \underline{c}_t) + \text{h. o. t.}$$

Here, $\xi^{(i*)}$ is the theoretical zero-mean white residual sequence, $\hat{y}^{(i*)}$ is the optimal estimate, and $\nabla\hat{y}^{(i*)}$ is the gradient of the optimal estimate with respect to ζ. The analogous expression for the redundant sensor set 2 is

$$\nu_k^{(R)} = \xi_k^{(R)} - \nabla\hat{y}_k^{(R)} (\zeta^{(i*)} - \underline{c}_t) + \text{h.o.t.} \tag{49}$$

Note that $\xi^{(R)}$ is again a zero-mean white noise sequence which is correlated, in general, with the sequence $\xi^{(i*)}$.

Equations (48) and (49) substituted into equation (47) provide the following power series expression for the test statistic z_k:

$$\begin{aligned} z_k = \frac{1}{2}\{ & (\xi_k^T B^{-1} \xi_k)^{(i*)} - (\xi_k^T B^{-1} \xi_k)^{(i*)} - [(\xi_k^T B^{-1} \nabla\hat{y}_k)^{(i*)} \\ & - (\xi_k^T B^{-1} \nabla\hat{y}_k)^{(R)}] (\zeta^{(i*)} - \underline{c}_t) \\ & - (\zeta^{(i*)} - \underline{c}_t)^T [(\nabla\hat{y}_k^T B^{-1} \xi_k)^{(i*)} - (\nabla\hat{y}_k^T B^{-1} \xi_k)^{(R)}] \\ & + \|\zeta^{(i*)} - \underline{c}_t\|^2 [(\nabla\hat{y}_k^T B^{-1} \nabla\hat{y}_k)^{(i*)} - (\nabla\hat{y}_k^T B^{-1} \nabla\hat{y}_k)^{(R)}] + \text{h.o.t} \} \end{aligned} \tag{50}$$

Under normal no-failure conditions, the usual theoretical properties of Kalman filters apply to this expression. In particular,

$$E[\xi_k^{(i*)}] = 0, \qquad E[(\xi_k^T B^{-1} \nabla\hat{y}_k)^{(i*)}] = 0,$$

$$E[\xi_k^{(R)}] = 0, \qquad E[(\xi_k^T B^{-1} \nabla\hat{y}_k)^{(R)}] = 0.$$

Furthermore, if we assume that the two sensor sets have identical noise statistics, then $\xi^{(i*)}$ and $\xi^{(R)}$ are identically distributed sequences, as are $\nabla\hat{y}^{(i*)}$ and $\nabla\hat{y}^{(R)}$. It then follows that E(z) = 0 regardless of the parameter error (at least up to 2nd order terms).

In the event of sensor failure, of course, one of the likelihood functions $L^{(i*)}$ or $L^{(R)}$ will increase beyond its normal no-failed value. The test statistic, z, will then develop biases (positive for sensor set 1 failure and negative for sensor set 2) which can be detected by statistical decision procedures.

The decision procedure selected for Design 1 was the so-called sequential likelihood ratio test (ref. '14). It is based on the following function

$$\Lambda_{ik} = \frac{f_0 (z_i \cdots z_k)}{f_1 (z_i \cdots z_k)}$$

where Λ_{ik} is a likelihood ratio, i is the starting sample, k is the current sample (at time t_k), f_0 is the distribution of the test statistics under hypothesis H_0 (no failure) and f_1 is the distribution under hypothesis H_1 (sensor failure).

The test is:

Accept H_1 if $\Lambda_{ik} \leq A$

Accept H_0 if $\Lambda_{ik} \geq B$

Continue test if $A < \Lambda_{ik} < B$

If the test statistic, z, has a normal distribution † and the two hypothesis correspond to different mean values, the test reduces to comparing the sum

† This is not quite true for the statistic in equation (50), but convenience outweighs rigor.

$$\sum_{\ell=i}^{k} z_\ell$$

against the following thresholds:

$$\frac{(k-i)(\mu_0 + \mu_1)}{2} - \frac{\sigma^2}{(\mu_1 - \mu_0)} \ell nB < \sum z_\ell < \frac{(k-i)(\mu_0 + \mu_1)}{2} - \frac{\sigma^2}{(\mu_1 - \mu_0)} \ell nA$$

where μ_0 and μ_1 are the means corresponding to hypotheses H_0 and H_1 respectively, and σ^2 is the variance of the test statistic.

Parameters for these thresholds were set at

$$\mu_0 = 0$$

$$A = 1/B = 10^{-3}$$

$$\mu_1 = \begin{cases} 3.9\ \sigma \text{ for Sensor Set 1 Failures} \\ -3.9\ \sigma \text{ for Sensor Set 2 Failures} \end{cases}$$

Estimates of σ for no-failure conditions were obtained from the F-8C simulation under a variety of commands and gust disturbances. The test was initiated whenever either of the two simulated gyros or accelerometers triggered the hardware comparators, I_g or I_a. Thresholds for the latter comparators are discussed later in this section. A pictorial summary of Design 1 is shown in Figure 36.

Design 2: This design had the same objectives as Design 1. However, instead of initiating the analytical test upon miscomparisons of like sensors, the test was run continuously. A sequential test of the mean was initiated with each sample and carried forward for a fixed period of time. Each new test contained its own summation of the test statistic and its own expanding

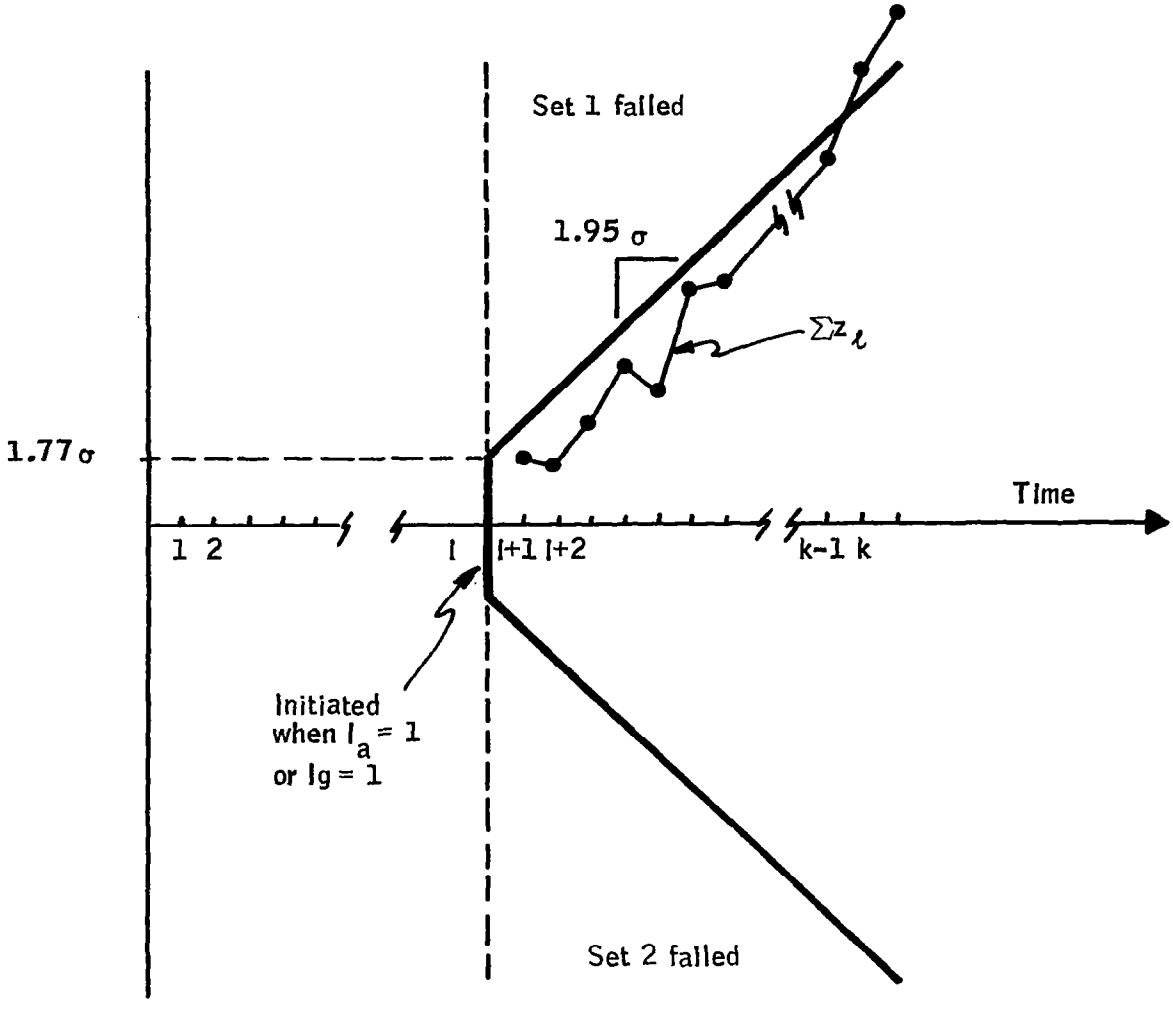

Figure 36. Analytical Test, Design 1

threshold. These were compared at each sample, and failure flag, I_{ar}, was set if any summation exceeded its threshold. For F-8C simulator evaluations, a time period of one second was selected for the maximum test length. At 32 samples per second, this translates into 32 simultaneous sequential tests. A pictorial summary of this design is shown in Figure 37. Note that Design 2 may require larger thresholds than Design 1 since no false alarm rejection is provided by the comparator.

Design 3: The objective of the third analytical redundancy design was simply to detect failures of either the gyro or accelerometer in a single sensor set without providing isolation. Hence, this design used residuals from the min-L_i channel only and included no hardware comparators or redundant channel data.

The design was again based on the sequential likelihood ratio test. Because no redundant data was available, the test statistic was taken to be a direct combination of Kalman filter residuals.

$$z_k = \frac{1}{\sigma_g}(q - \hat{q}^{(i^*)}) + \frac{1}{\sigma_{Nz}}(N_z - \hat{N}_z^{(i^*)})$$

Unlike the difference of likelihood function, this statistic is sensitive to parameter errors as well as sensor failures. The thresholds associated with the sequential likelihood ratio tests were therefore set significantly larger than those of Designs 1 and 2. In all other respects the test was identical to Figure 37.

Simulation Evaluations

The three analytical redundancy concepts above were briefly evaluated on NASA Langley's F-8C simulator to examine their general performance potential. The evaluations consisted of a number of trial "flights" under

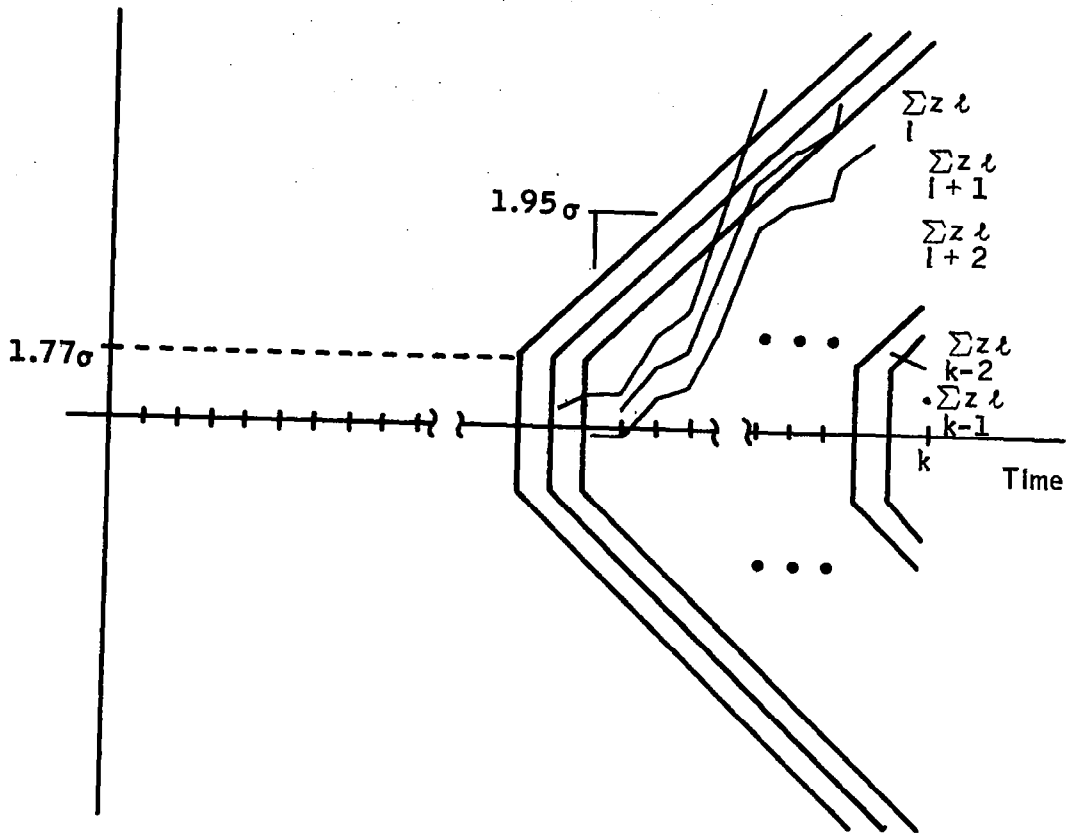

Figure 37. Analytical Test, Design 2

different signal levels and failure mode conditions. The failure modes considered and performance results are summarized below.

Sensor failure modes. - Realistic failure modes are needed to assess the performance of any concept for failure detection. Various sensor failure modes have been hypothesized. Some studies (refs. 9 , 10) have categorized the failure modes as either

- Sudden failures with sudden effects
- Sudden failures with drifting effects.

For this study the the common failure mechanism of a rate gyro and the normal accelerometer were identified (refer to Table 6). The various faults were then reduced to the following modes:

- Zero output
- Zero to hardover step output
- Output sticks and remains at one value during a transient
- High hysteresis
- Low gains.

This mode set is considered inclusive of all significant failures of the sensors in question. Table 6 relates particular sensor faults for the rate gyro, accelerometer and position transducer to the above categories. Note that many specific failure modes of individual sensors can exhibit one or more of the above mode characteristics.

TABLE 6. - SENSORS FAULT CATEGORIES

Fault	Mode
Rate gyro (spring restrained)	
• Open spin motor winding	(1)
• Open pickoff winding	(1)
• Shorted spin motor winding	(1), (4), (5)
• Shorted pickoff winding	(1), (5)
• Broken torsion spring	(2)
• Frozen gimbal	(3)
• Gimbal stiction	(4)
• Open or shorted demodulator	(1), (2), (5)
Accelerometers (electrical force balance)	
• Open or shorted feedback electronics	(1), (2), (5)
• Mass stiction	(4)
• Frozen mass	(3)
Position transducer	
• Open pickoff	(1)
• Shorted pickoff	(1), (5)
• Pickoff stiction	(4)
• Frozen pickoff	(3)

Note:

(1) Zero output

(2) Zero to hardover step output

(3) Output sticks and remains at one value during a transient

(4) High hystersis

(5) Low gains

Performance Summary

The performance potential of the three analytical redundancy concepts was examined by comparing their detection/isolation capability against a "performance standard" achieved by ordinary hardware comparators of like sensors. The latter consists of simple threshold comparison logic

$$I_y = 1 \text{ if } |y_{ch1} - y_{ch2}| > \text{Threshold}$$

with thresholds set according to Table 7. Table 7 represents typical comparator thresholds in operational systems. Only the first term of each threshold was used in the simulation because alignment and scale factor errors which motivate the remaining terms were not included in the sensor models.

TABLE 7. - TYPICAL COMPARATOR THRESHOLDS

Sensor	Threshold
Rate gyro	$4/3 * [.0255 * \|FS\| + .035 * \|q\| + .866/57.3\|p\|]$
Accelerometer	$4/3 * [.012 * \|FS\| + .056\|N_z\|]$
	FS = full scale output

Detection/isolation capability was evaluated for all five failure modes (per sensor) and for five signal levels:

1) Adaptive test signal only
2) 1 m/sec turbulence
3) 2 m/sec turbulence
4) C* command = 3 m/sec^2
5) C* command = 10 m/sec^2

Results for the hardware comparison "standard" are shown in Table 8. It should be noted that the standard is not perfect. "Covert" failures (denoted by arrows) require significant excitation (either gusts or commands) in order for the failure to be detected. This is of interest since these covert failure modes will be examined with analytical redundancy to determine the corresponding signal levels.

TABLE 8. - COMPARATOR PERFORMANCE*

Failure simulated	Excitation, Test signal	1 m/s gust	2 m/s gust	C*=3 m/s	C*=10 m/s	
Gyro--Dead	0	X	X	X	X	←
Gyro--H. O.	X	X	X	X	X	
Gyro--Stuck	0	X	X	X	X	
Gyro--50% Gain	0	0	0	0	X	←
Gyro--Hyst.	0	0	0	X	X	←
Accel--Dead	X	X	X	X	X	
Accel--H. O.	X	X	X	X	X	
Accel--Stuck	0	0	X	X	X	←
Accel--50% Gain	X	X	X	X	X	
Accel--Hyst.	0	X	X	X	X	←

* X = Failure detected

Results for the three analytical redundancy designs are shown in Table 9. Note that all tests can detect the overt failures but the ability to catch covert failures varies. Specific failure detection is depicted by the corresponding design number given in the table. Time histories for representative conditions are given in the Appendix.

Qualitative conclusions which can be drawn from comparisons of Tables 8 and 9 are summarized in Table 10.

TABLE 9. - PERFORMANCE SUMMARY FOR ANALYTICAL REDUNDANCY DESIGNS

Failure simulated	Excitation,				
	Test signal	3F/s gust	6F/S gust	C*=10	C*=30
Gyro--Dead	---	---	---	1	1, 2
Gyro--H. O.	1, 2, 3	1, 2, 3	1, 2, 3	1, 2, 3	1, 2, 3
Gyro--Stuck	---	---	---	1	1, 2
Gyro--50% Gain	---	---	---	---	1, 2
Gyro--Hyst.	---	---	---	---	1
Accel--Dead	1, 2, 3	1, 2, 3	1, 2, 3	1, 2, 3	1, 2, 3
Accel--H. O.	1, 2, 3	1, 2, 3	1, 2, 3	1, 2, 3	1, 2, 3
Accel--Stuck	---	---	---	---	---
Accel--50% Gain	1, 2, 3	1, 2, 3	1, 2, 3	1, 2, 3	1, 2, 3
Accel--Hyst.	---	---	---	---	---

TABLE 10. - ANALYTICAL REDUNDANCY CONCLUSIONS

Test	Objective	Performance
1	Detect and isolate one of two channels	Almost as good as hardware comparison to detect and isolate one of three channels
2	Detect and isolate one of two channels	Not as good as Test 1
3	Detect failure in one channel	Not as good as hardware comparison to detect failures in one of two channels (no isolation) Test 3 catches overt failures only

Sensor Fault Detection Requirements

While the simulation results show promising failure detection/isolation potential for at least one design, these results are preliminary in nature and much additional evaluation effort will be required to fully assess the designs. In order to establish objective goals for such future evaluations, an effort was made to derive qualitative performance requirements for analytical redundancy concepts in general. Now, we will discuss these derivations. They show that analytical failure detection tests must reach missed alarm rates less than approximately 3.0 percent in order to be competitive with direct voting schemes using redundant hardware. False alarm rates, of course, must also be acceptable ($\leq 10^{-3}$/flight hours). Further Monte Carlo-type simulations are recommended to evaluate the analytical redundancy designs against these requirements.

Basic flight control reliabilities. - The contributions of automatic flight control systems to aircraft effectiveness have increased the reliance on their operation for satisfying mission and flight safety requirements. These requirements are often quantified as probabilities. For example, the probability of a catastrophic failure must not exceed approximately 10^{-7} per hour of flight (one chance in ten million). Mission abort probabilities are on the order of 10^{-3} per flight hour, (ref. 15).

In spite of continual improvements in component quality, a non-redundant electronic flight control system still exceeds these allowable fly-by-wire flight safety failure rates by about a factor of 1000 (ref. 15). Thus redundant configurations are a necessity.

Various levels of redundancy are commonly classified according to the ability of the system to accommodate failures; e.g., "fail safe", "single-fail-operate" or "dual-fail-operate". The single and dual refer to the number of like failures that can be tolerated without loss of system function. Failure

detection is primarily accomplished by comparison monitoring of like outputs. With this limitation the following parallel between failure accommodation level and redundancy configuration are common (ref. 16).

- Fail safe → 2 channels
- Single-fail-operate → 3 channels
- Dual-fail-operate → 4 channels

Basic sensor reliabilities. - Because analytical redundancy procedures are primarily concerned with sensor failures, it is useful to consider that fraction of the above flight control requirements which is allocated to the sensors. Conservatively, this will be 10 percent of the total budget. This allocation is then further subdivided among individual instruments. Assuming a complement of 10 sensors gives:

Probability of total failure $\leq 10^{-9}$ per sensor per hour

Probability of mission abort $\leq 10^{-5}$ per sensor per hour.

As with the overall flight control system, nonredundant sensors fall well short of these requirements. Current failure rates for rate gyros, for example, are 10^{-4} per hour (one of the worst of the sensor failure rates). Hence, redundant sensor configurations are also a necessity.

Reliabilities for redundant configurations. - To examine the reliability characteristics of redundant sensors, consider a fly-by-wire application with quad sensors. The usual approach to management of the set of four is to isolate the first and second failed sensors by majority vote, with the third failure (sensed by a miscomparison between the remaining two sensors) resulting in total disengagement. If the monitoring process is perfect, the probability of total failure of the set is approximated by $4Q_s^3$, where Q_s is the probability of failure of one of the sensors in the selected time period. Under

the same assumption, the probability of failure of any two sensors is $6Q_s^2$, a number of significance to the mission abort probability. In terms of current sensor failure rates, the above probabilities are exceedingly small numbers. Taking a rate gyro as an example gives

$$\text{Probability of total failure} = 4Q_s^3 = 4 \times 10^{-12}$$

$$\text{Probability of mission abort} = 6Q_s^2 = 6 \times 10^{-8}$$

where each applies to a one-hour flight. Consequently, the quad sensor set (with perfect monitoring) exceeds requirements by about two orders of magnitude. This appears to be an overdesign.

If a majority-voted triple set were hypothesized instead of the quad, however, the associated flight safety and mission abort probabilities of $3Q_s^2$ and $3Q_s$ would produce values of 3×10^{-8} and 3×10^{-4}, respectively. These values fall short of the above requirements by a factor of 30. The situation is simply that with conventional comparison monitoring, triple is not good enough and quad is too good.

Complicating the above argument (and changing some of the conclusions) is the issue of nonperfect monitoring, which in itself is difficult to deal with quantitatively. One attempt to do so argues that a nondetected failure may cause quad set failure after the second sensor failure (instead of after the third), producing an added total failure contribution of $6Q_s^2 Q_m$, where Q_m is the probability of having the first failure occur without being detected and that both of the actual sensor failures are alike. The result of such a combination of events is that the quad voting logic cannot decide with two good like sensors versus two bad like sensors. A common example of this situation is having two sensors fall dead in an interval where insufficient control activity (e.g., cruise) occurs to trip monitors. There is no data available to assign numbers to Q_m, but a parametric study of its potential effects soon

convinces one that it is a significant and probably a dominant contributor to total failure rate. For example, speculated values for Q_m are in the order of 10^{-2}, making the $6Q_s^2 Q_m$ term (again for a rate gyro) equal to 6×10^{-9} for the one-hour flight, just within requirements. So now with imperfect monitoring considered, the quad set may no longer be "too good", but just good enough.

The relevance of the above discussion to analytical redundancy requirements lies primary in the notion that imperfect monitoring (an element of redundancy mismanagement) is probably the pacing cause for failure of highly redundant sensor sets. The quality of the required analytical diagnostics must be viewed in this perspective. Consider, as an example, an analytical redundancy application wherein triple sensors are to be configured for dual-fail-op performance. The first failure will be "voted out" by comparison logic. The second failure will be detected by comparison monitoring and isolated by the analytical diagnostic. The resulting total failure rate is $Q_s^3 + 3Q_s^2 Q_D$, where the second term represents the probability of a dual sensor failure and Q_D is the probability of failure of the diagnostic to pick the bad sensor. Judging the second term to be dominant and equating it to the 10^{-9} requirement speculated above,

$$3Q_s^2 Q_D = 10^{-9}$$

or $Q_D = 0.033$ for a rate gyro set, meaning that the analytical test must be correct in about 97 percent of the decisions made to distinguish a good sensor from a bad sensor. This performance appears feasible. Note also that the source of failure experienced in the conventional quad set due to imperfect monitoring is also present in the above triple set, but it is half as probable in the triple. It may simply be included as a contribution to Q_D.

In terms of mission reliability, the triple set speculated above will be aborted after the second failure, a probability of $3Q_s^2$. This is lower than the quad set by a factor of two.

The above reliability figures for quad and triplex systems are summarized in Table 11. A similar application of analytical redundancy can also be made to dual sensor configurations (see Table 12). Here it is assumed that another backup system is available. Thus if the dual sensors disagree, the system can be safely disengaged. Referring to Table 12, it is noted that a dual sensor system does not meet mission abort requirements. This can be greatly improved if analytical redundancy is used to select the remaining good sensor. By comparing system failure probabilities and mission abort probabilities, a probability of a correct decision of 95 percent satisfies typical specifications. That is, a 5 percent missed alarm rate is adequate for the analytical diagnostic in this application.

Both Tables 11 and 12 suggest that analytical redundancy concepts can make meaningful contributions to overall system reliability even with modest performance capabilities. Based on these findings, it is recommended that work on Design 1 be continued. The benefit of maneuver dependent thresholds should be examined and flight data should be used to verify that the decision quality of the algorithm can be made to satisfy the above requirements.

TABLE 11. - RELIABILITY CHARACTERISTICS OF QUAD AND TRIPLEX SENSOR SYSTEMS

Typical specification	Failure probability for selected redundancy structures			
	Quad, perfect monitor	Quad, with imperfect monitor[1]	Triplex	Triplex with analytical redundancy[2]
System failure (10^{-9} per sensor)	$4Q_S^3 = 4\times10^{-12}$	$4Q_S^3 + 6Q_S^2Q_M = 0.6\times10^{-9}$	$3Q_S^2 = 3\times10^{-8}$	$Q_S^3 + 3Q_S^2Q_D = 10^{-9}$
Mission abort (10^{-5} per sensor)	$6Q_S^2 = 6\times10^{-8}$	$6Q_S^2 = 6\times10^{-8}$	$3Q_S = 3\times10^{-4}$	$3Q_S^2 = 3\times10^{-8}$

NOTES:

[1] $Q_M = 0.02$

[2] $Q_D = 0.033$

TABLE 12. - RELIABILITY CHARACTERISTICS OF DUAL SENSOR SYSTEMS

Typical specification	Failure probability for selected redundancy structure	
	Dual	Dual with analytical redundancy
Total system failure (10^{-9} per sensor)	0*	$Q_S^2Q_D = 10^{-9}$ (If $Q_D = 0.01$)
Mission abort (10^{-5} per sensor)	$2Q_S = 2\times10^{-4}$	$2Q_SQ_D = 10^{-5}$ (If $Q_D = 0.05$)

*Alternate backup assumed.

SECTION 6
CONCLUSIONS AND RECOMMENDATIONS

The extension studies documented in this report have examined three areas of refinement for the baseline F-8C adaptive control system designed in (ref. 1).

- Accuracy improvements for pitch axis identification
- Lateral axis identification
- Analytical redundancy techniques

Significant results were achieved in each area.

The pitch study has shown that on-line adjustment of gust level statistics improves accuracy of the baseline identifier and/or reduces test signal requirements. It can be readily implemented by discrete gust level discrimination techniques. A two-level case was demonstrated which adds a single parallel channel and a second set of stored filter gains to the identifier. These extra elements are recommended as permanent modifications of the baseline design. Accuracy improvements have also been demonstrated for rapid flight transitions. These were achieved with better trim compensation and with basic modifications of the underlying MLE design theory. The latter results replace the baseline identifier's Newton-Raphson correction step with a Kalman filter correction step designed for dynamic parameter models. This change is also recommended as a permanent modification of the baseline design. The only negative result of the pitch-axis study is that attitude data provides no significant accuracy improvement.

The lateral-axis study has shown that inertially coordinated command augmentation is feasible without air data measurements. A lateral MLE identifier was designed with sufficient transient accuracy (during large maneuvers) to schedule the full state lateral CAS (ref. 6). The combined

lateral adaptive system exhibits excellent dutch roll damping and good turn coordination. Further study of this concept is recommended, with emphasis on simplifying the identifier.

Finally, the analytical redundancy study has shown that the baseline identifier, augmented with one additional parallel channel to process redundant sensor data, has significant capabilities for fault detection and isolation of gyros and accelerometers. Although evaluation results in this area are limited, they indicate that at least one of three suggested analytical redundancy procedures is worthy of further development and evaluation.

SECTION VII
REFERENCES

1. Hartmann, G. L., et al "F-8C Adaptive Flight Control Laws" Final Report Contract NASI - 13383. (NASA CR-2880, 1977)

2. Mehra, R. K., Stepner, D. E. and Tyler, J. S., "A Generalized Method for Identification of Aircraft Stability and Control Derivatives from Flight Test Data" 1972 JACC.

3. Woolly, C. T., "A Real-Time Hybrid Simulation of a Digital Fly-By-Wire Aircraft"" 1974 Summer Computer Simulation Conference, Houston, TX July 1974.

4. Lee, R. C. K. Optimal Estimation Identification and Control Research Monograph No. 28, MIT Press, Cambridge, Mass. 1964.

5. U. S. Standard Atmosphere, 1972, U. S. Government Printing Office, Washington 25, D. C.

6. Hartmann, G. L., Hauge, J. A., Hendrick, R. C., "F-8C Digital CCV Flight Control Laws", NASA Contractor Report, NASA CR-2629, February 1976.

7. Bassett, K., Yechout, T., Oelschlaeger, D. and Hendrick R., "A Digital Multimode Flight Control System for Tactical Fighters" NEACON Proceedings, Dayton, Ohio, May 13 - 15, 1974.

8. Mehra, R. K. and Peschon, J., "An Innovations Approach to Fault Detection and Diagnosis in Dynamic Systems," Automatics, Vol. 7 pp. 637-640, 1971.

9. Meier, L., Ross, D. W., Glaser, M. B., Evaluation of the Feasibility of Using Internal Redundancy to Detect and Isolate On-Board Control Data Instrumentation Failures, AFFDL-TR-70-172, January 1971.

10. Maybeck, Peter S., Failure Detection Through Functional Redundancy, AFFDL-TR-74-3, January 1974.

11. Kerr, T. H., "A Two Ellipsoid Overlap Test for Real Time Failure Detection and Isolation by Confidence Regions," IEEE Conference on Decision and Control, November 1974, Phoenix, Arizona.

12. Montgomery, R.C. and Price, D.B., "Management of Analytical Redundancy in Digital Flight Control Systems for Aircraft," AIAA Mechanics and Control of Flight Conference, Anaheim, California, August 5-9, 1974.

13. Willsky, A.S., Deyst, J.J., and Crawford, B.S., "Adaptive Filtering and Self-Test Methods for Failure Detection and Compensation," Proc. of the 1974 JACC, Austin, Texas, June 19-21, 1974.

14. B. W. Lindgren, Statistical Theory, The MacMillan Company, London 1969

15. Hendrick, R.C. et al Design Criteria for High Authority Closed Loop Primary Flight Control Systems. Wright-Patterson AFB, Ohio AFFDL-TR-71-78, August 1972.

16. Hendrick, R.C. and Hill, C.D., "Self-Testing Digital Flight Control Applications," AIAA Digital Avionic Systems Conference, Boston, Mass. February 1975.

APPENDIX A

PITCH AND LATERAL IDENTIFIER FLOW DIAGRAM

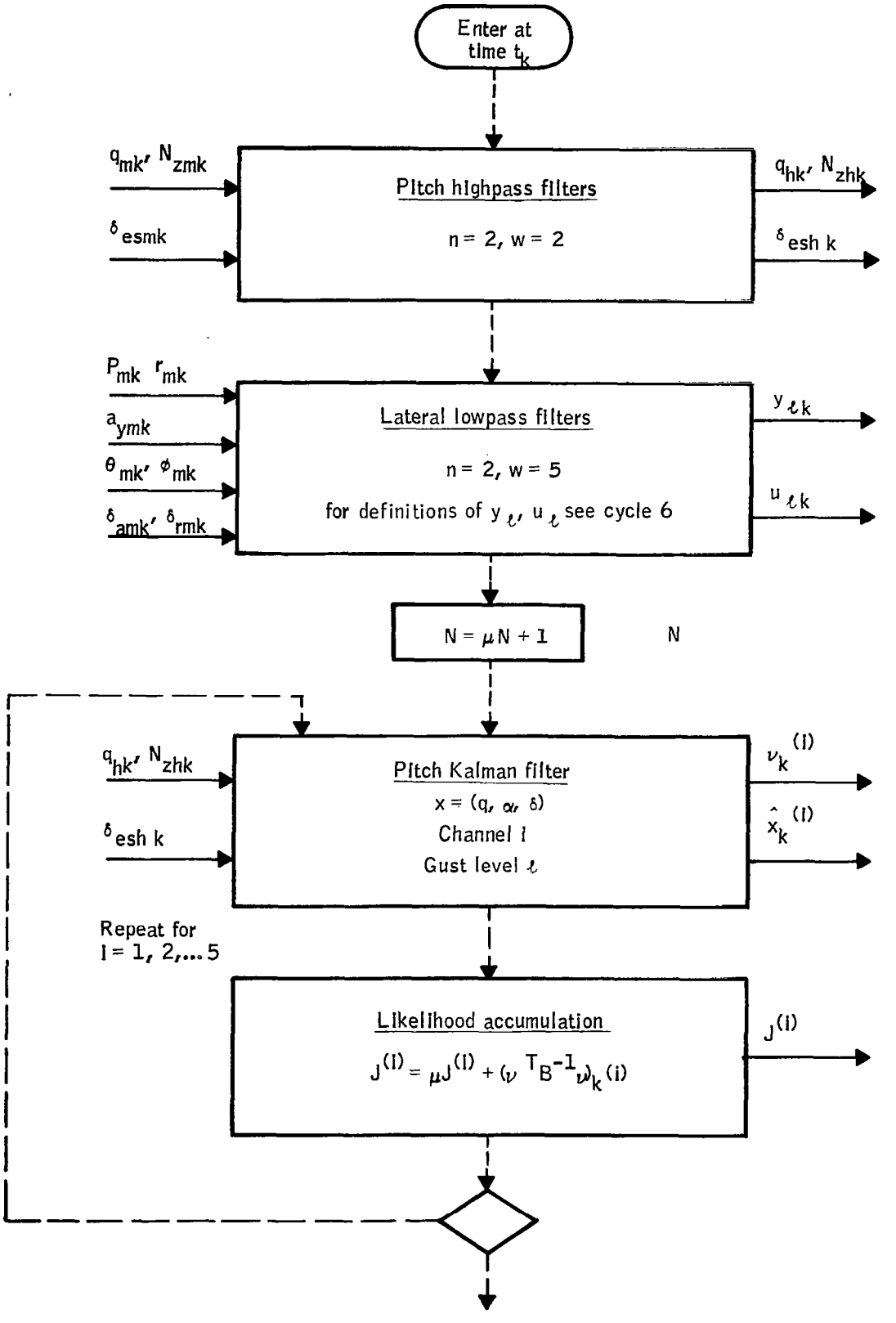
Enter at time t_k
q_{mk}, N_{zmk}
δ_{esmk}
Pitch highpass filters
n = 2, w = 2
q_{hk}, N_{zhk}
$\delta_{esh\,k}$
P_{mk} r_{mk}
a_{ymk}
θ_{mk}, ϕ_{mk}
δ_{amk}, δ_{rmk}
Lateral lowpass filters
n = 2, w = 5
for definitions of y_ℓ, u_ℓ see cycle 6
$y_{\ell k}$
$u_{\ell k}$
$N = \mu N + 1$
N
q_{hk}, N_{zhk}
$\delta_{esh\,k}$
Pitch Kalman filter
x = (q, α, δ)
Channel I
Gust level ℓ
$\nu_k^{(I)}$
$\hat{x}_k^{(I)}$
Repeat for
I = 1, 2,... 5
Likelihood accumulation
$J^{(I)} = \mu J^{(I)} + (\nu\ T_B^{-1} \nu)_k(I)$
$J^{(I)}$

Appendix A

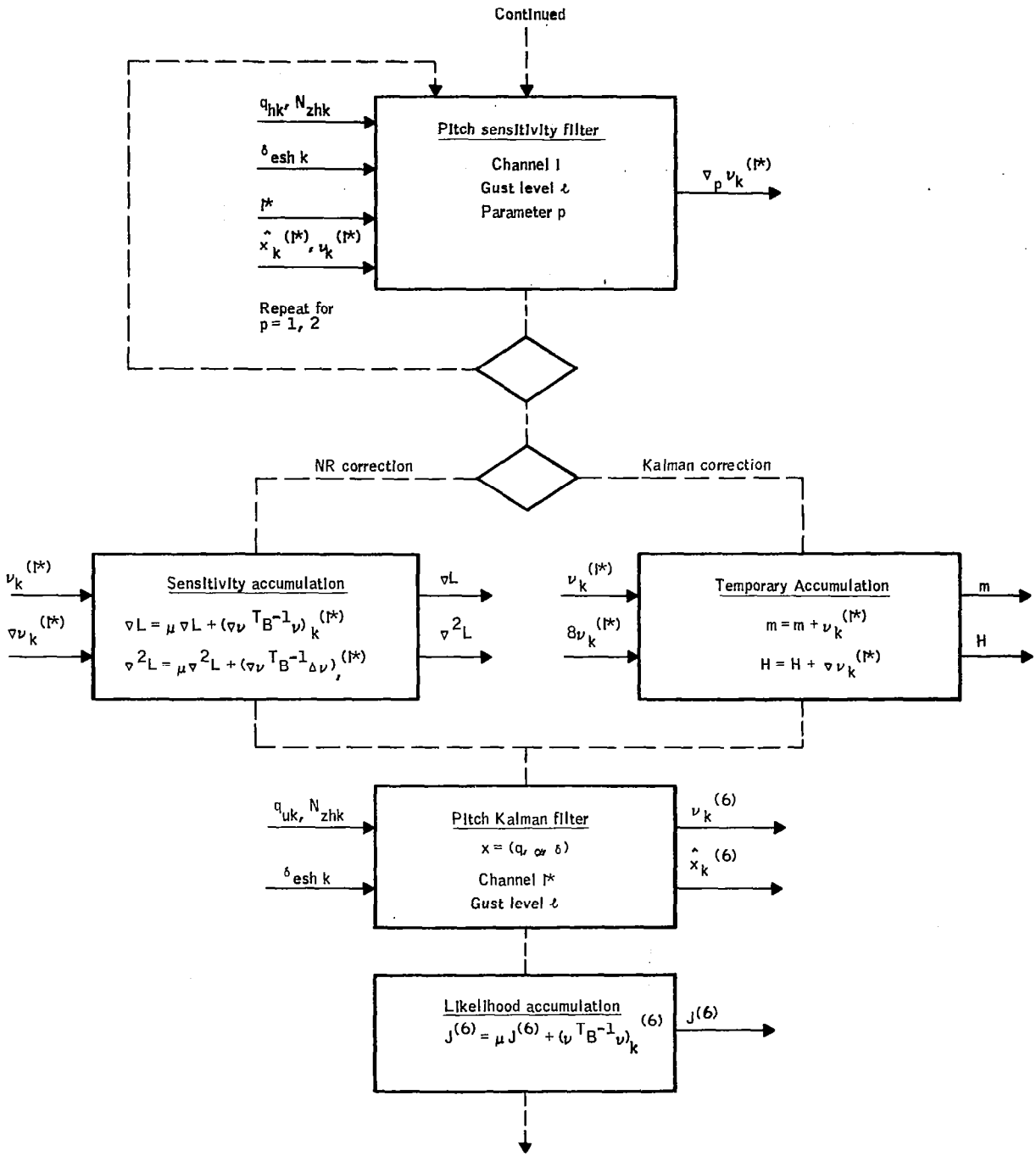
Continued
q_{hk}, N_{zhk}
$\delta_{esh\,k}$
l^*
$\hat{x}_k^{(l^*)}$, $\nu_k^{(l^*)}$
Pitch sensitivity filter
Channel l
Gust level ℓ
Parameter p
$\nabla_p \nu_k^{(l^*)}$
Repeat for
p = 1, 2
NR correction
Kalman correction
$\nu_k^{(l^*)}$
$\nabla\nu_k^{(l^*)}$
Sensitivity accumulation
$\nabla L = \mu \nabla L + (\nabla\nu\ ^T B^{-1}\nu)_k^{(l^*)}$
$\nabla^2 L = \mu \nabla^2 L + (\nabla\nu\ ^T B^{-1}\Delta\nu)_k^{(l^*)}$
∇L
$\nabla^2 L$
$\nu_k^{(l^*)}$
$\delta\nu_k^{(l^*)}$
Temporary Accumulation
$m = m + \nu_k^{(l^*)}$
$H = H + \nabla\nu_k^{(l^*)}$
m
H
q_{uk}, N_{zhk}
$\delta_{esh\,k}$
Pitch Kalman filter
$x = (q, \alpha, \delta)$
Channel l^*
Gust level ℓ
$\nu_k^{(6)}$
$\hat{x}_k^{(6)}$
Likelihood accumulation
$J^{(6)} = \mu J^{(6)} + (\nu\ ^T B^{-1}\nu)_k^{(6)}$
$J^{(6)}$

Appendix A

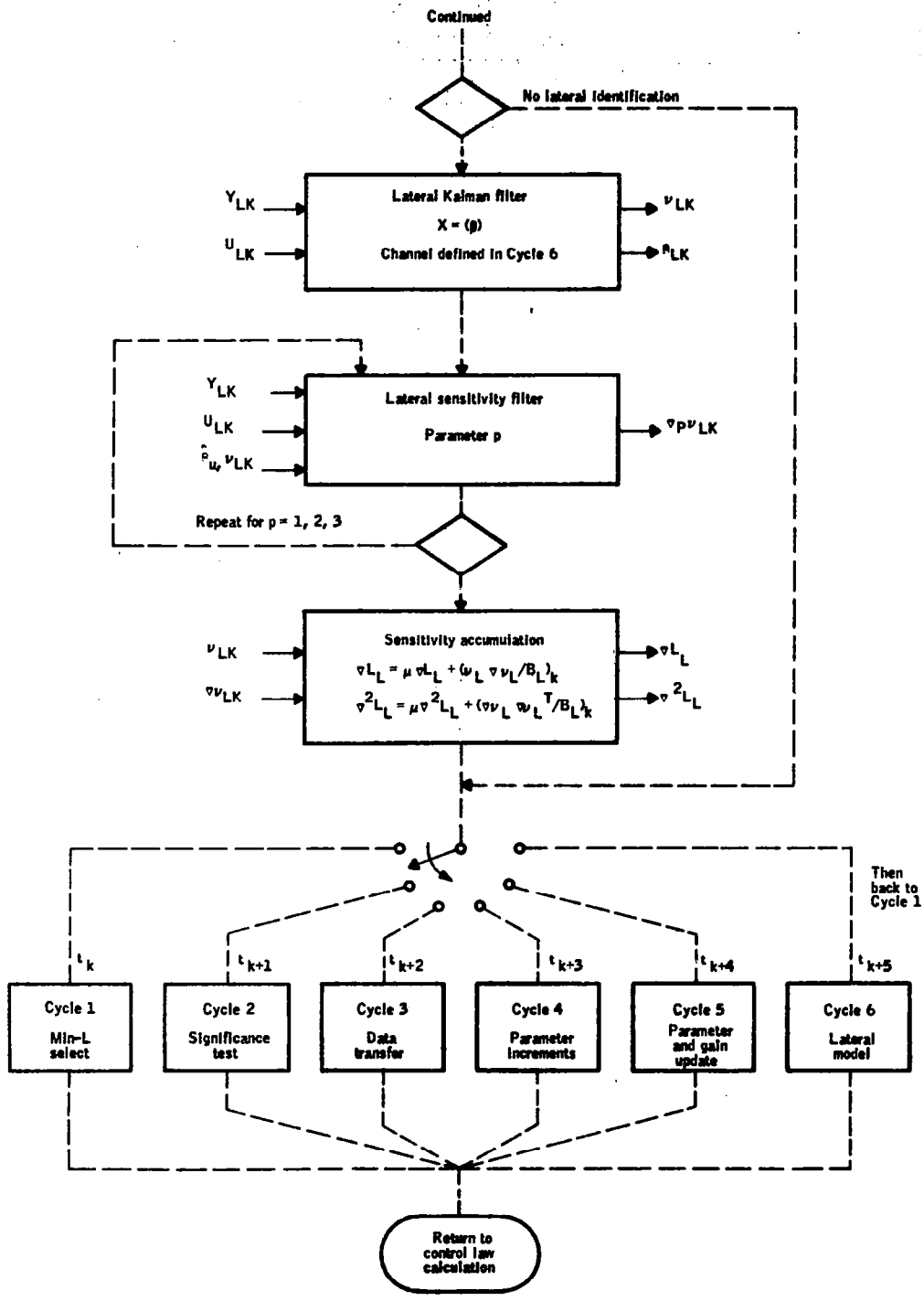
Continued
No lateral identification
Lateral Kalman filter
X = (p)
Channel defined in Cycle 6
Lateral sensitivity filter
Parameter p
Repeat for p = 1, 2, 3
Sensitivity accumulation
Then back to Cycle 1
Cycle 1
Min-L select
Cycle 2
Significance test
Cycle 3
Data transfer
Cycle 4
Parameter increments
Cycle 5
Parameter and gain update
Cycle 6
Lateral model
Return to control law calculation

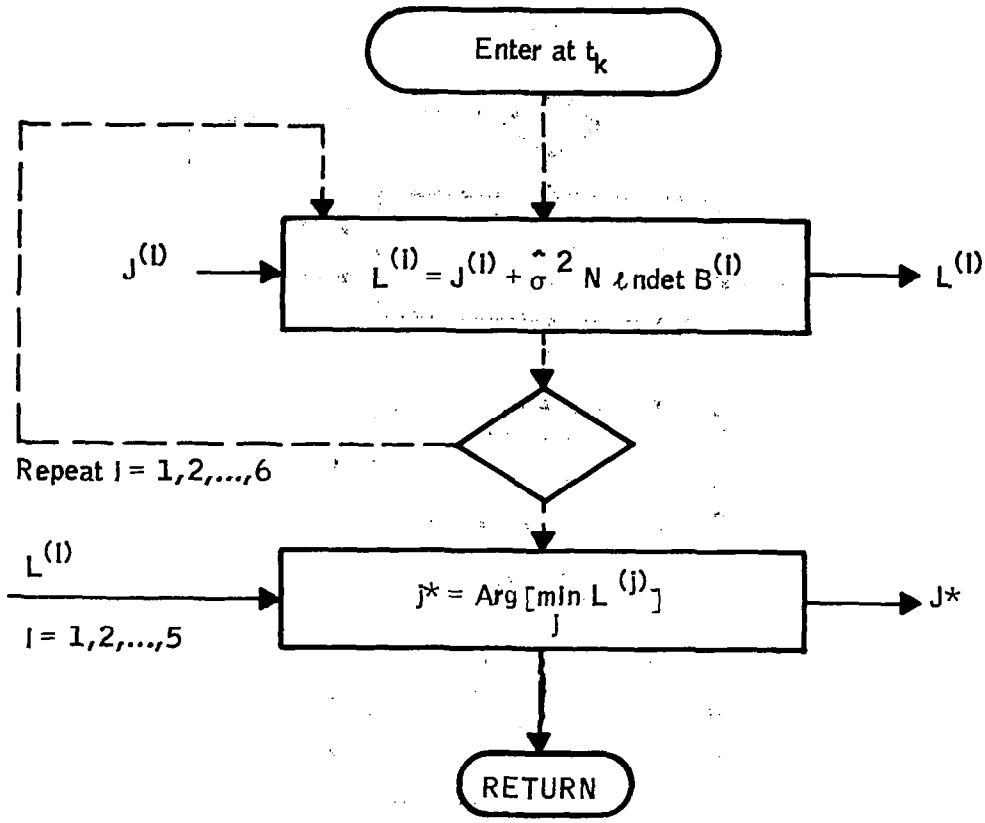

Cycle 1 = Min - L selection

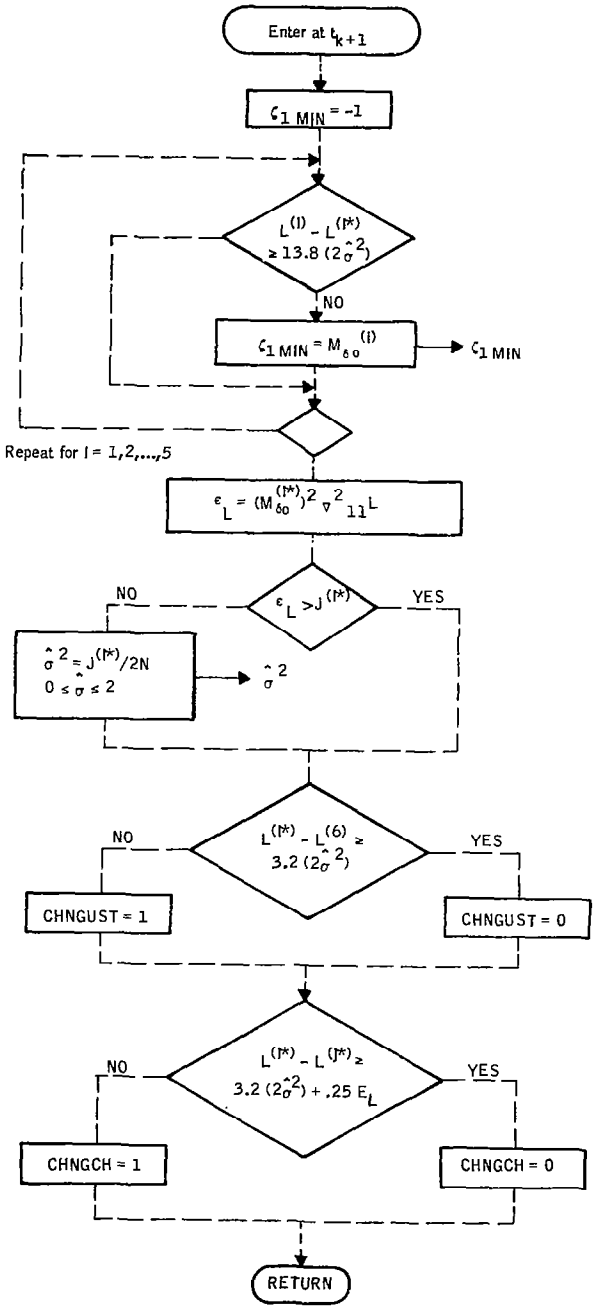

Cycle 2: Significance Test and Change Logic

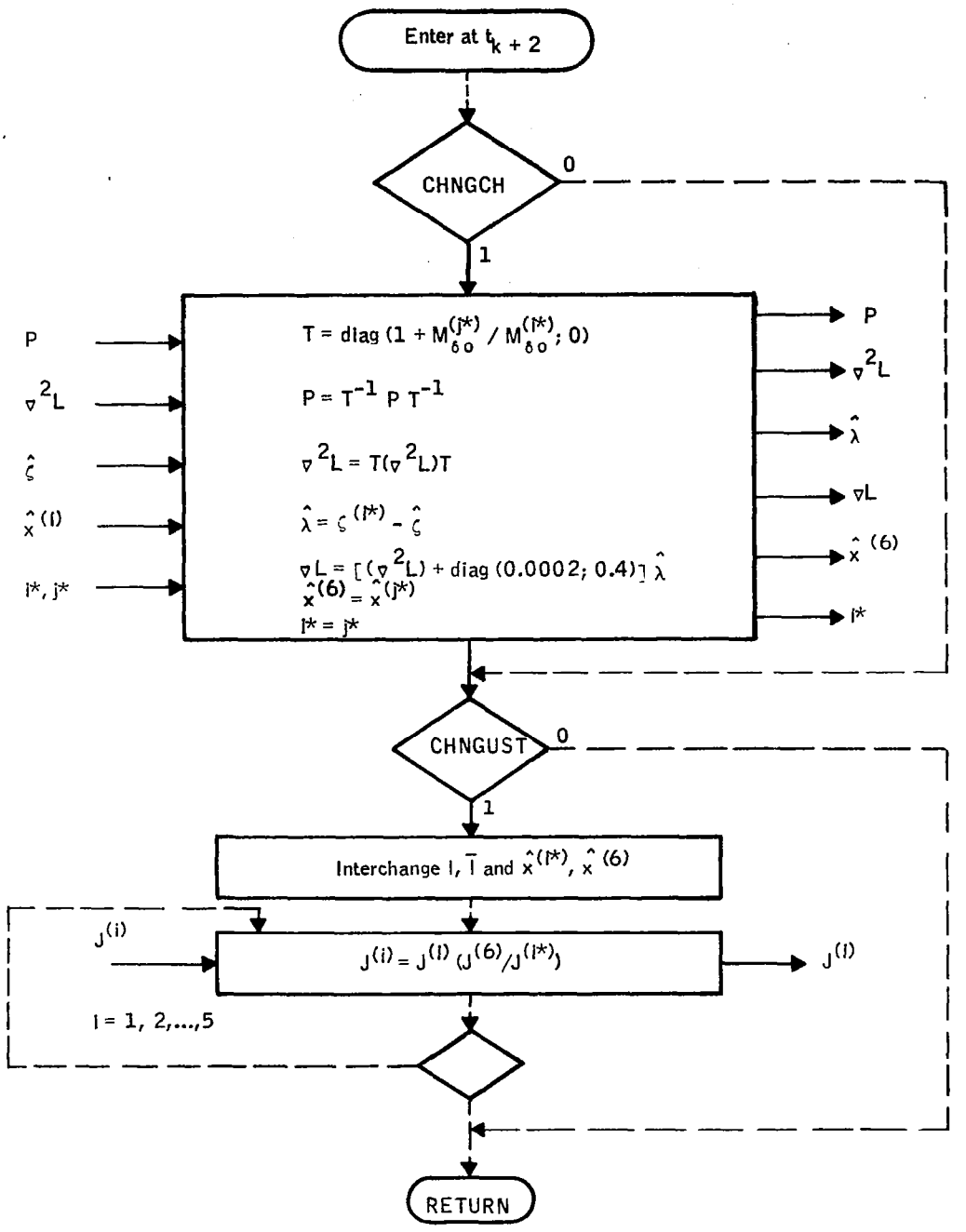

Cycle 3: Channel Data Transfer

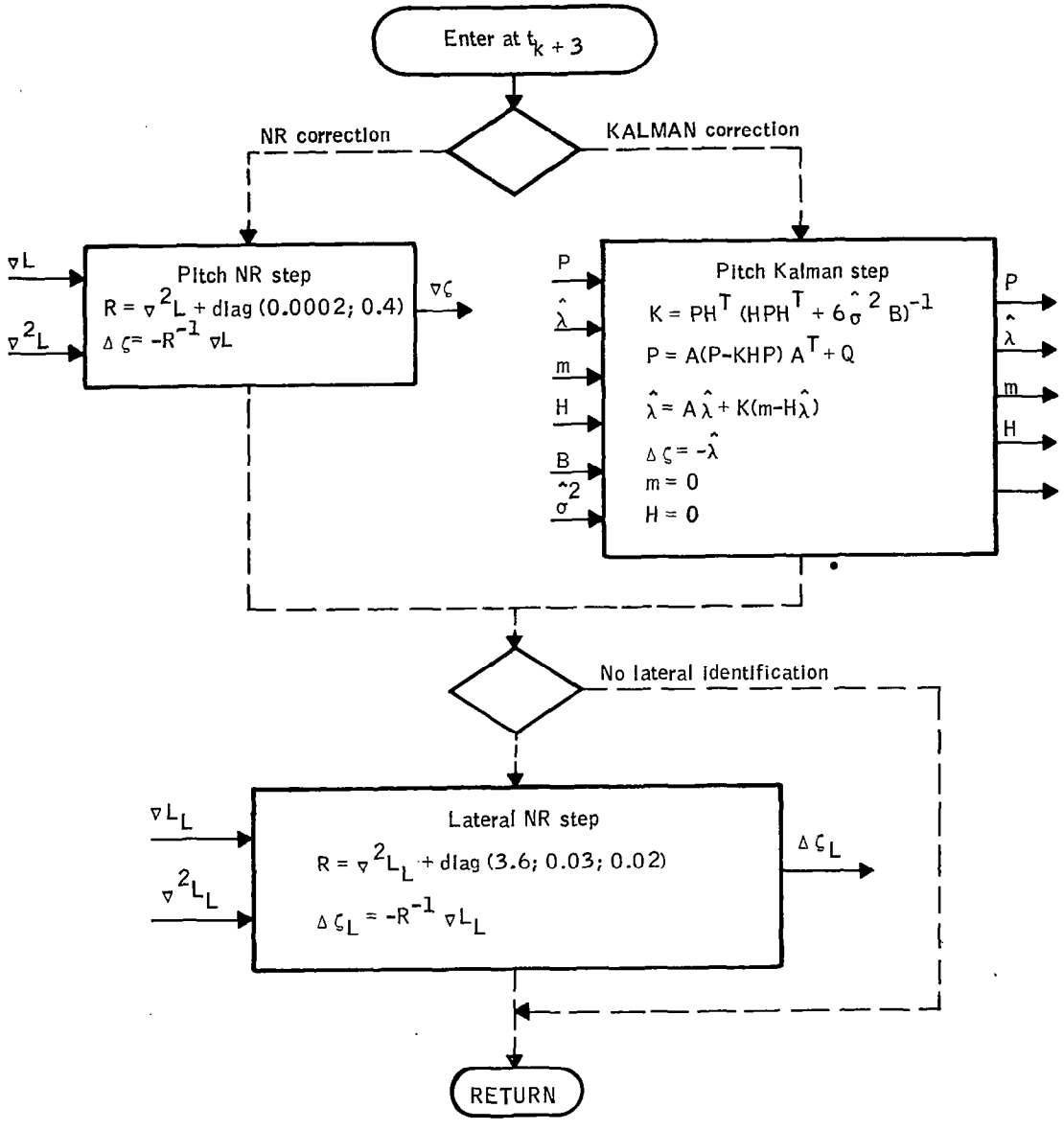

Cycle 4: Parameter increments

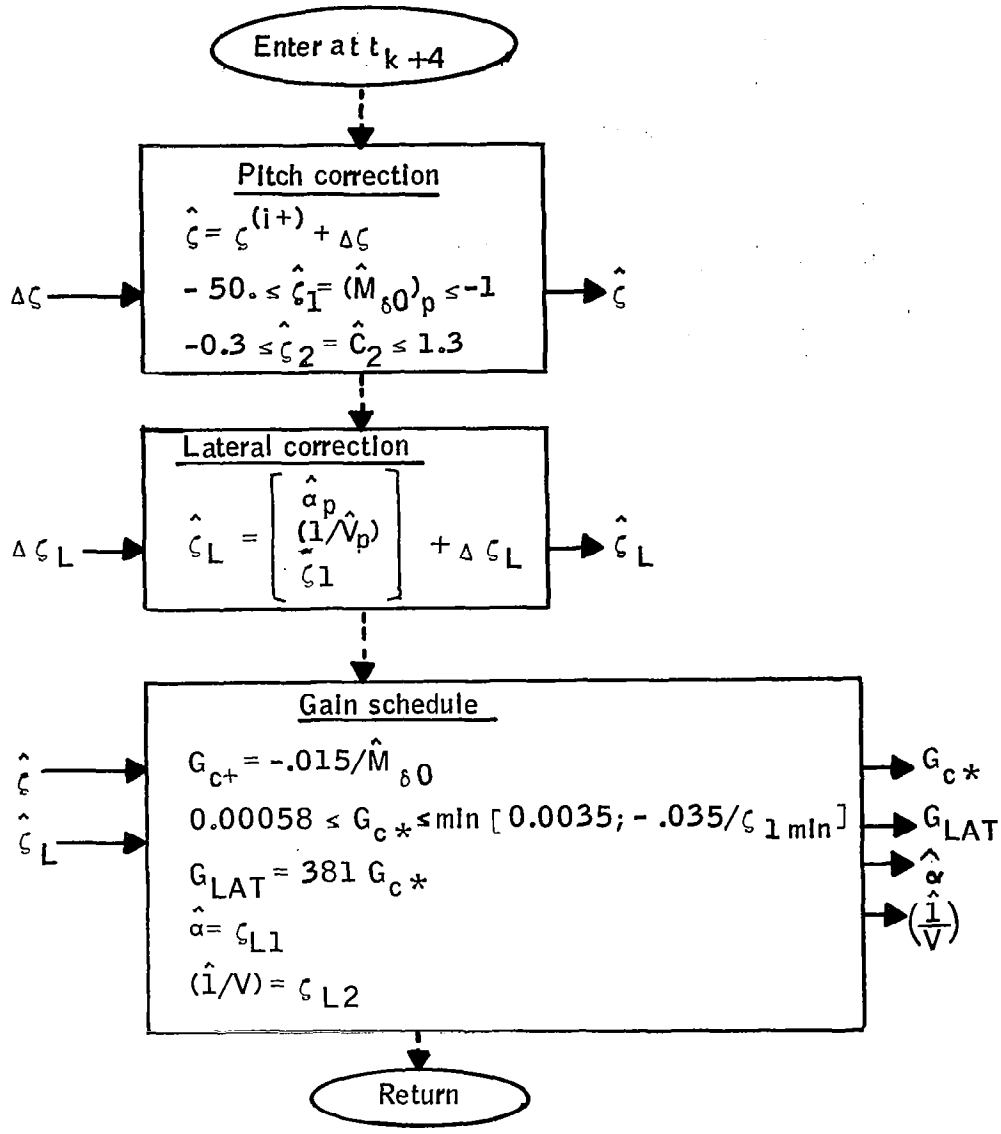

Cycle 5: Parameter and Gain Updates

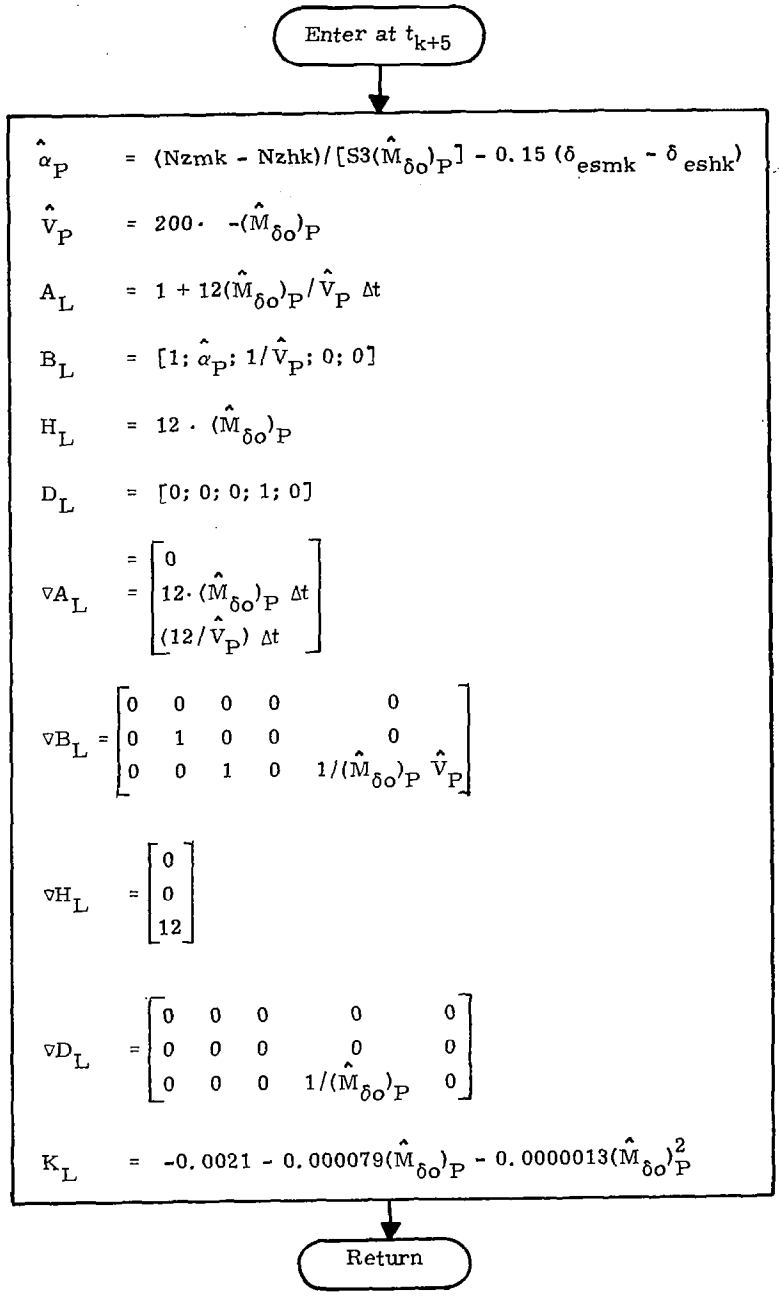
Enter at t_{k+5}
$\hat{\alpha}_P = (Nzmk - Nzhk)/[S3(\hat{M}_{\delta o})_P] - 0.15\,(\delta_{esmk} - \delta_{eshk})$
$\hat{V}_P = 200 \cdot -(\hat{M}_{\delta o})_P$
$A_L = 1 + 12(\hat{M}_{\delta o})_P / \hat{V}_P\,\Delta t$
$B_L = [1;\ \hat{\alpha}_P;\ 1/\hat{V}_P;\ 0;\ 0]$
$H_L = 12 \cdot (\hat{M}_{\delta o})_P$
$D_L = [0;\ 0;\ 0;\ 1;\ 0]$
$\nabla A_L = \begin{bmatrix} 0 \\ 12 \cdot (\hat{M}_{\delta o})_P\,\Delta t \\ (12/\hat{V}_P)\,\Delta t \end{bmatrix}$
$\nabla B_L = \begin{bmatrix} 0 & 0 & 0 & 0 & 0 \\ 0 & 1 & 0 & 0 & 0 \\ 0 & 0 & 1 & 0 & 1/(\hat{M}_{\delta o})_P\ \hat{V}_P \end{bmatrix}$
$\nabla H_L = \begin{bmatrix} 0 \\ 0 \\ 12 \end{bmatrix}$
$\nabla D_L = \begin{bmatrix} 0 & 0 & 0 & 0 & 0 \\ 0 & 0 & 0 & 0 & 0 \\ 0 & 0 & 0 & 1/(\hat{M}_{\delta o})_P & 0 \end{bmatrix}$
$K_L = -0.0021 - 0.000079(\hat{M}_{\delta o})_P - 0.0000013(\hat{M}_{\delta o})_P^2$
Return

The lateral model defined in this cycle accepts the following quantities as inputs and outputs

$$y = N_y - (Y_{\delta r} V)\, \delta r_m - (Y_{\delta a} V)\, \delta a_m - d \frac{d}{dt} r_m$$

y_ℓ = low passed version of y

$$u = \begin{bmatrix} -\Delta t\, r_m \\ \Delta t\, p_m \\ \Delta t\, [g \cos \theta_m \sin \phi_m + (Y_{\delta r} V)\, \delta r_m + (Y_{\delta a} V)\, \delta a_m] \\ [(Y_{\delta r} V)\, \delta r_m + (Y_{\delta a} V)\, \delta a_m]\, (\hat{M}_{\delta o})_p \\ \Delta t\, [(Y_{\delta r} V)\, \delta r_m + (Y_{\delta a} V)\, \delta a_m] / \hat{V}_p\, (\hat{M}_{\delta o})_p \end{bmatrix}$$

u_ℓ = low passed version of u

Cycle 6: Lateral Model Definition

APPENDIX B

ANALYTICAL REDUNDANCY SIMULATION TIME HISTORIES

APPENDIX B
ANALYTICAL REDUNDANCY SIMULATION TIME HISTORIES

This appendix contains some representative time histories that illustrate the performance of the analytical redundancy concepts. Both normal operation and simulated failures are considered for a variety of input conditions. The cases are given in Table B1 below.

TABLE B1. REPRESENTATIVE TIME HISTORIES

Figure	Condition
B1	Residuals and likelihood differences at FC1 with no failure and test signal plus sensor noise (TS + SN), 2 m/s gusts, Thunderstorm (7 m/s gusts) and C* command
B2	Simulated accelerometer failure - high hysteresis at FC1
B3	Simulated accelerometer failure - stuck at FC1
B4	Simulated gyro failure - high hysteresis at FC1
B5	Simulated gyro failure - dead at FC1
B6	Simulated gyro failure - low gain at FC1
B7	Residuals and likelihood differences at FC10 with no failures. Test signal and sensor noise (TS + SN) and 2 m/s gusts recorded at CH2 and CH4 (correct channel)
B8	Residuals and likelihood differences at FC5 with no failures. TS + SN, commands and gust inputs
B9	Residuals and likelihood differences at FC8 with no failures. TS + SN, command and gust inputs.

For simulated failures the excitation is labeled at the top of each figure.

OK	=	Test signal and no failure simulated
LG	=	Low gust level (rms=1 m/sec)
HG	=	High gust level (rms=2 m/sec)
LC	=	Small C* command (3 m/sec^2)
HC	=	Large C* command (10 m/sec^2)

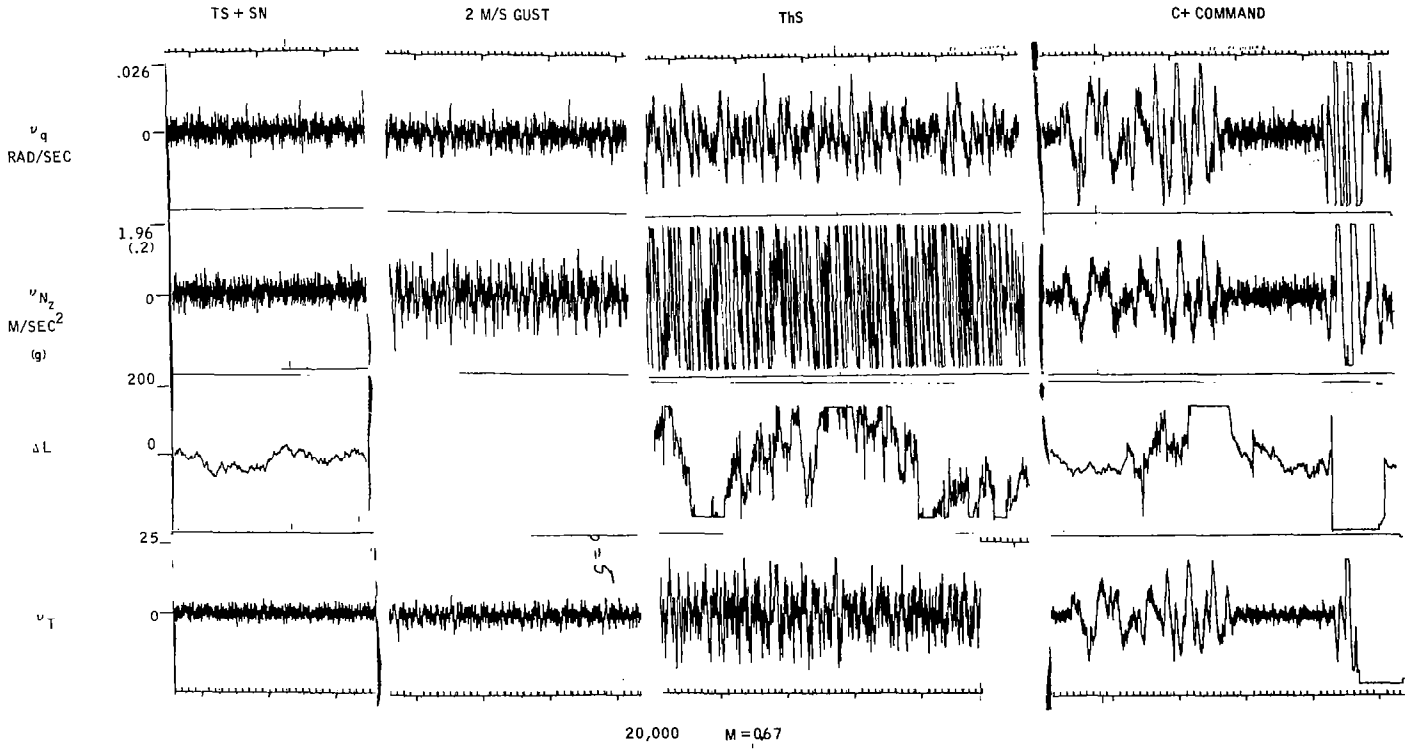
TS + SN
2 M/S GUST
ThS
C+ COMMAND
.026
0
v_q
RAD/SEC
1.96
(.2)
0
v_{N_z}
M/SEC^2
(g)
200
0
ΔL
25
0
v_T
20,000
M=0.67

Figure B1

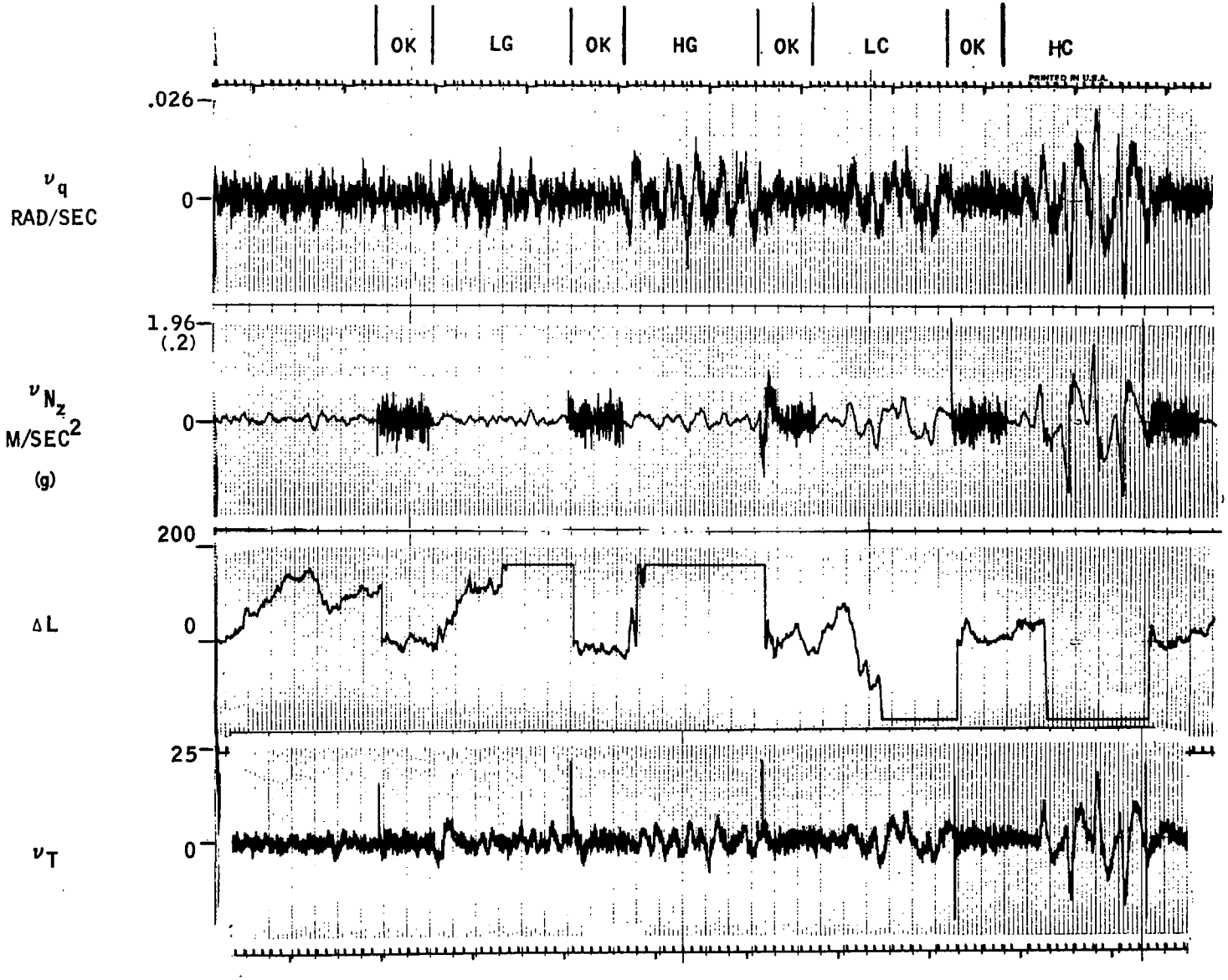
OK
LG
OK
HG
OK
LC
OK
HC
.026
0
ν_q
RAD/SEC
1.96
(.2)
0
ν_{N_z}
M/SEC^2
(g)
200
0
ΔL
25
0
ν_T

Figure B2

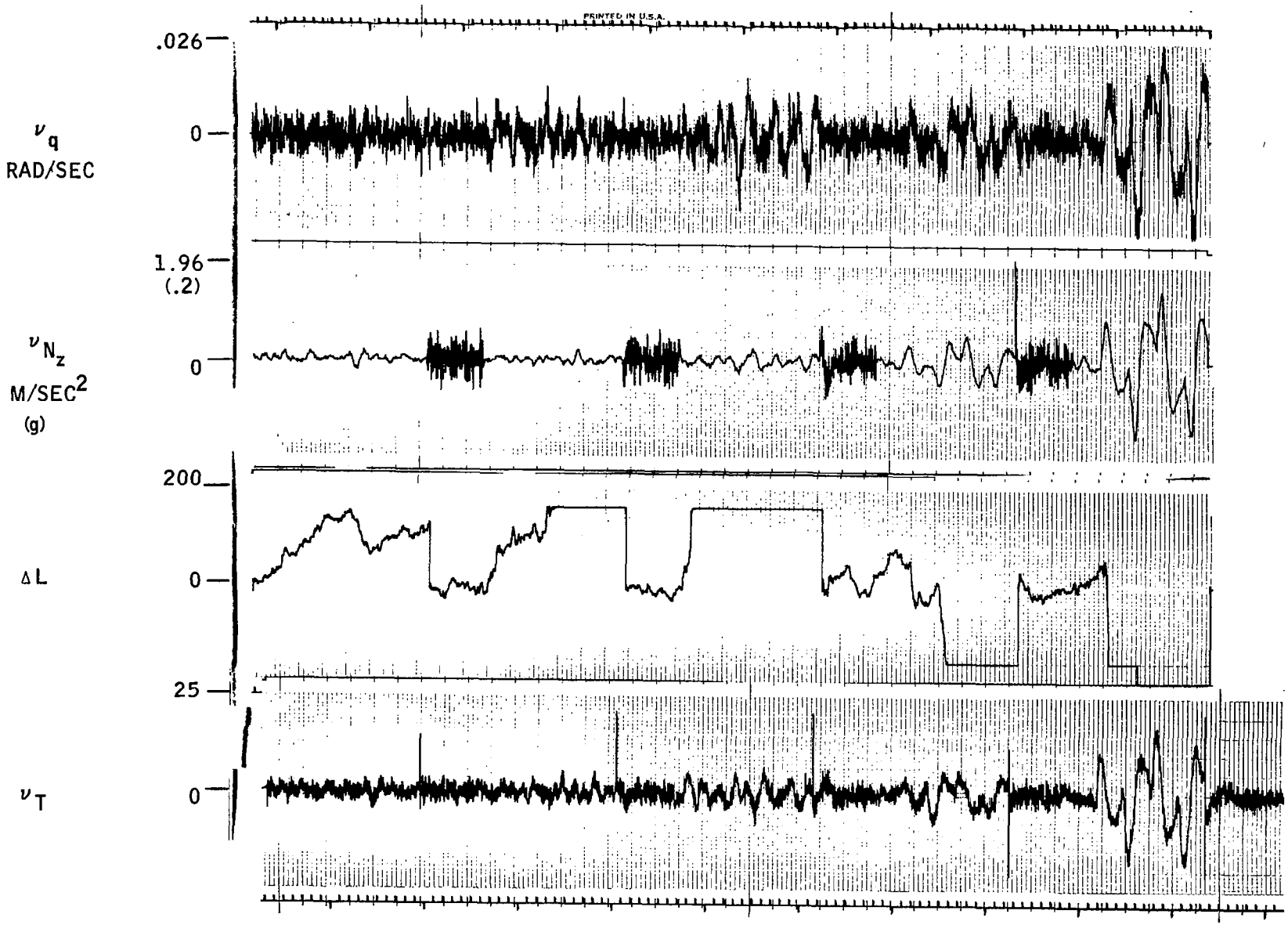
PRINTED IN U.S.A.
.026
0
ν_q
RAD/SEC
1.96
(.2)
0
ν_{N_z}
M/SEC^2
(g)
200
0
ΔL
25
0
ν_T

Figure B3

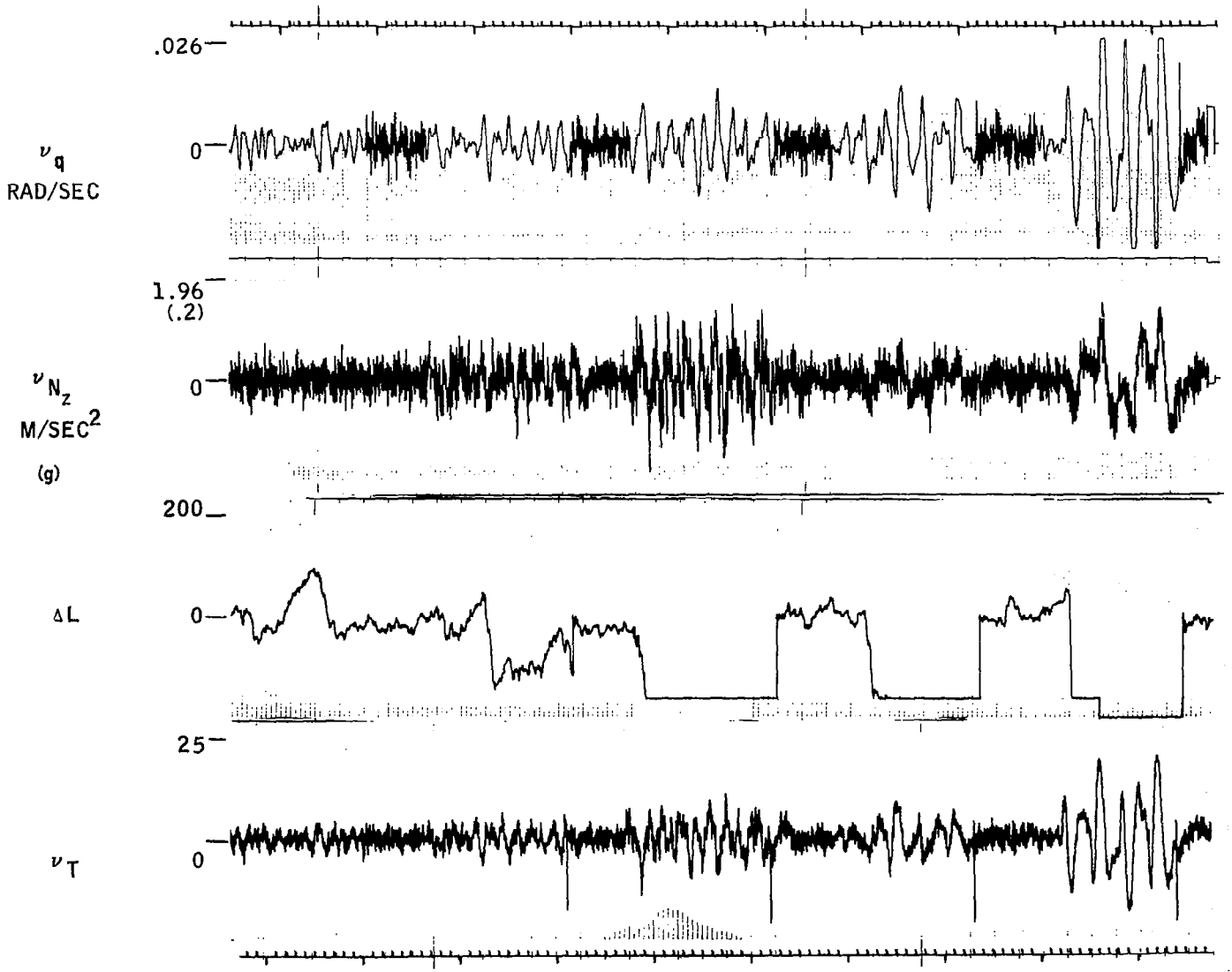

Figure B4

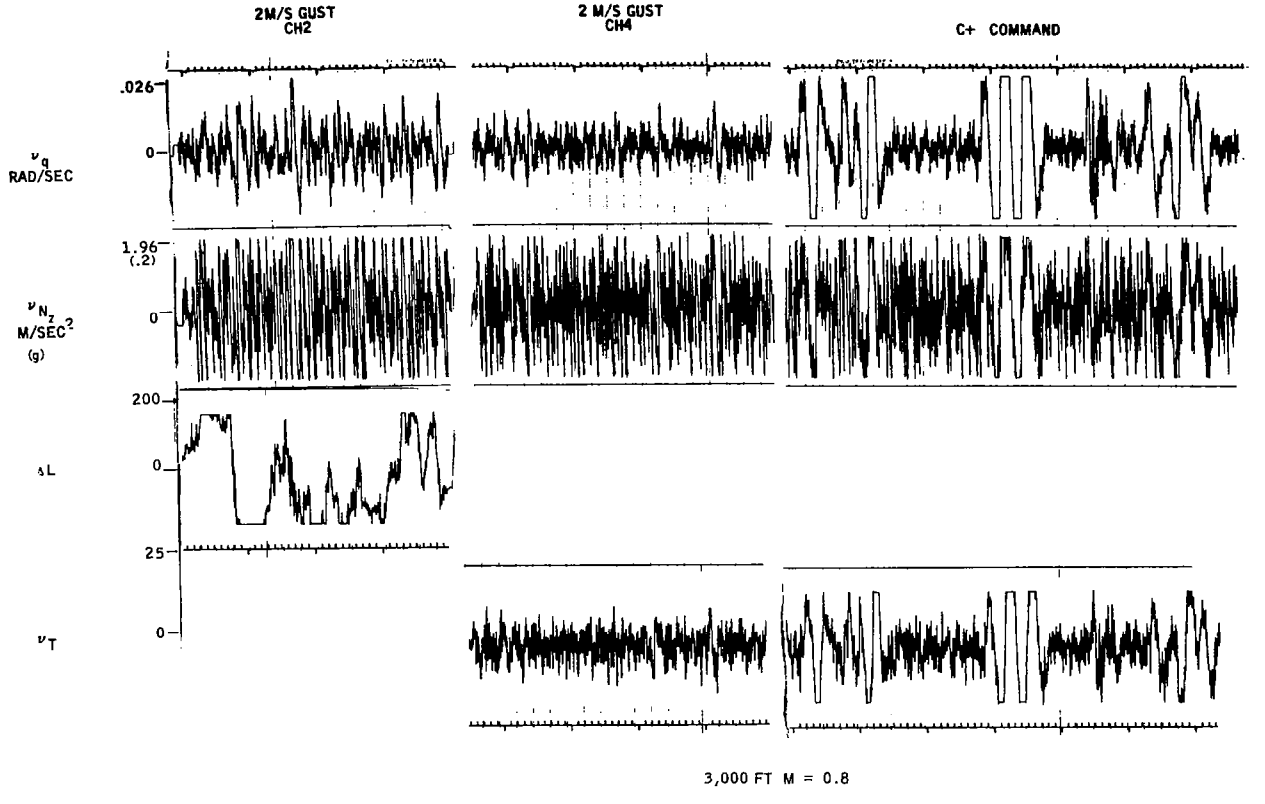
2M/S GUST
CH2
2 M/S GUST
CH4
C+ COMMAND
.026
0
ν_q
RAD/SEC
1.96
(.2)
0
ν_{N_z}
M/SEC^2
(g)
200
0
ΔL
25
0
ν_T
3,000 FT M = 0.8

Figure B7

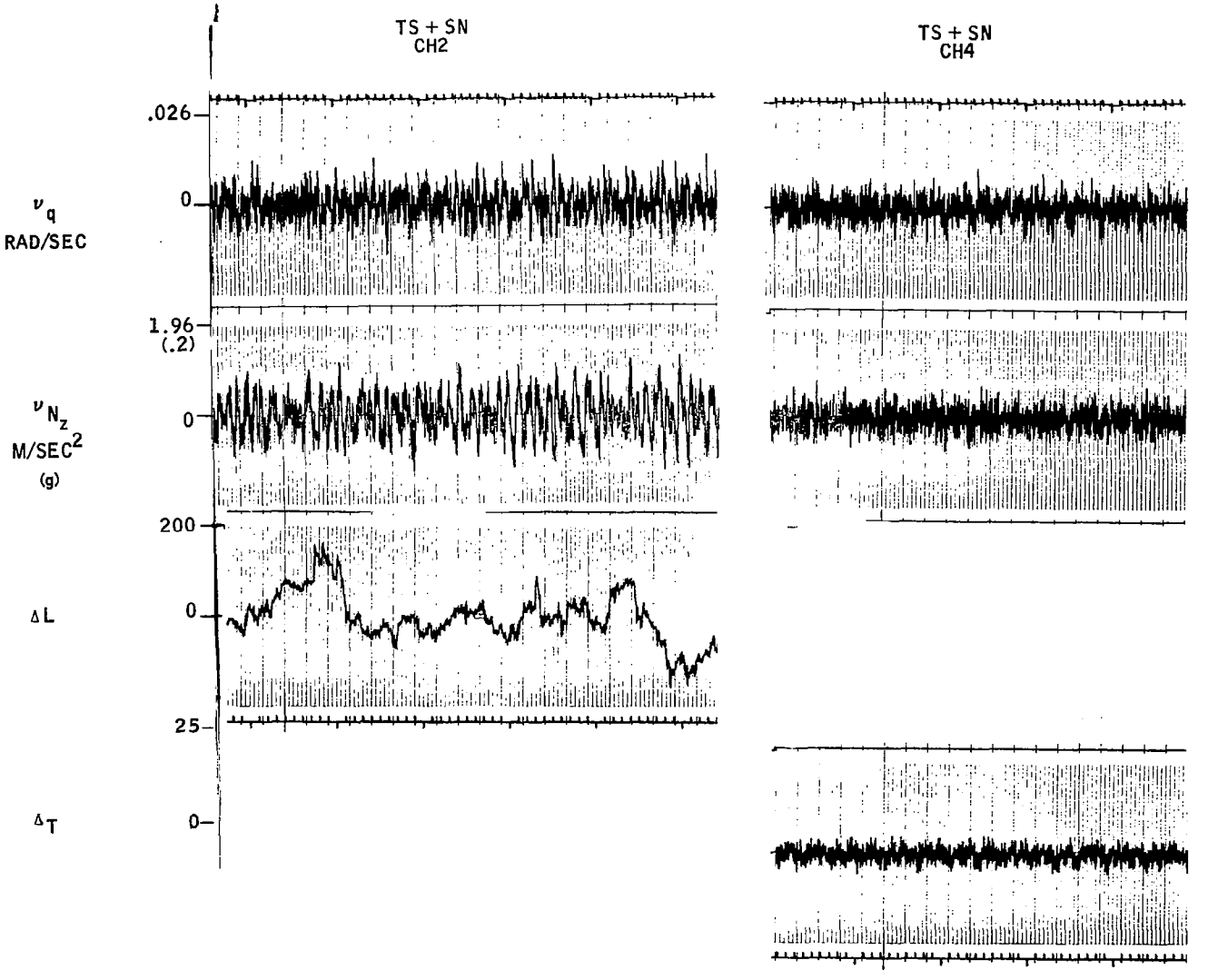

Figure B7 (Concluded)

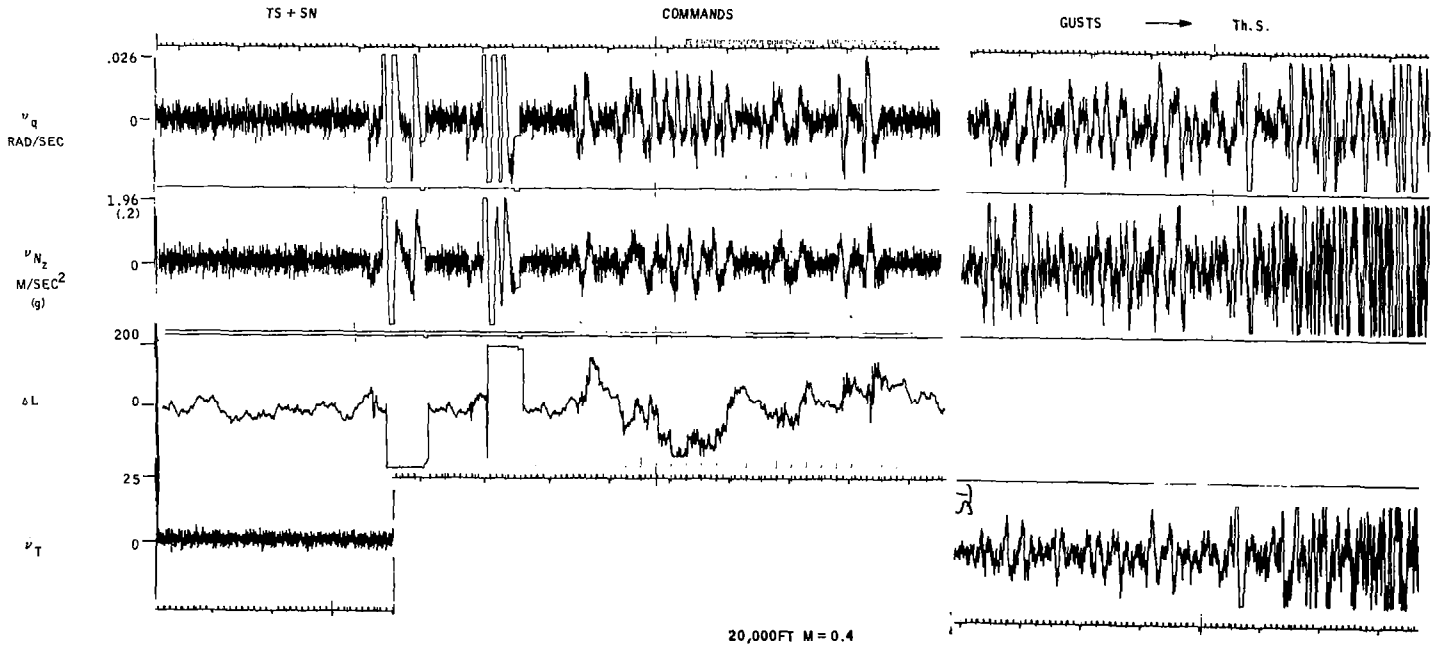
TS + SN
COMMANDS
GUSTS
Th.S.
.026
0
ν_q
RAD/SEC
1.96
(.2)
0
ν_{N_z}
M/SEC^2
(g)
200
0
δL
25
0
ν_T
20,000FT M = 0.4

Figure B8

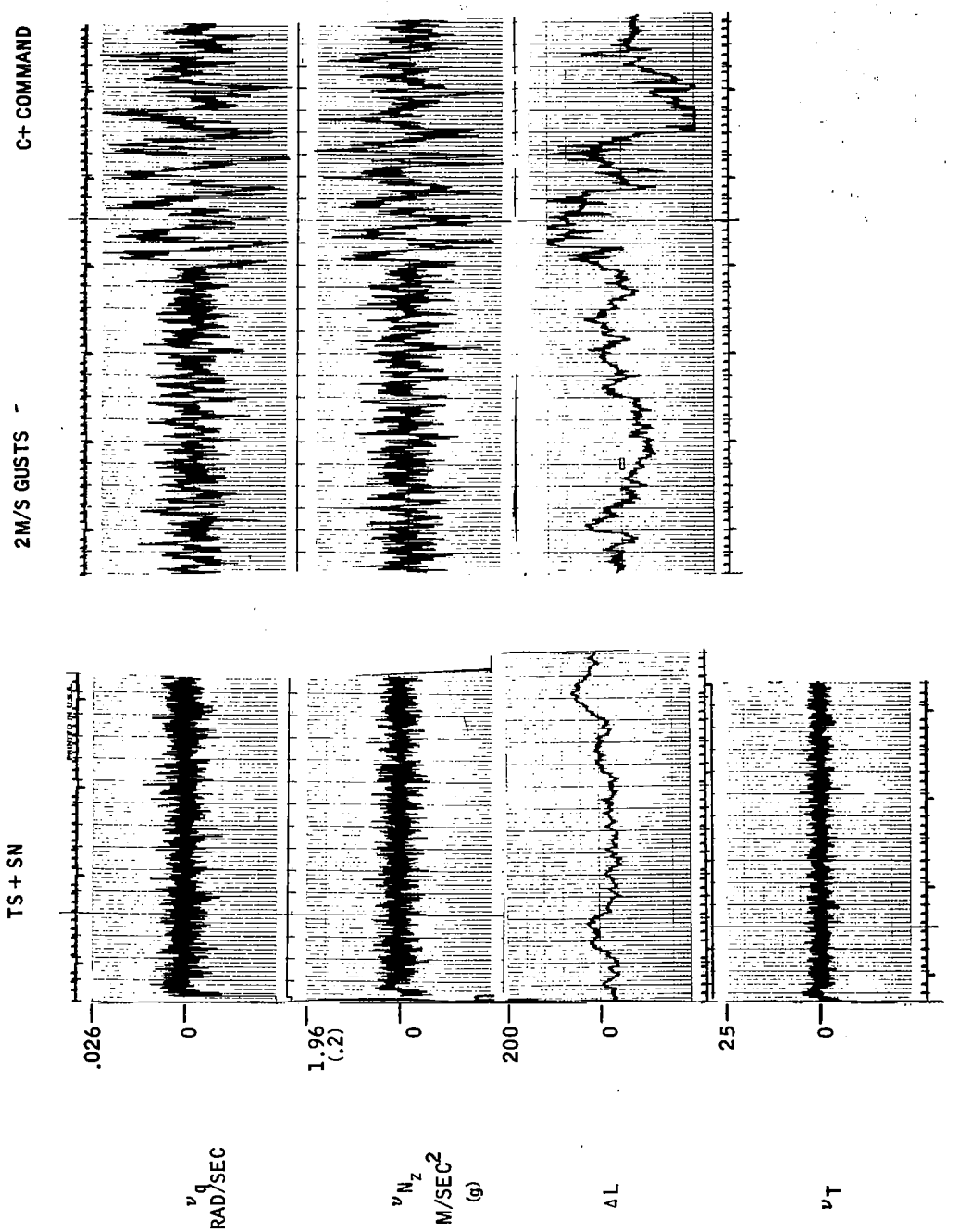

Figure B9

*U.S. GOVERNMENT PRINTING OFFICE: 1977 - 735-004/24